INTEGRATING OPTICAL EMITTERS INTO SILICON PHOTONIC WAVEGUIDES

INTEGRATING OPTICAL EMITTERS INTO SILICON PHOTONIC WAVEGUIDES

By

JOEL MILGRAM, B. ENG., M.A.SC.

A Thesis

Submitted to the School of Graduate Studies

in Partial Fulfilment of the Requirement

for the Degree

Doctor of Philosophy

McMaster University

© Copyright by Joel Milgram, April 2008

DOCTOR OF PHILOSOPHY (2008)	McMaster University Hamilton, Ontario
MASTER OF APPLIED SCIENCE (2002)	McMaster University Hamilton, Ontario
BATCHELOR OF ENGINEERING (2000)	McMaster University Hamilton, Ontario

TITLE: Integrating Optical Emitters into Silicon Photonic Waveguides

AUTHOR: Joel Milgram (McMaster University)

SUPERVISOR: Professor A. P. Knights

NUMBER OF PAGES: *x*, 196

Abstract

This thesis reports work targeting the integration of Si light emitters with optical waveguides. Such integrated devices would find utility in a number of applications including telecommunications, optical interconnects, and biological and chemical sensors. Much research has been directed by others on how to improve the emission efficiency and achieve lasing in VLSI (very large scale integration) compatible sources. Here, the focus is on how such devices can be integrated with planar waveguides. Two enhancement techniques were selected for potential integration; defect engineering (DE), and Si nanocrystals (Si-nc) embedded in SiO_2. Defect engineered light emitting diodes (LEDs) made on silicon-on-insulator (SOI) and emitting at 1.1 μm were successfully demonstrated. In addition, surface photoluminescence from SOI was analyzed to account for interference from the SOI cavity. However, it was determined that the emission efficiency of defect engineered LEDs studied during the course of this work is below that which was reported previously, and that the fabrication procedure thus suffers from irreproducibility. Barring an enormous advancement in the DE technique, it is concluded that the emission efficiency is too small to make use of its integration potential.

A more successful approach was obtained from the Si-nc system fabricated using electron-cyclotron resonance plasma enhanced chemical vapor deposition (ECR-PECVD). Optically pumped edge emitting devices were

designed, fabricated and characterized. The devices are comprised of Si-ncs emitting at 800 nm, integrated with slab silicon nitride waveguides. This work is the first report of edge emission from Si-ncs integrated with silicon nitride waveguides. Edge emission and waveguide properties were characterized in the ~850 nm emission band of the Si-ncs. The edge emission was well described as a propagating mode, attenuated primarily by the Si-nc film. Propagation losses of a typical air/Si-nc/SiN_x/SiO_2 waveguide were measured to be 11 ± 2 dB/cm and 20 ± 2 dB/cm at 850 nm in the TE and TM polarizations respectively. A wavelength dependent loss of -0.14 ± 0.03 dB/(cm*nm) was found to exist in the material loss of Si-nc films. In addition, the Si-nc films were found to undergo a partially recoverable photo-induced degradation of PL efficiency during exposure to pump light. Processing techniques compatible with both high efficiency Si-nc and low loss silicon nitride were developed and described. A two-sectioned photonic device was also designed, fabricated and characterized. The device contained an optically pumped Si-nc emitting waveguide section integrated with a low loss silicon nitride slab waveguide. The potential for optically pumped Si-nc emitters integrated with silicon nitride photonic circuits thus appears promising.

Acknowledgements

This thesis is based largely on experimental work, and therefore I have many people to thank. Firstly, Doris Stevanovic, Zhilin Peng, Jim Garrett and Graham Pearson for their help in the fabrication facilities. Also, Jacek Wojcik, Charlie Zhang and Tyler Roschuk for providing deposited films, Othman Zalloum for setting up a photoluminescence apparatus, and Doug Bruce for his insights in experimental optics. Without the skills and continuity these people bring to the lab, departmental research would grind to a halt. Aside from the obvious help just mentioned, I am also grateful to the above people for accommodating my frantic binges of experimenting, separated by long pauses of analyzing data and wondering what to do next. I would also like to thank Jon Lannan, Steve Gou, Phil Foster, and Jon Bradley, and Jonathan Doylen for making life in the sub-basement interesting. I thank the Ion Beam Centre at the University of Surrey for providing implanted samples, and to Peter Mascher and Paul Jessop for extensive use of their facilities. I thank my supervisor Andy Knights, and my committee members Peter Mascher again and Dan Cassidy, for their guidance. Lastly, I would like to thank my family for knowing not to ask how my research is going, and to Jen for reminding me not to work too hard (which I never do).

"Keep the company of those who seek the truth, and run from those who have found it."

V H

Table of Contents

Chapter 1. Introduction 1
1.1 Introduction and Objectives of Silicon Photonics 1
1.2 Overview on the Development of a VLSI Compatible Laser 3
1.3 Thesis Purpose and Approach 7
1.4 Summary of Contributions to the Field 9
1.4.1 Defect Engineered LEDs 9
1.4.2 Si-nanocrystals 10
1.5 Thesis Outline 10
Chapter 2. Background and Literature Review 12
2.1 Light Emission in Bulk Si 12
2.2 Common Efficiency Enhancement Techniques 16
2.2.1 Defect Engineering 19
2.2.2 Silicon nanocrystals 27
2.2.3 High purity Si 30
2.2.4 Porous Silicon 32
2.2.5 Erbium Doped Silicon 37
2.3 Emitters Integrated in Waveguides 38
2.3.1 Bulk silicon emitters integrated with waveguides 39
2.3.2 Silicon nanocrystal emitters integrated with waveguides 42
2.3.3 Integrated Porous Silicon Emitters 44
Chapter 3. Device Theory of Operation, Design and Fabrication 45
3.1 Theory of an Integrated Emitter 45
3.1.1 Planar Waveguide Modes 45
3.1.2 Pumping Methods 50
3.1.3 Coupling of Sources to Waveguides 51
3.2 Design and fabrication of Defect Engineered LEDs 57
3.2.1 Design of defect engineered LEDs 57
3.2.2 Fabrication specifics of defect engineered LEDs 62
3.3 Design and fabrication of integrated Si-ncs 67
3.3.1 Design of integrated Si-ncs 67
3.3.2 Fabrication specifics of integrated Si-nc waveguides 73
Chapter 4. Measurement Techniques 80
4.1 Surface emission from multi-layer film stacks 80
4.2 Emission efficiency 86
4.3 Waveguide properties 93
Chapter 5. Results and discussions on Si-nc devices 108
5.1 Surface Emission 108
5.2 Fatigue of PL 117
5.3 Emission Efficiency 126

5.4 Si-nc core slab waveguides 129
5.5 SiN_x core passive slab waveguides 141
5.6 Si-ncs integrated with SiN_x core slab waveguides 147
5.7 Summary on the integration of Si-ncs in waveguides 166
Chapter 6. Results and Discussions on Defect Engineered LEDs 170
6.1 Photoluminescence of Defect Engineered Si 170
6.2 Electroluminescence of Defect Engineered Si 178
6.3 Summary of Defect Engineered LEDs 184
Chapter 7. Conclusions and Future Work 186
Appendix I Gain Measurement 188

List of Figures

Figure 1: Schematic of phonon assisted ... 14
Figure 2: Schematic of the region of Si near a dislocation loop ... 22
Figure 3: Band-gap diagram of a DE *p-n* junction... 23
Figure 4: Schematic of an arbitrary slab waveguide ... 46
Figure 5: An example of the modal solutions of a slab waveguide ... 48
Figure 6: Schematic of a hypothetical unguided emitter integrated through "end-fire" coupling to a planar waveguide. ... 52
Figure 7: Simulation of the implant and diffusion profile of boron ... 60
Figure 8: Simulation of phosphorous implantation ... 60
Figure 9: Cross section of a lateral injection LED made on SOI... 62
Figure 10: (Top) Schematic of a two-sectioned waveguide with integrated Si-nc transmission section, coupled to a low-loss transmission section. (Bottom) Schematic of a conventional Si-nc core slab waveguide. ... 68
Figure 11: Simulated waveguide loss in an air/SiN_x/SiO_2 waveguide ... 72
Figure 12: Simulation of the coupling loss between the emission and transmission sections of a two-sectioned device with varying SiN_x core thicknesses. ... 72
Figure 13: Staircase pattern of a two sectioned device ... 75
Figure 14. Schematic showing the origin of interference of spontaneous emission generated within the Si overlayer... 81
Figure 15: Schematic of experimental setup for measuring surface PL spectra ... 86
Figure 16: Schematic of a point source within a material ... 88
Figure 17: Experimental setup diagram used for LED characterization. ... 92
Figure 18: Experimental setup used to measure PL efficiency of Si-nc films. ... 93
Figure 19: Prism coupling diagram showing the measurement of N_{eff} and α. ... 95
Figure 20: Photograph of the streak generated from prism coupled light. ... 98
Figure 21:Pump probe setup used to measure gain in Si-nc waveguides. ... 99
Figure 22: SES measurement technique ... 100
Figure 23: Top-view of the SES measurements showing the introduction of system loss ... 102
Figure 24: Schematic of the SES experimental setup. ... 107
Figure 25:Theoretical modification of surface emission of an emitting material 109
Figure 26: Surface emission spectra from a single layer Si-nc film ... 110
Figure 27: Surface PL of multi-layer Si-nc films under different annealing conditions. ... 111
Figure 28: Refractive index of a Si-nc and $aSiN_x$ film ... 114
Figure 29: Fitted surface PL from air/Si-nc/SiN_x/SiO_2/Si ... 115
Figure 30: Fatigue measurement of the surface PL from ... 119
Figure 31: Fatigue measurement of the surface PL from the implanted. ... 120
Figure 32: Fatigue measurements on three samples, with three different pump intensities ... 124

Figure 33: Fatigue measurements on sample 014, annealed for 2 hrs in Ar_2: 5%H_2 at three different temperatures........ 126
Figure 34: PL signal with different pump laser peak intensities........ 127
Figure 35: Example of streak and SES measurements........ 131
Figure 36: Waveguide loss measurements v.s. wavelength of the Si-nc core waveguide........ 131
Figure 37 Edge emission spectra of sample an air/Si-nc/SiO_2 waveguide. 135
Figure 38: Loss measurements of an air/SiN_x/SiO_2 passive waveguide, made using the streak method. 142
Figure 39: Streak measurements of three air/SiN_x/SiO_2 waveguides from the same deposition under different annealing conditions........ 144
Figure 40: Streak measurements of a air/SiN_x/SiO_2 after high temperature annealing showing H adsorption followed by H desorption........ 145
Figure 41: Loss measurements of an air/Si-nc/SiN_x/SiO_2 waveguide (035x1) at different wavelengths........ 149
Figure 42: SES measurement showing the un-normalized power carried by the TE and TM polarizations. 152
Figure 43: Edge emission spectra of an air/Si-nc/SiN_x/SiO_2 waveguide........ 154
Figure 44: Edge emission spectra of an air/Si-nc/SiN_x/SiO_2 waveguide with incrementing excitation positions........ 155
Figure 45: Edge emission spectra collected with the SES setup using 4 different knife positions........ 157
Figure 46: Streak measurement on the two sectioned device. 159
Figure 47: Streak measurement on the two sectioned device. 160
Figure 48: Streak measurement on the two sectioned device. 161
Figure 49: Edge emission spectra collected out the transmission facet of the two-sectioned device 164
Figure 50: Room temperature PL of virgin and DE bulk Si. 173
Figure 51: PL from unimplanted 5μm silicon overlayer on........ 175
Figure 52: PL from implanted 5μm silicon overlayer on........ 175
Figure 53: PL from implanted 1.5/1.0 μm SOI........ 176
Figure 54. EL spectra of a bulk Si LED with Er implantation........ 179
Figure 55: Example of and IV curve for a lateral injected LED........ 179
Figure 56: EL power of a laterally injected 1mm diameter bulk Si LED........ 181
Figure 57: EL power vs current for a laterally injected 1 mm diameter LED integrated on SOI. 183
Figure 58: Pump-probe measurement of surfaced pumped prism coupled light in an integrated Si-nc waveguide........ 188

List of Tables

Table 1: Starting substrates for DE LEDs. 63
Table 2: Preparation routes for the implantation and annealing of LED fabrication 64
Table 3: Sample List for Surrey I 64
Table 4: Sample List for Surrey II 65
Table 5: Waveguide mode properties of the conventional and two-sectioned 71
Table 6: A partial Si-nc sample list.. 78
Table 7: Fall times, in seconds, for the PL signal 125
Table 8: Fitting parameters for the PL signal from Figure 32. 125
Table 9: Internal quantum efficiencies of sample 031x1 measured at different pump intensities 128
Table 10: Waveguide loss measurements of a Si-nc core waveguide, 016x3, at different wavelengths using the streak method. 132
Table 11: Loss measurements of a SiNx core waveguide 142
Table 12: Loss measurements of an air/Si-nc/SiN_x/SiO_2 waveguide at different wavelengths using the streak method.. 149
Table 13: Ratio of the measured edge power of the TE and TM polarizations of SES measurements.. 153

Chapter 1. Introduction

1.1 Introduction and Objectives of Silicon Photonics

In traditional optoelectronics, the vast majority of components are fabricated using III-V semiconductor based materials, such as GaAs and InP. This includes well established components such as diode lasers, diode amplifiers, light emitting diodes, modulators, waveguides, and InfraRed (IR) detectors. The driving electronics are achieved with a separate off-chip Si circuit. Packaging the two chips into one unit is a non-trivial task that increases the overall cost and severely limits the complexity of the photonic circuit to a few discrete components.

Silicon photonics attempts to merge the photonic and electronic functions onto an all-Si platform [1- 4]. The main objectives are to produce cheap components in high volume, and allow monolithic integration with Si circuits. This would lower the cost of existing devices, and allow the complexity and functionality of the chips to be increased. Silicon photonics targets the telecommunication industry, optical interconnects in computers, and chemical and biological sensors.

The paramount design philosophy in this field is to make use of silicon material and processes that are compatible with the fabrication of silicon microelectronics. This design decision is based more on economic merits than on

technical or physical merits. The idea is to take advantage of the huge infrastructure available for integrated circuits on Si, often called VLSI (very large scale integration) or ULSI (ultra large scale integration). VLSI infrastructure includes foundries for high-purity silicon processing, decades of refinement of fabrication processes, suppliers of equipment and materials, physically based computer models, standards, roadmaps for future requirements, and a trained workforce [5]. Economically, VLSI owes its success to its ability to mass produce chips with high transistor densities in a single planar process flow. It is not only feasible to produce relatively simple chips with single functions, but also to fabricate intricate and complex chips with high-level multi-functionality.

In a photonic circuit, one wishes to generate, modulate, transport and detect light. Passive devices such as low-loss waveguides, splitters, gratings, arrayed waveguides, and ring resonators have been demonstrated in the literature and are fabricated in industry by companies such as Bookham, Kotura, Enablence Tech., and Luxtera. Ridge waveguides made from silicon-on-insulator (SOI) is the preferred platform for optical confinement [2]. Active, electrically driven low speed and high speed modulators have also been developed. Detectors operating in the telecommunications window of 1.5 μm have been developed [6], while efforts continue to improve the infra-red efficiency and rise time. However, an efficient, reliable, VLSI compatible Si based optical source is lacking. This is, without doubt, the missing link of silicon photonics.

1.2 Overview of the Development of a VLSI Compatible Laser

Research toward the development of a VLSI compatible laser has received steady attention for over 17 years, and continues on all imaginable fronts. There have been several highly publicized announcements [7-13, 31, 52], and an outsider to the field might falsely conclude a silicon laser is within reach.

The terms "silicon laser", "silicon emitter", "silicon compatible", "VLSI compatible", and "integration" deserve rigorous definitions. The concepts of "laser" and "emitter" are straightforward. Lasers are devices that have well defined optical cavities, feedback, and gain via stimulated emission. "Emitters" emit light through spontaneous emission, and are not necessarily arranged in any sort of intentional cavity. The terms "silicon emitter" and "VLSI compatible emitter" are used interchangeably in the literature regardless of the role of the silicon (be it the actual emitting material, involved in part of the excitation process, involved in guiding, in mechanical support, or any combination thereof). Unfortunately, the most important concept of all, VLSI compatibility, is used by many and defined by few. In the strictest sense, a claim of VLSI compatibility means that the emitter can be fabricated along side CMOS and/or BJT chips in a VLSI process flow permitting the design of fully integrated components. A less demanding definition might only require that the fabrication of the emitter make use of standard VLSI processes and materials. Lastly, "integration" refers to the process whereby discrete components are merged into a larger system. There are

different degrees of integration, and they are categorized according to the fabrication method. Here "integration" is defined as the fabrication of multiple and interconnected devices in a planar process. "Monolithic integration" makes a further requirement that the devices in question remain crystalline across their interfaces. In contrast, "hybrid integration" refers to discrete components that are fabricated on separate chips, and then connected in a non-planar process that is either automated, performed by hand, or a combination of the two.

Direct band-gap III-V, and II-VI semiconductors are the primary materials used to make diode lasers, light emitting diodes, and optical amplifiers. As will be discussed in chapter 2, silicon has an indirect band-gap and therefore does not efficiently emit light in standard *p-n* devices. It seems obvious, then, that a hybrid solution employing both III-V's and Si should be the best solution. Attempts have been made to monolithically grow epitaxial III-V films on Si, but thus far these attempts have been thwarted by the severe strain caused by the lattice mismatch and thermal expansion coefficient difference between Si and III-V layers [8]. Recently, III-V nano-wires grown on Si have shown photoluminescence, although the utility of freestanding nanostructures in a VLSI circuit is questionable. Wafer fusion bonding of III-V films on Si has been successfully demonstrated, and will be discussed shortly.

In hybrid-integration, a separate III-V laser diode chip is either mounted on the Si chip directly, or on its own platform and coupled to the photonic circuit via an optical fiber. In the case of fiber coupling, there is a considerable mode

mismatch between the ~10 μm wide fiber mode and the ~1μm wide waveguide. This can introduce a large coupling loss, which can be partially relieved through the use of tapered waveguides [9]. In either case, an optical facet on the Si chip is required to couple in the laser light. Optical facets in silicon are difficult to fabricate. Unlike most III-IV semiconductors, silicon facets formed through crystal cleaving are rough, introducing considerable scattering losses of ~10 dB/facet. Mechanically polished facets can have losses approaching the Fresnel limit; however, polishing processes are time consuming, and limit facet formation to the edges of the chip. Facets formed through dry-etching of Si within the area of the chip have been investigated [10]. An interesting solution to the problem of facet formation is through the use of surface gratings. As opposed to butt coupling, where the fiber or laser core must be aligned co-planar to the Si waveguide core, a surface grating allows waveguide coupling of non-coplanar light sources directed through the surface of the silicon chip [9]. Surface gratings then eliminate the necessity for facets.

Regardless of the coupling method used in hybrid integration, the positional tolerance required for alignment of the laser facets with waveguides is difficult to achieve in automation. Therefore, although hybrid integration is the only feasible option currently available, thus far it does not enjoy the same ease of fabrication, packaging costs and high throughput associated with Si microeletronics.

Alternatives to hybrid integration were not extensively studied until Canham's discovery of efficient photoluminescence from porous Si in 1990 [11]. That work inspired a huge effort to develop an efficient, reliable, electrically driven, VLSI compatible laser. Thus far, only two alternatives to hybrid integration stand out, both having made their initial announcements within the last four years. The first is Intel's laser based upon the Raman effect [12]. In this device an external pump laser is coupled to an SOI ridge waveguide resulting in stimulated Raman gain. The device contains a reverse-biased *p-i-n* junction to sweep out carriers and reduce the free carrier loss introduced by two-photon absorption of the high intensity pump light. Lasing has been demonstrated. While the work is unquestionably important, it is not clear how a Si-Raman laser has any advantage to an externally coupled laser. Not only is an external laser still required, but it has to be a high power laser, capable of an output power of hundreds of Watts. Admittedly, the lasing occurs within a Si gain medium, and therefore the laser intensity could be controlled on-chip; however, a Si Mach-Zehnder modulator could accomplish the same task.

The second major announcement, also from Intel, was the recent development of a hybrid, evanescent laser [13] in 2006. There, an InP wafer with AlGaInAs multiple quantum wells is bonded to a Si ridge waveguide. Electrically driven lasing has been demonstrated, and efforts continue at reducing the threshold current. The result is extremely encouraging. It remains to be proven that the process is compatible with a VLSI process flow, and that the performance

and cost are commercially viable. Both the Raman laser and the evanescent laser were initially developed in academia, and were subsequently adopted by Intel.

As well as the two technologies mentioned, there is a host of other techniques aimed at achieving luminescence in silicon directly, or in other VLSI compatible materials. These include, but are not limited to, porous Si [69], Si nanocrystals [50], ultra pure Si [7], defect engineered Si [31], impurities in Si such as Er [82], boron [14], strained SiGe, Si/SiGe superlattices, quantum wires [4], and ZnO [15]. Each technique has their advantages and disadvantages, but thus far there are no well-rounded solutions. A dominant technology has not emerged, and research continues at improving the emission efficiency, stability, thermal properties, and at achieving electrically driven stimulated emission. The two techniques relevant to this thesis, Si nanocrystals and defect engineering, are reviewed in detail in sections 2.2.2 and 2.2.1 respectively.

1.3 Thesis Purpose and Approach

A silicon laser would represent a revolutionary advance for several applications including telecommunications, optical interconnects in computers and chemical and biological sensors and the ultimate goal of this field remains an electrically driven laser source. However, a laser is not necessary for all applications. A VLSI compatible spontaneous emitter could find utility in niche applications that require cheap components without the need for high efficiency,

high power, or narrow spectral width. For example, cheap, disposable chemical and biological evanescent sensors are sought [16, 17].

As discussed in the previous section, there is an ever growing amount of literature concentrating on improving the emission characteristics of silicon. Most works concentrate on improving "stand alone" figures of merit such as quantum efficiency, gain, and operating lifetime. These works have a short checklist for feasibility such as room temperature operation, and the ability to be pumped electrically. These are tremendously important attributes, but do not fully reveal how the emitter might perform in the larger system of a photonic circuit. From a broader perspective, ease of fabrication, and the performance of the emitter within the system as a whole are equally important. However, relatively few works examine how silicon emitters might be integrated with electronics/waveguides, or what benefits might result from having an on-chip emitter.

The aim of this work is twofold. First, as mentioned, very little work has concentrated on integration thus far, and there is value in pushing these technologies forward even as others work to improve the emitters themselves. Since the goal of the field is an *integrated* emitter, it is important that one tackles emission *and* integration. Further, lessons learned in attempting integration of one technique may possibly be applied to other techniques. The work may be transferable then, even if the technique itself later becomes obsolete. The second aim of this work is to identify potential applications that benefit from integrated emitters in their present form.

In this thesis I have examined, through experimental demonstration, the integration of light emitters with waveguides. To accomplish this, two light emission techniques (defect engineering, and Si-nanocrystals) were selected and treated as "given" technologies. The fabrication, underlying physics, and performance were assumed to be well enough documented to permit their further development into larger systems. Using each technique, optical emitters integrated with waveguides were designed, fabricated, and characterized.

1.4 Summary of Contributions to the Field

1.4.1 Defect Engineered LEDs

Defect engineered LEDs, which have previously been demonstrated on bulk Si [31], were successfully integrated on SOI waveguides. This result has been published in [18], where the design, fabrication and characterization of LEDs on SOI are described. In addition, surface photoluminescence (PL) of SOI was analyzed. The surface PL was found to be strongly modified by cavity interference, requiring detailed modeling to properly predict the modified emission spectrum. Although my intent was to explore integration, in this thesis I also present measurements on the bulk Si that are quite revealing when compared to previous claims. The electroluminescence (EL) efficiency of defect engineered LEDs was found to be less than previously reported, defect engineering was found

to lower the PL efficiency in Si, and the process was found to suffer from irreproducibility.

1.4.2 Si-nanocrystals

Optically pumped Si-nanocrystals, embedded in SiO_2 films were integrated with low loss silicon nitride waveguides for the first time. A two-sectioned device, containing an optically pumped emitter integrated with a low-loss silicon nitride waveguide was designed, fabricated and characterized. The incorporation of hydrogen through high temperature annealing, while beneficial to emission from the Si-ncs films, was found to increase material absorption in silicon nitride. This was reconciled by annealing at low lower temperatures. This work has been published in [19]. Additionally, the efficiency, stability, and gain characteristics of Si-nc films were explored.

1.5 Thesis Outline

The following is an outline of the remainder of the thesis document. Chapter 2 contains a background and literature review on the physics of light emission in silicon and some of the common enhancement techniques, primarily emphasizing defect engineering and Si-nanocrystals. This is followed by a review of integrated silicon light emitters. Chapter 3 begins with a section devoted to the theory necessary to understand the operation of an integrated emitter. The

remaining sections describe the design considerations and fabrication specifics of the devices used in this thesis. Chapter 4 describes the measurement techniques used in this work. This includes interpreting photoluminescence from multi-layer films, measuring the emission efficiency, and characterizing waveguide parameters such as effective index and propagation loss. Chapters 5 and 6 contains results and discussions on the work performed with Si-nanocrystals and defect engineering respectively. Thesis conclusions are summarized in Chapter 7.

Chapter 2. Background and Literature Review

2.1 Light Emission in Bulk Si

In semiconductors, light emission can result from the band to band recombination of electrons and holes. Electrons near the bottom of the conduction band and holes near the top of the valence band recombine releasing energy as a photon. This radiative recombination is the essence of spontaneous light emission in semiconductors.

The emission process is bound by energy and momentum conservation laws. The total energy of the carriers, E, and wave-number, k, must be conserved in the recombination process. In direct-band-gap semiconductors (which include III-V materials such as InP, GaAs, GaN), the bottom of the conduction band and top of the valence band are aligned in k-space, at the zone center. The conservation equations are [20, 21]

$$k_c - k_v = k_p \quad \textbf{(1)}$$

$$E_c - E_v = E_p \quad \textbf{(2),}$$

where c and v designate the electron states in the conduction and valence bands respectively, and p designates the emitted photon. The momentum difference, $k_c - k_v$, is small since the states are both near the zone centre, and the photon's small k_p

(usually neglected) can easily satisfy equation (1). Equation (2) shows the emitted photon's energy is equal to the bandgap, E_c-E_v.

Silicon has an indirect bandgap of 1.125 eV at room temperature [22]. The bottom of the conduction band is shifted by 85% from the zone centre to the zone edge in the <001> direction. The difference, k_c-k_v, is large, and cannot be conserved by a photon. Radiative recombination of an electron and hole can occur in a 3-body process involving the emission or absorption of a phonon, shown in Figure 1. This is called phonon-assisted radiative recombination [20, 21], and can be described by the conservation equations,

$$k_c - k_v = \pm k_q \quad (3)$$

$$E_c - E_v = E_p \pm E_q \quad (4),$$

where q designates the phonon, $+k_q$ designates phonon emission, and $-k_q$ designates phonon absorption (k_p has been neglected). The phonon most likely to assist the recombination is from the transverse optical phonon branch, and has an energy of 58 meV [22]. Emission would then predominantly show signal at 1.125 ±0.058 eV. At lower temperatures, exciton, multi-phonon, defect, and impurity peaks will also be present, as is described thoroughly in references [22, 23].

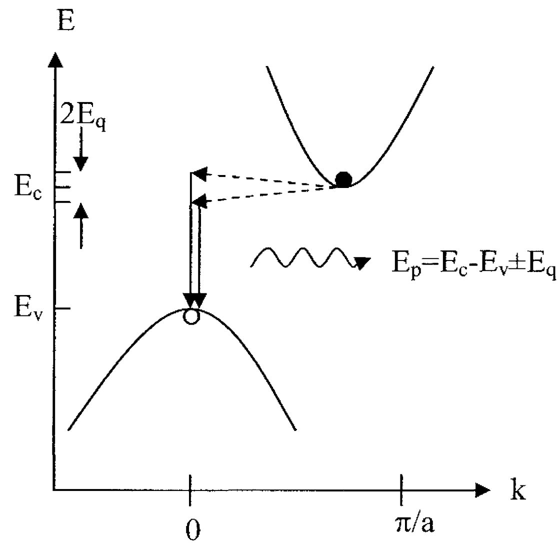

Figure 1: Schematic of phonon assisted radiative recombination of an electron and hole in the indirect band-gap of Si. Dashed lines show the contribution from phonon emission or absorption.

The rate of radiative recombination of minority carriers in semiconductors is generally described as having a characteristic lifetime, τ_r. Direct and indirect semiconductors differ drastically in τ_r. The phonon assisted process is much slower than direct transitions, and leads to larger radiative lifetimes in indirect semiconductors. For example, at room temperature and for low doped material, τ_r for GaAs is ~40 ns, whereas for Si τ_r is 250 ms [21].

Radiative recombination is not the only pathway by which carriers can recombine. There are non-radiative pathways that compete with radiative recombination. The dominant non-radiative recombination processes include Shockley-Read-Hall (SRH) recombination at defect and impurity sites, and Auger recombination [21, 24]. In these non-radiative recombination processes, energy is

released entirely as phonons with no light emission. In SRH recombination, impurities form localized states within the forbidden band-gap of the semiconductor. These states act as "stepping stones" for efficient non-radiative recombination. Carriers will tend to diffuse to the impurities and recombine non-radiatively before having the chance to recombine radiatively.

An internal quantum efficiency for photon emission, η_{int}, is then defined as the ratio of the radiative rate of recombination with the total recombination rate,

$$\eta_{\text{int}} = \frac{R_r}{R_{nr} + R_r} = \frac{\tau_{nr}}{\tau_r + \tau_{nr}} \quad (5),$$

where R_r and R_{nr} are the radiative and non-radiative recombination rates respectively [4]. This must be distinguished from the external quantum efficiency, η_{ext}, which takes into account the fact that only some of the light will escape the device and be available for detection. Additionally, power efficiency, η_{power}, is defined to be the ratio of emitted power to pump power.

With regard to equation (5), high purity, defect free semiconductors are essential for efficient emission. In III-V devices, carefully grown material can exhibit η_{int} as high as 0.99 [25]. In Czochralski grown Si, which is the VLSI

industry standard wafer grade [5], η_{int} is typically assumed to be 10^{-7}-10^{-6} at room temperature [4][1]. For this reason, III-V semiconductors have found tremendous success in high efficiency light emission devices, whereas silicon has not. Light emission in bulk Si is physically possible, although it accounts for a very small part of the total carrier recombination.

While emission from forward biased LEDs emits light at an energy corresponding to the band-gap, reverse biased LEDs operating in the breakdown avalanche regime have long been known to emit visible light. The visible emission, which also suffers from low efficiency, is likely due to transitions of hot carriers in interband and intraband processes, and the details are currently under investigation [26].

2.2 Common Efficiency Enhancement Techniques

As is listed in section 1.2, there are many techniques that have been developed to increase η_{int} of Si. Many authors describe structures that are "efficient", "very efficient", "highly efficient", or "extremely efficient.", yet do not even provide an efficiency measurement, and work exclusively in arbitrary units. It can be quite overwhelming to determine which techniques are actually

---

[1] This has become a benchmark for the field, and any η_{int} greater than 10^{-6} is usually said to be "efficient", or "highly efficient."

viable. A concerned reader must be armed with the following question list to critically evaluate a given technology.

1. Is output power or efficiency reported?
2. Is emission observed at room temperature, or only cryogenic temperatures?
3. How stable is the emission over time? What is the operating life?
4. Is the technique reproducible? How many groups get supporting results? How many groups get conflicting results?
5. What are the arguments for VLSI compatibility?
6. Is the device pumped optically or electrically?
7. Has stimulated emission been reported?
8. Is there discussion on how the results can be improved upon?

The list, presented above, is not intended to be exhaustive, but to highlight the main areas for concern which are typically hidden in the details, or not mentioned at all.

Most of the strategies for developing a VLSI compatible emitter rely on a combination of similar concepts. For emission generated within Si structures, the simple description leading to equation (5) is quite revealing, and suggests that efficiency can be improved by either increasing τ_{nr} (decreasing the probability of non-radiative recombination) or decreasing τ_r (increasing the probability of radiative recombination). This is indeed the case.

Non-radiative pathways can be blocked by removing non-radiative recombination centres, such as impurities and defects. This is done simply by using ultra-pure material. Similarly, confining the carriers to small volumes where the likelihood of there being a non-radiative recombination centre is small, accomplishes the same thing. The latter is employed by several technologies such as porous silicon, silicon nanocrystals, and defect engineering.

Further, the probability of radiative band-edge recombination in Si is thought to be improved through spatial confinement. In confined silicon structures, the band-gap, although still indirect, is shifted to higher energies. In addition, as the dimensions are reduced, the long range order of the atom arrangement in the crystal is also reduced. The bulk crystal electron states, formally associated with a very narrow k, become spread in k-space. The conservation of momentum, described in equation (3), is no longer as influential since electrons and holes now have some overlap in k-space. This is thought to increase the rate of radiative recombination, and allows the possibility of non-phonon assisted radiative recombination [27], although proving this effect experimentally is difficult.

Additionally, some methods circumvent emission in Si directly, and instead aim at introducing radiative centres in Si using extrinsic impurities, such as rare-earths [82], boron, or crystal defects [23].

However, the goal is a VLSI compatible laser, which does not necessarily need to involve silicon in the emission process except as a platform for

integration. For this reason, as already discussed in section 1.2, some researchers concentrate on other materials such as III-V [28, 29], and II-VI semiconductors [15], and their ability for integration with VLSI processing technology.

There are several thorough review articles that describe the multitude of enhancement techniques developed to date, such as [30], and it is beyond the scope of this thesis to describe them all. In the following sub sections, the general concepts regarding enhancement of emission in silicon devices are discussed further by way of examples. Particular attention is given to defect engineering (DE), and Si-nanocrystals (Si-ncs), since they are the methods employed in this thesis to fabricate devices.

2.2.1 Defect Engineering

Defect engineering (DE) as a route to high efficiency optical emission in silicon, first appeared in the literature in 2001 [31]. The model put forward by Homewood states that defects intentionally introduced between the surface and junction of a *p-n* Si LED enhance the room temperature EL η by blocking non-radiative recombination pathways.

The process for DE involves ion implanting a high dose of dopant atoms into a lightly doped wafer, followed by thermal annealing. The standard DE recipe uses ion implantation of boron at 30 keV, with a dose of 10^{15} cm^{-2} into low *n*-doped Czochralski grown (100) silicon. This is followed by an annealing step

at 950 °C for 20 minutes in N_2 atmosphere. These values are within typical ranges used in VLSI processing. However, this particular regime of process parameters is usually avoided in the fabrication of electronic devices since it is known to result in residual defects caused by implantation damage [5]. In the DE process, the boron implant forms the *p-n* junction, and concurrently introduces dislocation loops between the surface and the junction.

In [31] Homewood et al report room temperature EL and PL centred at 1.16 μm, and take this to be due to phonon assisted band-to-band recombination. They show that EL and PL is almost 3 times higher at 300 K compared to 70 K. The room temperature η_{ext} is reported to be $2.0*10^{-4}$.

The compatibility of DE with VLSI is unquestionable. DE makes use of standard equipment, in their standard operating ranges, and could be performed in the front end of a MOSFET process flow. However, the annealing temperature and time is quite critical, and would need to be accommodated. However, stimulated emission has not been demonstrated and the emission wavelength near 1.16 μm does not correspond to any current application in integrated optics, and would be reabsorbed in an SOI waveguide. To remedy this situation, Homewood has aimed at achieving IR emission through co-implantation of Er or S. References [32] and [33] show that emission at 1.55 μm and 1.3 μm from co-implanted Er and S respectively is enhanced by the presence of dislocation loops.

The emission efficiency in the 1.5 μm band is not reported, although it is reported to quench with temperature by a factor of 30 from 80 K to 300 K.

Homewood et al. have proposed a model to explain these results [31]. They show, by transmission electron microscopy, that dislocation loops are formed in the DE process. A dislocation loop is a defect whereby a single disk shaped plane of Si is inserted into the regular Si lattice. The edge of the disk forms a line defect that "loops" back onto itself. The loops are typically 80-100 nm in diameter, spaced 20 nm apart, oriented in the (111) direction, and positioned near the range of the implant between the surface and junction. The loops are formed from the collection of interstitial Si created through implant damage. While most of the implant damage heals upon annealing, there is an excess population of interstitial Si that has been displaced by the boron atoms that occupy substitutional positions.

Homewood's explanation for the enhanced luminescence is as follows. An elastic theory of dislocation defects predicts a considerable amount of stress at the edge of the dislocation loops. This stress causes a shift in the band-gap, estimated to be as high as 325-750 meV. Figure 2 illustrates this theory by showing a single dislocation loop, the estimated strain field, and the resulting shift in the band-gap. The net effect of the dislocation loops is considered to be the superposition of all the loops combined. Minority electrons injected across the forward biased junction would then experience a blocking potential and would be confined to a volume between the surface and junction, as illustrated in Figure 3.

Homewood argues that the predicted confinement discourages electron diffusion to non-radiative centres located in the bulk Si and at the surface.

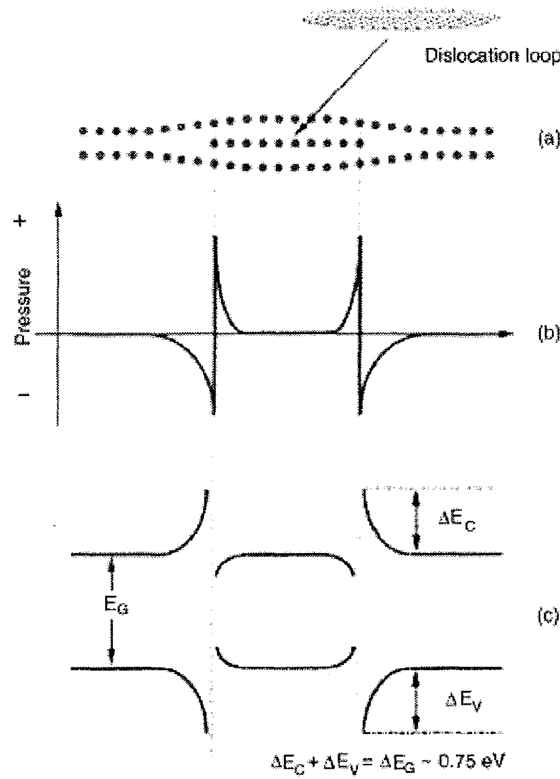

Figure 2: Schematic of the region of Si near a dislocation loop. a) shows a cross sectional diagram of the atom's positions in the vacinity of a dislocation loop. b) shows the stress introduced by the dislocation loop. c) shows the resulting band-gap deformation caused by the stress, after [34]

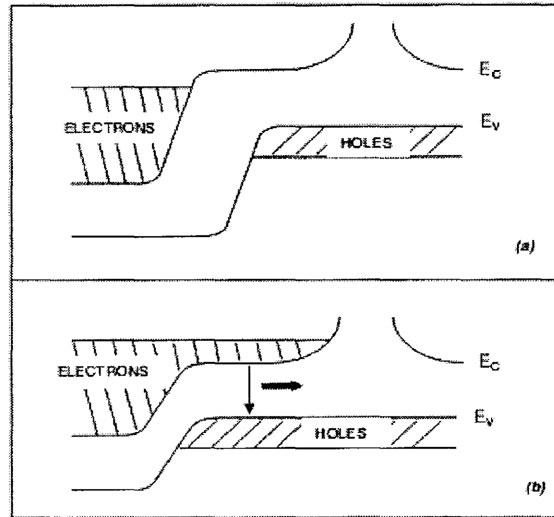

Figure 3: Band-gap diagram of a DE *p-n* junction. The surface is at the right of the diagram. a) shows the junction with no bias. b) shows the junction in forward bias. After [35].

The above few paragraphs describe the DE model published to date almost in its entirety. In subsequent publications, Homewood explores the parameter space of the DE process, and aims to defend the DE theory. In [32] the effect of annealing temperature and time on the EL η is measured. EL at 1.5 μm is explored through post-implantation of Er, followed by a 2nd rapid thermal anneal. Room temperature EL at 1.5 μm is reported. Comparing Er doped samples with and without dislocation loops, where the loops are found to enhance the 1.5 μm emission. Reported PL shows the 1.5 μm emission is below detectable levels when dislocation loops are not present. In [36] the dependence of PL of DE silicon is measured. In [37] the dislocation loop characteristics with varying implant energy is characterized using transmission-electron-microscopy.

In [38], LEDs are fabricated using the DE technique on virgin Si wafers, as well as with Si wafers that have been pre-amorphized through Si implantation. The pre-amorphization discourages dislocation loop formation, and permits the fabrication of near identical LEDs with and without dislocation loops. Homewood finds that the efficiency of the DE LED is 10 times greater than the pre-amorphized LED, and states that this "clearly shows" their model is correct. Curiously, the reported enhancement is *only* a factor of 10.

Homewood reports a correlation between the EL efficiency and the implant energy [39] and density of dislocation loops [40]. The primary conclusions of the two papers hinge on the authors' choice of fitting functions. However, the choice of the functions used to relate the EL efficiency to the DE parameters (Fig. 6 in ref [39] and fig. 6 in ref [40]) seems arbitrary and is not discussed.

DE has attracted controversy. Other groups that have fabricated heavily implanted Si LEDs have observed efficiencies close to that of Homewood's, with similar anomalous temperature properties. However, it is Homewood's explanation of the role of the dislocation loops that has aroused skepticism, and drawn criticism.

Sobolev et al. [41] describe EL from LEDs fabricated from boron and phosphorous implantation. The fabrication procedure is almost identical to [31], except for the implant energy which is 10 keV higher. EL has a dominant peak at

1.13 μm, indicating phonon assisted band to band recombination. The peak η_{int} of room temperature EL is measured to be 0.4 % . Defects, including dislocation loops, are observed for annealing temperatures between 700 and 1000 °C, but are not formed (or are repaired) for samples annealed at or above 1100 °C. After a 1000 °C anneal, dislocation loops are observed with a density of $4*10^8$ cm^{-2}. Sobolev reports a monotonic increase of the EL η with sample temperature similar to [31]. However, Sobolev does not observe a correlation between the η_{int} and the presence of defects. The η_{int} is greatest for the sample annealed at 1100 °C, which contained no defects. They suggest enhanced emission is due to gettering of non-radiative impurites[2], or the introduction of new radiative centres, however, these ideas are not elaborated or explored in detail. In a similar study, [42] reports EL from LEDs made using a procedure almost identical to [31], but with annealing performed for a 60 s duration using rapid thermal annealing. There, the presence of dislocation loops does not correlate with an improvement in emission efficiency.

In [43], Stowe et al. find that η is not influenced by the presence of a junction, an important component of Homewood's model. They form devices in a

---

[2] Gettering is a term that describes the behaviour of impurities during annealing. Many of the impurities of interest are larger than Si atoms, and preferentially sit in crystal defect sites. During annealing, these impurities diffuse to crystal defects where they become trapped. Gettering is used beneficially in VLSI processing by intentionally inserting crystal defects away from the device volume, drawing the impurities to a location where their presence has no consequence [5].

process identical to [31], except for the annealing which is done at 900 °C for 10-15 minutes. Boron is implanted into both p and n-type material, and a dislocation loop density of $5*10^{10}$ cm^{-2} is observed. Using cathode luminescence, they measure an η_{ext} of $5*10^{-6}$ for devices with and without a junction. They attribute enhanced emission due to recombination at the dislocations themselves, and propose a confinement model.

In [44], Kittler et al. fabricate LEDs in a similar process to [31]. They report room temperature η_{int} near 1%, as well as temperature properties quite similar to that of [31]. Remarkably, they develop a much simpler model to explain both their results and the results from [31]. Their model, which does not take into account dislocations, uses the simple description given by equation (5), and assumes τ_{nr} to be dominated by shallow Shockley-Read-Hall traps arising from the boron dopant atoms. Using calculated values for carrier concentration, they claim that the observed temperature behaviour and efficiency is expected.

Recently, Hoang et al. [45] fabricated LEDs in an almost identical process to [31], but with a 10 keV higher implant energy. Their LEDs yield an η_{ext} of 10^{-4}, a factor of 2 smaller than [31]. These LEDs were compared to LEDs made by boron gas diffusion, annealed to have the same sheet resistance as the implanted LEDs. The LEDs made through diffusion were 5 times more efficient than the LEDs formed through implantation. Hoang concludes that DE reduces the efficiency of band-edge emission in Si, instead of enhancing it. When the

diffused LEDs were further implanted with Si and annealed (to produce dislocation loops), the efficiency consistently drops. Homewood rebutted by explaining that the dislocation density obtained from the Si implant is 100 times larger that that of [31], and therefore is not optimized [46]

Other groups report luminescence associated with the defects themselves [47-49]. These are the so called D-lines (D1, D2, D3, D4), and show luminescence below the band gap at wavelengths between 1.25μm and 1.55 μm. Their origin is not well known, and is attributed to either the defects themselves, or to the segregation of impurities at the defects [23]. Although the intensity of these lines is quite small, the position of the D1 line near the telecommunication window of 1.5 μm has attracted some interest [47].

2.2.2 Silicon nanocrystals

Si nanocrystals (Si-ncs) are comprised of nano-sized crystallites of Si embedded in an SiO_2 matrix. The oxide provides chemical and mechanical protection, as well as ensuring the surface of the Si-nc is passivated and largely free from non-radiative defects, such as dangling Si bonds. Si-ncs are an improvement compared with porous-Si (P-Si), while utilizing similar physical processes to enhance optical emission. Unlike P-Si, the characteristics of Si-ncs are more reproducibly fabricated, and Si-ncs do not chemically react with the ambient environment, and therefore emit light more stably over time. The

disadvantage of using Si-ncs as the bais for silicon LEDs is the insulating nature of the films, and therefore the difficulty encountered in forming an electrical pumping mechanism.

Si-nc films are typically fabricated with the following process. First, a silicon-rich silicon oxide (SiO_x, x<2) layer is created with a thickness of a few hundred nm's. This can be accomplished through a variety of film deposition techniques such as chemical vapour deposition or sputtering, or it can be accomplished by ion implantation of Si into stoichiometric SiO_2. In each case, the as-deposited (or as-implanted) layer is predominately amorphous. During a high temperature anneal (900-1200 ^{o}C), the excess Si atoms separate from the homogeneous distribution and form nanocrystals within the oxide host [50]. Similar to P-Si, Si-nc films contain an ensemble of different nanocrystal sizes. The mean of the size distribution of the Si-ncs can be somewhat controlled through the excess Si concentration, annealing time, and annealing temperature, while narrow size distributions of Si-nc films have been fabricated through deposition of SiO_x/SiO_2 superlattices [58].

The VLSI compatibility of Si-ncs seems promising. Films can be fabricated with standard processes, although the high temperature anneal limits Si-nc formation to a front end process, prior or concurrent to electrical activation of implanted dopants. A further limitation is the Si-nc film's incompatibility with thermal oxidation steps, such as that used to isolate devices in the Local Oxidation of Silicon (LOCOS) process. Unless the Si-nc film is protected with an O_2

diffusion barrier, the nano-crystals will oxidize during such a thermal oxidation step, shrinking the Si-nc size until the Si-ncs eventually convert into SiO_2.

The wavelength of the PL from Si-nc films is typically in the 700-1000 nm range. A room temperature PL η_{int} as high as 59% has been reported for individual Si-ncs [51]. Electroluminescent devices have been demonstrated, but typically have a low power efficiency and operating life [4]. Optically pumped gain in Si-nc films has been reported [52, 53].

As is the case with P-Si, Si-nc layers have been comprehensively studied to determine the emission mechanisms. Much of the physics is considered to be similar between the two systems. However, even after a decade of work a great deal remains misunderstood and some basic questions are unanswered, as summarized in [54]. Many studies present data supporting the belief that emission is due to band-edge (or exciton [55]) recombination in a quantum confined structure, and correlate the Si-nc size with its emission properties [56,57, 58, 59]. Other studies find evidence that emission is due to recombination at surface states, possibly at double bonded Si=O, as shown in [54] and the references therein. There are even conflicting reports of the degree of electrical isolation between Si-ncs, and how carrier tunneling between nanocrystals impacts the emission properties [60].

There is wide support for the idea that the high emission efficiency of Si-nc films is, at least in part, due to a subset of nanocrystals that have an absence of

non-radiative recombination centres. Dangling Si bonds at the nanocrystal surface have been identified as a likely source for parasitic non-radiative recombination [61]. Further, many studies have observed that annealing Si-nc films in the presence of H_2 increases both the efficiency and PL decay lifetime. The effect is largely attributed to hydrogen termination of Si dangling bonds, which removes the non-radiative recombination pathway [62, 63]. The H_2 anneal can be concurrent to the high temperature nanocrystal growth anneal (900-1200 °C), or during a post anneal at lower temperatures, > 400 °C [61]. In Si-nc films grown at McMaster using ECR PECVD, it is observed that the PL efficiency of films annealed in Ar_2+H_2 is typically between 4-10 times higher than films annealed in Ar_2 or N_2 alone [64].

It is noteworthy that in addition to Si nanocrystals, recent work has aimed at the formation of amorphous Si nanoclusters [65]. These are thought to be more VLSI compatible than Si-ncs since the amorphous clusters can be fabricated with low temperature anneals (<900 °C), making their fabrication a more versatile process. Another recent development is the increasingly popular view that the SiO_2 matrix which surrounds the Si-ncs should be replaced by Si_3N_4. Such a system of Si-ncs embedded in Si_3N_4 has shown promising electrically pumped emitters [66].

2.2.3 High purity Si

High efficiency LEDs have been developed by Green at al using high purity silicon [7]. High purity silicon made from a float zone process is used as the starting wafer. The float zone crystal growth technique is known to produce wafers with much lower impurity levels than the Czochralski method, although it is currently limited to smaller wafer diameters [5], and therefore does not dominate the production of wafers for the electronics industry. The LED surfaces are carefully passivated with high quality, thermally grown SiO_2. LEDs with a room-temperature η_{int} as high as 0.01 have been reported, emitting near the Si band-edge at 1.1 μm [7]. Using photoluminescence, a similar design results in a very high room temperature η_{int} of 0.2 [67], with a correspondingly long carrier life time of ~10 ms. The reason for the success of these LEDs is straightforward - an absence of non-radiative recombination centers results in a long carrier lifetime and a large η_{int}.

For integration, the value of high purity LEDs is questionable. The starting float zone substrate is not VLSI compatible, since, compared to CZ grown Si, it is only available in lower wafer diameters. The long carrier lifetimes result in slow modulation speeds, and would require an optical modulator external to the emitter. Of greater limitation is that stimulated emission has not been demonstrated, and the emission wavelength does not correspond to any existing application in integrated optics. Integration with passive Si core waveguides is

possible, but somewhat limited. Although the emission wavelength necessarily[3] overlaps the phonon-assisted band-to-band absorption spectrum, the extinction coefficient of Si near the band edge is ~1.3 cm^{-1}, hence the losses incurred from propagation over short distances might be acceptable.

2.2.4 Porous Silicon

Porous silicon (P-Si), is by far the most heavily studied structure for light emission in Si. Its popularity is due to its ease and low cost of manufacture, and to an impressively high emission efficiency. These are the only appealing properties of P-Si, and from an integration perspective it is a very difficult structure to combine with VLSI technology.

P-Si is usually fabricated through a partial etch of crystalline Si in an electrochemical reaction with a HF:H_2O solution. This leaves behind a complex structure of crystalline Si features separated by interconnected volumes of pores, or voids. The amount of Si removed during etching and the feature size of the remaining Si skeleton can be somewhat controlled by selection of voltage, electrode geometry, etch duration, and solution concentration. An onset of increased efficiency occurs when the Si skeleton features are a few nm in dimension [11]. Two dominant components of PL emission are typically

[3] Light emission and absorption are reverse process of one another, that is, if there is a route for emission, there is also a route for absorption at the same wavelength.

observed, one centred in the red (~700-1000 nm) and another in the blue (~440-500 nn). Reference [68] reviews the capabilities of P-Si. The η_{ext} of photoluminescence (PL) at room temperature is typically >5% in the red band, and 0.1% in the blue band. Electrically pumped devices, of which there are numerous designs, have been fabricated with η_{ext} typically ~ 0.1%. [68]

Most work on P-Si concentrates on relating the physical properties (mainly size) to the emission properties. There are several comprehensive reviews on the subject [68,69, 70]. However, the structure of P-Si is very complex, and challenges even the resolution capabilities of electron-microscopy. Further, any given sample contains an ensemble of crystalline feature sizes, complicating the analysis. The etching of P-Si is difficult to control, making it hard to fabricate reproducibility. P-Si also has an enormous surface area to volume ratio, hence surface effects can play a dominant role over bulk properties.

The emission mechanisms are still under debate (almost 20 years after the discovery of the luminescent properties of P-Si), with conflicting experimental results reported [68]. Many favour a quantum mechanical confinement description, where the reduced dimensions of the structure increase the band-gap, blue shifting the emission wavelength, and allowing quasi-direct transitions. Others believe that emission is due to surface states, such as double bonded Si=O. The correct description may be a combination of the two, where confinement and surface states both play a role [71].

The PL efficiency from P-Si films is observed by some to decrease in time with increasing duration of photo excitation. This phenomenon, called "fatigue" (or photodegredation, or bleaching), has not been reported in the literature to occur in Si-nc films. That is, PL stability is not normally mentioned at all. However, fatigue in Si-nc films may be an unreported characteristic[4]. As is shown in section 5.2, partially recoverable fatigue is observed in Si-nc films fabricated at McMaster through ECR-PECVD, as well as through ion implantation performed at University of Western Ontario. In [72] PL degradation is reported in amorphous Si-nanoclusters (as opposed to nanocrystals) embedded in SiO_2. The PL power decreases by 20-30% over a 120 minute exposure. It is shown through FTIR that exposure to 325 nm pump light reduces the number of Si-H bonds, increases the number of dangling Si bonds, and it is concluded that this results in an increase in the number of non-radiative recombination centres. The pump laser intensity is not reported, and it is not suggested through what process the bond breaking actually occurs. In porous Si samples, fatigue has been more heavily reported. In [73, 74] photodegradation of PL is reported in P-Si samples. In [73], exposure to 266 nm light at 3000 $\mu J/cm^2$ reduces the efficiency (with a pump dose of $1 \mu J/cm^2$) by a factor of 13. There, it is suggested that the irreversible

---

[4] Personal communication with Dr. Al Meldrum, of the Dept. of Physics, University, of Alberta, during his visit to McMaster University in May, 2007. Dr. Meldrum confirmed his group observes degradation of PL in Si-nc samples. The behaviour in samples from his lab is, qualitatively, similar to that described in section 5.2.

component of the degradation is caused by the introduction of non-radiative centres created by high energy carriers.

During long breaks (minutes) in exposure to pump light, some report a partial recovery in the PL efficiency in P-Si [74, 75]. Interestingly, this is attributed in [75] to "blinking" (or intermittency) of the Si-ncs. Blinking of PL from indivudual nanocrystals has been observed in many materials, such as CSe, CTe, InP [76, 77], and has also been observed by two groups in individual Si nanostructures made from P-Si [75] and from oxidized e-beam of Si [78]. In the blinking phenomenon, it is observed that an individual nanocrystal will intermittently toggle from an emitting "on" state to a dark "off" state while under exposure to continuous pump light. It has been suggested, although not confirmed [77], that a nanocrystal is put into an "off" state when it is ionized in a photo-induced process. Ionization of a nanocrystal occurs when a photo-excited carrier tunnels through the nanocrystal:matrix barrier, and is temporarily trapped in the matrix, leaving behind a charged nanocrystal. It is argued that non-radiative Auger recombination is significantly enhanced in a charged nanocrystal since there is an extra free carrier (the carrier left behind during ionization) to encourage the process. Further photo-excited carriers will therefore more likely recombine non-radiatively, than radiatively. The nanocrystal remains in the "off" state until a carrier is returned to neutralize the nanocrystal. When individual nanocrystals are observed, the emission resembles a random pulse train. When an ensemble of nanocrystals are observed under continuous pump illumination, the

total emission is observed (by some groups) to decay with time, and will slowly recover during a waiting period when the pump light is blocked. In [75], it is empirically observed that the ensemble fatigue decays not exponentially, but as the power law, $(t+\tau)^{-B}$, where t is the duration of pump exposure, τ is a fitting parameter, and B is ~0.3. The blinking statistics from individual nanocrystals matches well with the observed fatigue and recovery of the ensemble of Si-ncs. (This power law behaviour is common to nanocrystals in other materials as well, and its empirical observation has prompted several models to explain its origin [77]).

From an integration perspective, P-Si has many undesirable properties. Because of the large surface area to volume ratio, the material is incredibly chemically and mechanically unstable. It is also difficult to imagine P-Si being used in a VLSI compatible process flow. The electrochemical etching of P-Si is difficult to mask, and perform selectively (a requirement for wafer level processing), and attacks photoresist, SiO_2, Si_3N_4 and most metals. Therefore P-Si formation does not belong at the end of a process flow since it would be difficult to protect other devices. P-Si formation does not find a good home at the beginning of a process flow either. The P-Si itself is chemically and mechanically unstable, and would require protection from subsequent processing steps.

Research on P-Si continues in the hopes of solving these problems, as shown by [79]. Further, some groups have exploited the chemical instability of P-

Si by using substrates as bio-sensors [80]. This may well be an application in which P-Si is feasible.

2.2.5 Erbium Doped Silicon

The rare earth, Er, has long found application in photonics. The intra-shell transition from the $^4I_{13/2}$ excited state to the $^4I_{15/2}$ ground state corresponds to a wavelength of 1.53 μm. Erbium doped fiber amplifiers have found tremendous success in long haul optical fiber communication systems. In fact, the invention of Er doped fiber amplifiers was the primary motive for the telecommunication industry to adopt the grid of wavelengths near 1.55 μm as the "conventional" band[5].

Erbium doped Si has been thoroughly studied, and there are many good review articles such as [81, 82]. Si can be doped with Er using a variety of techniques, including ion implantation. Usually Er incorporates into the silicon lattice interstitally as Er^{+3}. Due to a low solid solubility, Er tends to form optically inactive (non emitting) clusters when doped at concentrations beyond $3*10^{17}$ cm^{-3}. This and severe temperature quenching of the emission efficiency at

[5] During the development of long haul fiber networks, systems were designed for either1.3 μm or 1.5 μm. Laser sources were available for both wavelengths, and the two bands each correspond to local minima of material loss in silica fibers. The development of fiber amplifiers gave a clear advantage for working at 1.5 μm.

room temperature are the main problems associated with the fabrication of Er doped silicon emitters [81].

In Si, Er is excited through a rather complex multi-step process, each step having competing non-radiative processes [81]. First, electron hole pairs, generated optically or injected electrically, form free excitons. An exciton can then be captured at an Er trap, and may transfer its energy to the Er ion. The excited Er ion can then emit a 1.53 μm photon. A back-transfer of energy from the ion to the lattice, or a de-excitation of the exciton back into the bands are thought to be the primary causes of temperature quenching.

Erbium has been incorporated into bulk Si, amorphous Si, P-Si films, and Si-ncs films [81]. In the latter technology, many groups report that Si-ncs act as sensitizers for Er, increasing the excitation cross-section compared to an all SiO_2 host, although the exact explanation is still debated [83].

2.3 Emitters Integrated in Waveguides

Reports of silicon emitters integrated with optical elements have been published, and in some cases even patented. These works demonstrate an emitter integrated with one or two other optical components such as slab and ridge waveguides, and even detectors. The designs described to date are still in an early

stage of development, and the published articles focus mainly on the principle of integration as opposed to optimizing device performance.[6]

2.3.1 Bulk silicon emitters integrated with waveguides

Silicon-On-Insulator (SOI) is a natural choice of waveguide platform for bulk Si emitters[7]. Indeed, this is the direction taken by most of the (admittedly few) researchers in this field. EL and PL of surface emission from band-edge recombination of emitters integrated on an SOI platform has been demonstrated. In [84], bulk Si *p-i-n* LEDs on 50 nm thick SOI are reported to achieve room temperature surface EL with an η_{ext} of $2*10^{-6}$. In [85], EL from MOS transistors made on SOI are demonstrated, although the efficiency and origin of the emission is not reported. Reference [86] shows EL from *pn* LEDs made on SOI. A Bragg reflector on the top and bottom of the device is shown to improve the extraction efficiency of the surface emission. Recently, [87] demonstrate p-i-n LEDs with an η_{ext} of $1.4*10^{-4}$. The LEDs are formed on 200 nm thick SOI, and the low doped emission region is separated from the p/n contact regions by a thinned region, where the Si overlayer is reduced from 200 nm to 5-25 nm. The authors

[6] There are many works that demonstrate surface emitters integrated with thin film multi-layer reflectors (Bragg reflectors) that form a "micro-cavity". The micro-cavity modifies and emission spectrum and in some cases improves extraction efficiency. These works are not included in this review when there is no intent by the authors to achieve edge emission in a planar waveguide.

[7] Parts of this section have been published previously [18].

claim that the thinned regions act as a physical barrier for diffusion, and confine carriers to the island where the surface is well passivated, and where the Si has a low defect concentration. To decrease the resistance of the thinned regions, the carrier concentration is increased using gate electrodes.

Quantum well devices made from very thin SOI, with silicon overlayers a few nm thick have also been explored. There, PL originating from within the quantum confined Si layer, as well as from Si/SiO_2 interface states has been observed [88, 89].

While surface emission from Si emitters integrated into SOI has been reported on a number of occasions, edge emission has only been reported by one group. In [90], edge emission (and even stimulated emission) from SOI is described. The surface of the SOI is textured in a nano-pattern, and shows sub-bandgap 1.278 nm PL emission from defect states. While the result is encouraging, no other group has made a supporting measurement. Further, an efficiency is not reported, EL has not been demonstrated, and the sub-bandgap emission is only present at temperatures below 80 K.

In [91], SOI was used as an electrical platform for LEDs fabricated through focused ion implantation. White light was emitted when the junctions were biased in a reverse breakdown mode, with a power efficiency near 10^{-6}. As the emission is above band-gap, there is no hope of using the SOI as an optical waveguide, and the authors describe their future work as achieving emission at 1.5 μm.

In a recent study [92], Si micro-disks are formed by etching the Si overlayer in SOI. PL reveals the presence of whispering gallery modes.

Reference [93] demonstrates an evanescent protein sensor fabricated from an integrated transceiver. A *p-n* LED operated in the reverse bias avalanche regime is integrated with a Si_3N_4 waveguide. A second LED detector at the other end of the waveguide completes the transducer. As the emission is in the visible, a 150 nm thick, 25 μm wide, 900 μm long Si_3N_4 core with a 2.5 μm thick SiO_2 cladding is used for the guiding material since it is transparent to visible wavelengths. To optically couple the emitter (located at the surface of the Si substrate) with the waveguide (located on top of an SiO_2 cladding), the core extends down the non-vertical sidewall of the SiO_2 cladding to the junction. Details of the bending loss are not provided. The transceiver pair has a detector/emitter current ratio of $\sim 8*10^{-8}$. The integrated device includes an integrated microfluidic channel, supplying reagent flow into the evanescent field of the Si_3N_4 waveguide. A similar transceiver design is demonstrated in [94]. The design uses an SOI platform instead of bulk Si to limit material absorption from Si. A 200 nm thick, 3 μm wide, 240 μm long Si_3N_4 strip is claimed to act as a waveguide for the emitted light (which is at an unreported wavelength). Based on the plots supplied in the reference, the transceiver pair has a detector/emitter current ratio of $\sim 3*10^{-10}$.

2.3.2 Silicon nanocrystal emitters integrated with waveguides

Si-nanocrystals have been integrated into slab and ridge waveguides[8]. As EL devices are still an unreliable technology, the devices are always optically pumped. Previous studies that integrate Si-ncs in waveguides almost exclusively use Si-ncs embedded in a SiO_2 matrix as a waveguide core, while SiO_2 forms the bottom cladding, and SiO_2 or air is used as the top cladding. The material is often co-doped with erbium to achieve emission at 1.5 μm, the Si-ncs themselves emitting with a broad spectrum centred at 800-850 nm. This waveguide design is ideal both for its ease of fabrication and for the long interaction length which aids the search for stimulated emission, as is exampled by [95, 96, 97]. To date, optically pumped slab guides have shown edge emission from integrated Si-ncs [96, 97, 98, 99, 100] and from Er doped Si-ncs [101]. Ridge waveguides operating at ~850 nm have been demonstrated only as passive devices [102] – referring to the fact that the Si-ncs are not pumped, and waveguide operation is demonstrated with externally coupled lasers. Edge emission at ~850 nm arising from the Si-ncs has not been reported. However, ridge waveguides operating at 1.5 μm have shown Si-nc related edge emission [103, 104], presumably because of the lower propagation loss in the 1.5 μm band compared to ~850 nm.

---

[8] Parts of this section have been published previously [19].

In [105], a ring resonator employing a silicon nitride core waveguide with a Si-nc film cladding is demonstrated at 1.5 μm. An external light source is used to characterize the passive device. Si-nc related edge emission is not reported. Gardner and Brongersma's work in [105] is of particular relevance to this thesis study because it does not use the standard Si-nc core design while attempting to integrate Si-ncs. In this thesis, I show Si-nc emission at ~850 nm in slab structures using a Si-nc/silicon nitride /SiO_2 stack similar to [105], as well as a two-sectioned design.

Due to the industrial interest in the development of a silicon laser, it is plausible that researchers may choose to patent important work instead of publishing it. Several United States and European patents claim ownership of Si-nc waveguide device designs. None include any evidence of working devices, or give insights into the field not already covered by peer reviewed journal publications. However, to ensure complete coverage of publicly available information, patents are included in this review. In [106] an optical amplifier comprising of an Er doped SiO_2 core containing Si-nc with LED excitation is patented. A similar design is claimed under US Patent [107]. Patent [108] describes the concept of using Si-ncs as a laser medium within a planar waveguide with any of several feedback methods. The materials comprising the waveguide may include SiO_2 and Si_xN_y. The placement of the Si-nc within the waveguide is not specified, and all examples show the Si-nc within the core of the waveguide. Patent [109] lays claim to integrated circuits with sources,

waveguides, switches, and detectors all comprising of Si-ncs in SiO_2. The publication of a patent does not necessarily mean the patent has a legal claim to the property contained therein. Published patents may be invalid (and therefore unenforceable) for a variety of reasons.

2.3.3 Integrated Porous Silicon Emitters

Porous silicon emitters integrated with waveguides have been developed. Reference [110] shows P-Si formed through laterally anodized etching on SOI substrates. The device forms a waveguide in the vertical direction, with the P-Si acting as the core, and SiO_2 and air as the cladding layers, however it appears the device is an anti-guide in the lateral direction since the P-Si is sandwiched between two Si regions. Optically pumped edge emission is reported. In [111], P-Si based transceivers are demonstrated. P-Si/alumina junctions form the optical emitter and detector, and are optically coupled through an air/alumina/P-Si waveguide. It is not clear if there is any guiding in the lateral direction, indeed the lateral width of the device is not reported. The ratio of the LED current to the detector's photocurrent is 0.4 %, although the interconnect distance (ie, separation of the LED and photo-detector) is only 7 μm. It is not clear that guiding has actually been demonstrated considering the propagation length is relatively very short.

Chapter 3. Device Theory of Operation, Design and Fabrication

3.1 Theory of an Integrated Emitter

This thesis describes the design of two types of emitters integrated into planar waveguide platforms. The specific design considerations for DE LEDs and integrated Si-ncs are discussed in sections 3.2 and 3.3 respectively. In this present section, the physical operation of emitters integrated with waveguides is reviewed. These general concepts are also important for the characterization methods described in Chapter 4.

3.1.1 Planar Waveguide Modes

Modal analysis of waveguides has been studied extensively and there are several thorough books on the subject [3, 112, 113,]. The essence of solving the guided modes of the system is to apply Maxwell's equations with the appropriate boundary conditions. For the 1-D problem of a planar slab waveguide comprised

of an arbitrary number of transparent layers, shown in Figure 4, the transverse[9] modal profiles (if there are any supported modes) have analytic solutions. Within each film, the electric and magnetic fields are either sinusoidal or decaying exponentials. For 2-D problems, such as ridges, buried channels, and strips, several analytical approximations and numerical solving methods have been developed.

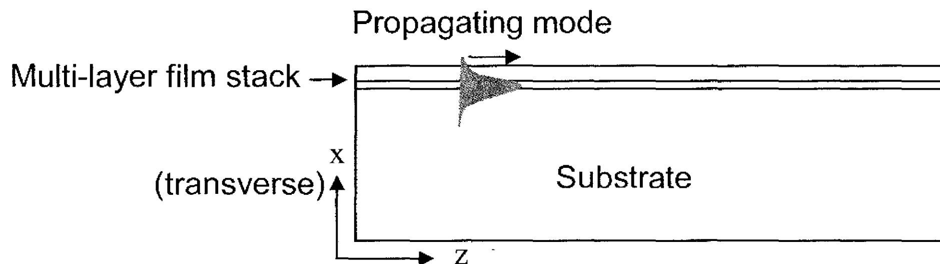

Figure 4: Schematic of an arbitrary slab waveguide, comprised of a multi-layer thin film stack. The films are assumed to extend infinitely in the *y* direction (out of the page). In laying out the solution, the mode is assumed to propagate in the *z* direction. The mode profile varies only in the *x* direction.

The slab waveguide is not particularly useful for commercial devices since it only guides in the transverse direction. The lateral direction is left unguided hence the direction of propagation is arbitrary within the plane of the film stack. Guiding in both the transverse and lateral (x and y) directions, such as in a ridge or channel structure, is required for all application-specific photonic devices.

---

[9] Here, transverse refers to the direction perpendicular to the film plane (x). Lateral refers to the y direction within the plane and perpendicular to the direction of propagation (z). The opposite convention also exists in the literature. In the definitions of TE and TM, 'transverse' refers to the field component (E or H) that lies only perpendicular to k.

However, slab waveguides are useful for research since many of the properties are comparable to ridge structures, while the fabrication is significantly simpler.

In the analytic solution for the modes of a slab waveguide, the governing equations decouple into two differently polarized modes. It is customary to choose z as the direction of propagation. The transverse magnetic polarized (TM) mode consists of the field components E_x, H_y, E_z. The TE polarized mode consists of the field components H_x, E_y, H_z. The electric field for the TE mode is written as

$$E_y = \hat{y}E(x)e^{i(\frac{2\pi N_{eff,TE}}{\lambda_o}z-\omega t)} \quad (6)$$

Here, E_y is the complex electric field of the TE mode and is a vector pointing in the y direction. The actual electric field is the real component of the complex E_y. The quantity ω is the angular frequency of oscillation, t is time, λ_o is the vacuum wavelength, and $N_{eff,TE}$ is the effective index of the TE mode. The co-ordinate system is shown in Figure 4. As the problem is 1-D, E_y varies only in the x direction. $E(x)$ is the mode profile, and is either a sinusoid or a decaying exponential within each layer. The mode maintains its shape as it propagates, ignoring attenuation. Similar equations exist for the two other field components in the TE mode, as well as for the TM mode. For the TE mode, $E(x)$ is continuous across the boundary, but for the TM mode it is discontinuous. The effective index is given by an eigenvalue equation yielding discrete solutions which must

be solved numerically for each of the two polarizations, TE and TM. Depending on the thicknesses and refractive indices of the films within the stack, there may be no solutions for N_{eff} (below cutoff), one solution (single mode), or multiple discrete solutions (multi-mode). An example of the TE and TM modes in a two-layer single mode waveguide is shown in Figure 5. To solve for the effective index of the modes, and the mode shape, code was written based on the analytic solution given by Chilwell [114]. The code was thoroughly tested and found to generate identical results compared to examples provided within reference [114]. Also, good agreement was observed with modes solved using the commercial BPM software package from Rsoft [115].

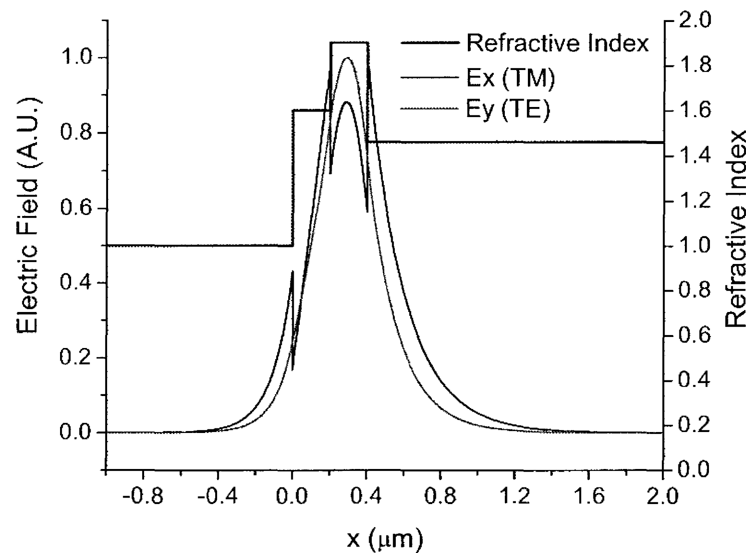

Figure 5: An example of the modal solutions of a slab waveguide. Shown are the TE and TM mode profile of an air/Si-nc/SiN_x/SiO_2 structure. The structure is a two layer slab waveguide formed on a quartz substrate with refractive index 1.46. The waveguide is comprised of two films with refractive indices 1.9 and 1.6, each 200 nm thick. The effective index for the TE and TM polarizations are 1.67 and 1.60 respectively, calculated at a wavelength of 850 nm.

According to equation

(6), the mode propagates in the z direction without attenuation. In reality, some loss is always present. Using perturbation theory, the mode can be approximated as the lossless mode modified by a decaying exponential, $e^{-\alpha z}$. The mode then propagates with the same profile and effective index, but is attenuated by the loss coefficient, α. Loss may be introduced from a variety of sources, such as material absorption, free carrier absorption, Raleigh scattering, and surface roughness [3]. If the losses of the individual films within the stack, α_i, are known, then the total modal loss is given by [116]

$$\alpha = \sum_i \frac{1}{N_{eff}} n_i \Gamma_i \alpha_i \tag{7}$$

$$\Gamma_i = \frac{\int_{x_i} \left|E_{tot}\right|^2 dx}{\int_{-\infty}^{\infty} \left|E_{tot}\right|^2 dx} \tag{8}$$

where α is the total modal loss of the waveguide, α_i, Γ_i, n_i are the material loss, confinement factor (or modal power overlap integral), and refractive index in the ith layer, and the sum is taken over all layers. The waveguide loss must be calculated separately for the TE and TM polarizations. Note that Γ_i is calculated

as the modal overlap of the vector sum of the total electric field, E_{tot}, which for the TM polarization has two components.

Here, α_i has been defined as material loss, and encompasses both absorption and scattering. In both cases, the loss coefficient is uniform throughout the film. In waveguides, another source of loss may be introduced through surface roughness at the interfaces [3]. Further, loss may have wavelength dependence in the spectrum of interest and should properly be written as $\alpha(\lambda)$.

3.1.2 Pumping Methods

The energy for optical emission must be supplied from an external source. In general, the emitter is pumped electrically or optically. In the case of electrical pumping, the device must provide a current path between the emitting region and the electrical contacts. For example, in a *p-n* LED, current is supplied through a *p* and *n* terminal, and EL is generated near the diode junction where injected minority carriers recombine. The terminals are usually either on the top and bottom of the device, or in the case of lateral injection, both terminals may be on the surface. In an LED the rate of carrier recombination is approximately given by I/q, where I is the current, and q is the charge of an electron.

In optical pumping schemes, energy is supplied from an external light source. The device must therefore provide a transparent optical path between the

pump source and emitting region. The pump energy will not entirely be delivered to the emitting material. Pumping will only occur in regions where the pump light is absorbed by the emitting material. In general, the pump light will form a standing wave within the device. A portion of the pump light will reflect (and possibly transmit) from the device, and may be absorbed in regions/processes other than that which is desired.

3.1.3 Coupling of Sources to Waveguides

Light may be launched "end-fire" into a waveguide from external sources, through the end facet. The amount of incident light that will be coupled to the mode (ignoring facet reflection) is given by the overlap integral of the incident light with the near-field mode profile [117],

$$\eta_{coupling} = \frac{[\int E_i E_m^* dx]^2}{\int E_i E_i^* dx \int E_m E_m^* dx} \tag{9}$$

where E_i and E_m are the fields of the incident light from the external source and the modal profile respectively, and the integrals are computed over the facet plane. This is the usual method for hybrid integration of sources (using butt coupling or free space alignment of waveguides), although it is also possible to design an integrated, unguided source coupled to a waveguide in this manner, as shown in Figure 6 (Top). However, since the source region is unguided, the

coupling efficiency of point sources located a distance r from the facet will diminish approximately as $1/r^2$.

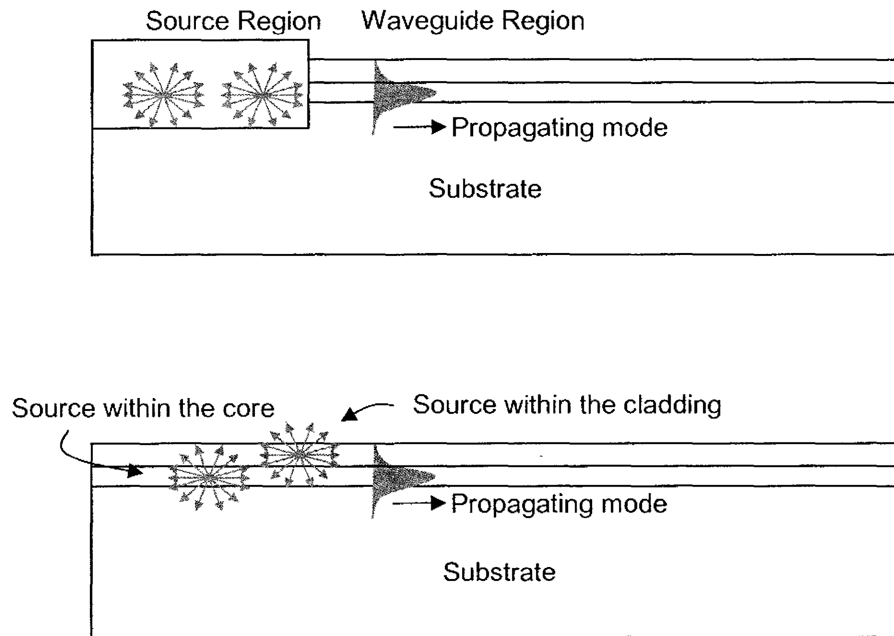

Figure 6: (Top) Schematic of a hypothetical unguided emitter integrated through "end-fire" coupling to a planar waveguide. It is assumed that the source region itself does not support any guided modes. (Bottom) Schematic of an integrated emitter with sources in the core and cladding of a waveguide. For simplicity, in both figures only two point sources within the emitting material are shown. These two schematics are for illustration purposes, and ignore how such structures might actually be fabricated.

In this thesis, sources were instead placed within the waveguide volume, as shown in Figure 6 (Bottom). In well-established guided sources, such as diode lasers and fiber lasers, the emitting material is usually in the waveguide core, as opposed to the cladding volume. The spontaneously emitting layer may be considered a collection of uncorrelated point sources. Energy is radiated in a

continuum of directions, and therefore each source will excite not just guided modes, but all radiation modes as well. Radiation modes are plane waves propagating in a continuum of angles, and carry energy away from the core and into the surrounding regions [113]. The ratio of the power coupled to a given waveguide mode, m, to the total power emitted by a source is defined here as the spontaneous emission factor,

$$\beta_m = \frac{Power\ \ coupled\ \ to\ \text{mode}\ m}{Total\ \ power\ \ emitted} \tag{10}$$

A rigorous calculation of β for a dipole source located in an arbitrary position within an arbitrary multi-layer waveguide is a difficult problem in the field of electricity and magnetism. Analytic solutions have been developed for symmetric waveguides, although asymmetric waveguides require numerical techniques, as summarized in [118].

The spontaneous emission factor is an important physical parameter influencing the operation of diode lasers, and approximate solutions based on modal analysis have been developed for that application. There, the simplifying assumption is that the total rate of spontaneous emission for a source located within a stack is close to that of an identical source located instead in a homogenous medium of refractive index n. Assuming uncorrelated dipole sources of identical strength, homogenously distributed, and randomly oriented within the core layer, β is found to be proportional to the overlap integral of the modal power with the emitting layer volume, Γ [119, 117]. Sources located

outside the core of the waveguide have been considered for various fiber applications [120, 121], and result in a similar relation. This yields the intuitive result that the coupling strength of an embedded source with a waveguide mode is proportional to the power of the mode profile at the location of the source.

In [122], a simpler approach is taken. The profile of a mode within the waveguide (called the near-field) is reconstructed as a spectrum of plane waves. According to Fourier optics, the far-field profile of the mode is the near-field's plane wave spectrum. The near-field and far-field mode profiles are approximately Fourier transform pairs [123]. A source is considered to emit plane waves uniformly in all 4π sr. The spontaneous emission factor is then estimated as the ratio of the entire plane wave spectrum of the mode with the total 4π sr. For a ridge or channel waveguide with a Gaussian mode shape, assuming paraxial angles and ignoring the obliquity factor,

$$\beta = \frac{\sigma_x \sigma_y}{2n^2} \quad \textbf{(11)}$$

where σ_x and σ_y are the $1/\sqrt{e}$ half widths of the far-field mode power in radians, and n is the refractive index of the active region [122]. Perfect coupling between the source and mode for axial plane waves is assumed. Equation (11) is therefore an upper limit for β, within the framework of the model. In a slab waveguide, there is no lateral guiding. However, in a real experiment the collection optics will only capture a sliver of the mode over the total 2π circumference. For a slab

waveguide, making the same approximations leading to Equation (11), β can be reworked by treating the guided and unguided directions separately. The portion of the total emission in the x direction is treated as in [122], and the portion in the y direction is assumed to be determined by the collection optics. This leads to

$$\beta = \frac{\sigma_x \Delta\theta_y}{2n\sqrt{2\pi}} \tag{12}$$

where $\Delta\theta_y$ is the subtended full angle of lateral observation within the film, and does not include refraction at the facet in the y direction.

For the integrated emitter shown in Figure 6 (Bottom), the total power coupled to the guided mode from an infinitesimal emitting region at z will be determined by the rate equation,

$$\frac{dP}{dz} = J\eta_{pump}\hbar\omega\eta_{\text{int}}\beta - \alpha P \tag{13}$$

Here, J is the external pumping rate density (electron-hole-pairs generated per time, within the element dz) and η_{pump} is the pumping efficiency, the product of which combine to form the rate of electron-hole pair generation in the wedge, dz, and represents an average over the area in the xy plane. For an LED, η_{pump} is close to 1 since most of the current provides minority carrier injection. For optical pumping, only a fraction of the pump light will be absorbed in the emitting region, the rest either being reflected, transmitted, or absorbed elsewhere. Of the excess carriers, only the fraction, η_{int}, will recombine radiatively, emitting a photon of energy $\hbar\omega$. Of the emitted light power, the fraction β will couple to the

mode of interest. The mode will propagate along the guide experiencing a loss of αP in each element of dz. Assuming a constant pumping rate density along the device ($J(z)=J_{total}/L$), the total power at the end of a device of length L is,

$$P = \frac{\frac{J_{total}}{L}\eta_{pump}\hbar\omega\eta_{\text{int}}\beta\left(1-e^{-\alpha L}\right)}{\alpha} \tag{14}$$

$$\eta_{power} = \frac{P}{J_{total}\hbar\omega_{pump}} \tag{15}$$

Here, ω and ω_{pump} are the angular frequencies of the emission and pump light respectively. Equation (14) gives a simple description of the operation of an integrated emitter[10]. However, the equation does not reveal the interdependence between the terms with respect to actual design parameters such as film index, thickness and device length. Optimizing the power efficiency of the device is an involved process that requires tradeoffs among the various parameters. For example, consider the influence of the emitting layer thickness on the power efficiency, η_{power}. As discussed earlier, both β and α are proportional to the overlap of the mode with the emitting layer, Γ. Therefore, increasing the layer thickness will increase β and α by the same proportion. If Γ is increased to $\varepsilon\Gamma$, equation (14) reveals that the net effect is an increase in P through the bracketed

[10] Incidentally, this equation is also a simple description of the “variable stripe length” (VSL) method.

term, which now becomes (1-$e^{-\varepsilon\alpha L}$). However, depending on the device in question, increasing the emitting film thickness may alter η_{pump} and/or η_{int}.

As another example, equation (14) reveals that decreasing the length of the device increases the power efficiency. However, depending on the emission mechanism, the magnitude of η_{int} may decrease with increasing J, and will certainly exhibit a maximum J above which damage to the emitting material will occur.

3.2 Design and fabrication of Defect Engineered LEDs

For this thesis, defect engineered light emitting diodes were designed, fabricated, and characterized. The purpose of the devices was to migrate the defect engineering (DE) method from bulk Si wafers onto an SOI platform. While the goal of such a project is to achieve monolithically integrated LEDs coupled with the SOI waveguide, this thesis work focused on the initial step in that evolution, surface emission. The following two sections describe the design and fabrication of the DE structures studied in this thesis.

3.2.1 Design of defect engineered LEDs

Recall that the DE technique consists of a boron (*p*-type) implant followed by thermal annealing. When performed on an *n*-type substrate this creates a *p-n* junction which operates as an LED when in forward bias. Minority carrier

injection across the junction results in radiative recombination at the band edge. In samples co-implanted with Er, emission at 1.5 μm is also observed. On the SOI platform, a buried oxide prevents the use of metallic *n*-type contacts on the substrate backside. Both the *p* and *n* contacts must therefore be placed on the top surface, in a lateral injection scheme. (Such a scheme is suitable for bulk Si samples as well, though is not necessary). To obtain electrical contact with the *n*-type material, there are at least two possibilities. The boron implant may be performed uniformly across the surface, and the Si overlayer may be selectively etched below the junction to the n-type material. Alternatively, masked implantation may be performed.

A masked implant is a more elegant solution since it does not alter the geometry of the Si:air interface, which is a likely contributor of non-radiative centres. Further, it is difficult to accurately control the etch depth of the heavily implanted Si overlayer. However, the ion implanter used in this thesis has a large 6 inch implant diameter, and beam time is precious. To make use of available implant time, it is preferable to implant a large sample once, rather than multiple smaller samples. To achieve a masked implant on a large sample requires a large photolithographic mask. This increases the fabrication cost by several thousands of dollars, compared to the Si-etch processing route, where smaller samples and masks are utilized. For these reasons, *n*-contacts were fabricated by etching through the *p*-region of uniformly implanted Si.

Accurate knowledge of the junction depth was required to ensure that the Si-overlayer was etched sufficiently deep to access the *n*-type material. Further, some samples, prior to application of the DE technique, were implanted with phosphorous, an *n*-type dopant. (This was done to decrease the resistance of the of the *n*-type electrical contact, and to explore the efficiency of differently doped junctions. Also, one sample tested was made on p-type material with a boron concentration of $\sim 10^{17}$ cm^{-3} and therefore required a counter doping *n*-type implant for junction formation.)

The implant and annealing recipes were simulated using the software package, ATHENA [124]. A Dual-Pearson implantation model was used to simulate the implantation and thus allowed exploration of the implant profile, while a Fermi diffusion model was used to simulate the post-implant annealing steps. Erbium implant tables and diffusion properties are not available in ATHENA, but the implant may be simulated with the Monte-Carlo program, SRIMS. The annealing step after the Er implant was quite short to limit diffusion [81]. Simulations resulting in dopant profiles from the DE process are shown in Figure 7. The junction depth is approximately at the depth where the boron concentration is equal to substrate's background doping level (usually near 10^{15} cm^{-3}), which is seen to occur near 480 nm. An example of the simulation of samples pre-implanted with phosphorous are shown in Figure 8. In that process, the extra implant resulted in a slightly shallower junction depth near 380 nm, depending on the annealing time.

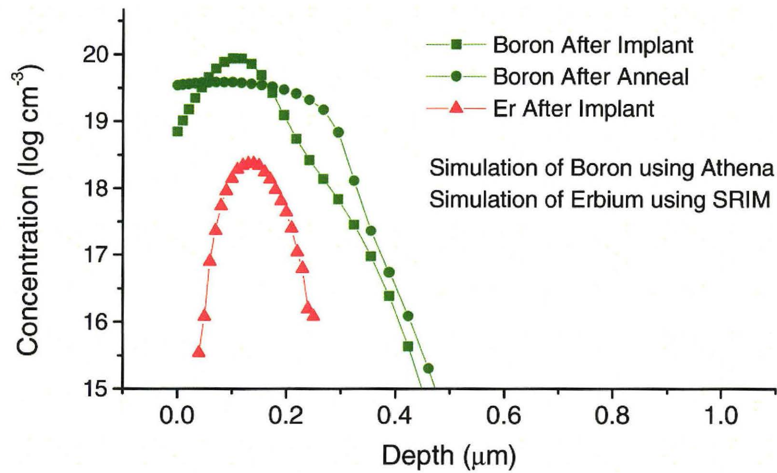

Figure 7: Simulation of the implant and diffusion profile of boron and erbium in the DE process (Route C, and C:Er). Boron is implanted at an energy of 30 keV, with a dose of $1*10^{15}$ cm^{-2}, followed by a 20 minute tube furnace anneal in N_2 at 950 °C. The Er profile is calculated after a 0.4 MeV implant with a dose of $2*10^{13}$ cm^{-2}.

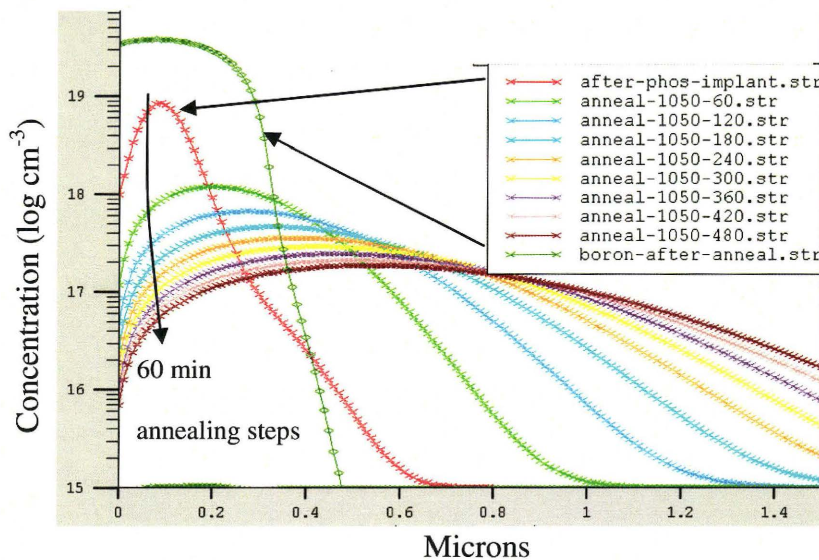

Figure 8: Simulation of phosphorous implantation (Route B) with an energy of 80 keV, and a dose of $1*10^{14}$ cm^{-2}. Shown are the phosphorous concentrations after implantation and after annealing at 1 hour intervals, starting at 60 minutes at 1050 °C in N_2. Also shown is the boron concentration (highest curve, circles) of the subsequent DE process. The DE process occurs at a lower temperature (950 °C) than the phosphorous anneal, and therefore does not significantly alter the phosphorous profile. In all cases, the junction depth is seen to occur

near 380 nm. The phosphorous diffusion profile is not affected by the finite thickness of the Si overlayer, for thicknesses as low as at least 5 μm.

A cross section schematic of the LED design with surface contacts is shown in Figure 9 (Top). Current is injected laterally, as opposed to the previously used design where current is injected through the substrate. The active region is defined by the Si etch. EL is generated on either side of the junction region as carriers recombine. Emission will occur in all directions, and undergo multiple reflections within the cavity. Electroluminescence is collected out the bottom side of the substrate. The structure is designed with cylindrical symmetry. The *p*-type contact is a disk, whereas the *n*-type contact forms a concentric ring. For such a design, depending on the device dimensions, there is possibly large current density non-uniformity across the active region. In this initial work, current non-uniformity is not considered further; however, a variety of diameters and contact spacing lengths were included in the mask design. The active region mesa diameter is made to vary from 50 μm to 1000 μm in diameter. To allow a degree of misalignment between mask layers, the *p*-type contact pad diameter is 20 μm smaller than the mesa diameter. The spacing between the *p* and *n*-contact perimeters varies from 25 to 130 μm. The etch depth depends on the substrate doping, typically between 0.7 and 1.0 μm. In the wet-etch processes, the resulting side walls are not vertical, but are sloped at an angle that depends on the anisotropy of the etch and the crystal orientation. LEDs are also formed with a

bottom side n-contact, shown in Figure 9 (Bottom). Such a design is only suitable for bulk substrates.

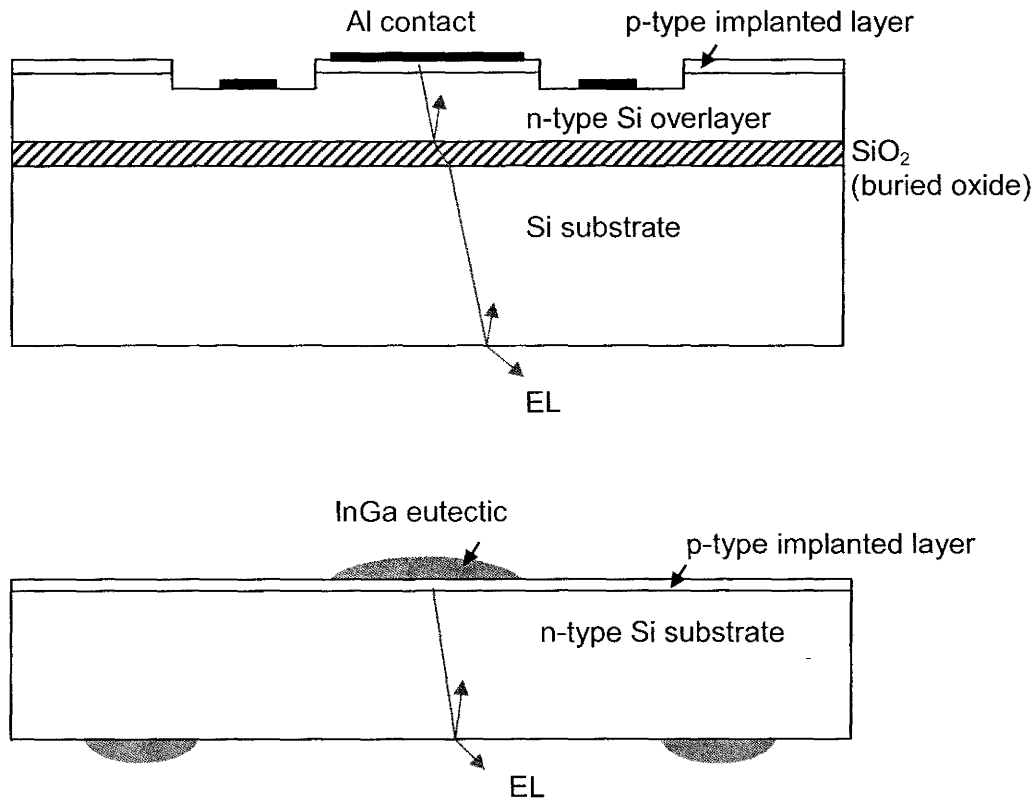

Figure 9: (Top) Cross section of a lateral injection LED made on SOI. Both electrical contacts are formed on the top surface. (Bottom) Cross section of an LED with contacts on the top and bottom surfaces made on bulk Si. While either design may be applied to bulk Si substrates, lateral injection is necessary for the SOI platform. In both devices, EL is collected out the bottom surface.

3.2.2 Fabrication specifics of defect engineered LEDs

Several starting substrates were used in this work, and are documented in Table 1. All substrate normals have a <100> crystal orientation. The bulk Si

samples were formed from device-grade Czochralski (CZ) grown Si. SOI substrates were purchased from Shin-Etsu, formed from the "bond and etch back" method. Properties of different layers within the substrate are denoted by layer1/ layer2/, etc.

Table 1: Starting substrates for DE LEDs.

Structure	Thickness (μm)	Resistivity (Ωcm)	Type
CZ Bulk Si	388	5-10	n
Epitaxial Si/CZ	7.5/765	(0.1-0.2)/(12-16)	p
5 μm SOI	5.0/1.0/725	28	n
1.5 μm SOI	1.5/1.0/725	34	n

The implantation and annealing recipes are shown in Table 2. The table is interpreted by reading down each column. An "x" indicates a step that was included in the route. For example, route C, shown in the last column, is the DE process, whereby samples received a boron implant followed by a 20 minute anneal at 950 °C. Route C:Er, is the DE process co-implanted with Er. Routes A and B are pre implanted with phosphorous.

Two batches of samples were implanted and annealed at the University of Surrey's Ion Beam Centre, and are referred to as Surrey I (performed in my absence) and Surrey II (performed in my presence). In the first batch, only boron and erbium were implanted. In the Surrey II batch, phosphorous was additionally implanted and annealed in some samples. On account of this extra implant and anneal, routes C and C:Er were modified to include a Step 2 anneal, although this anneal is not expected to have had an impact on the virgin wafer. An * denotes

this additional anneal received by the Surrey II batch. The list of samples fabricated in Surrey I and Surrey II are shown in Table 3 and Table 4 respectively.

Annealing was performed in two dedicated quartz tube furnaces for boron and phosphorous activation and diffusion. During the furnace anneals, the samples were slowly inserted and withdrawn into the heat zone over a 2.5 minute period. Erbium samples were annealed in a rapid thermal processor.

Table 2: Preparation routes for the implantation and annealing of LED fabrication.

Step	**Preparation Route**					
	A	**B**	**C**	**A:Er**	**B:Er**	**C:Er**
1A Implant Phos, 80 keV, $5*10^{12}$ cm^{-2}	■			■		
1B Implant Phos, 80 keV, $1*10^{14}$ cm^{-2}		■			■	
2 Anneal Nitrogen, 1050 °C ~2-3 h	■	■	* *	■	■	* *
3 Implant Boron, 30 keV, $1*10^{15}$ cm^{-2}	■	■	■	■	■	■
4 Anneal Nitrogen, 950 °C, 20 min	■	■	■	■	■	■
5 Implant Erbium, 0.4 MeV, $2*10^{13}$ cm^{-2}				■	■	■
6 Anneal Nitrogen, 950 °C, 1 min				■	■	■

Table 3: Sample List for Surrey I

Substrate	Route
5 µm SOI	C
1.5 µm SOI	C
5 µm SOI	C:Er
1.5 µm SOI	C:Er
Bulk Si	C:Er

Table 4: Sample List for Surrey II

Substrate	Route
Bulk Si	A
Bulk Si	B
Bulk Si	C*
Bulk Si	A:Er
Bulk Si	A:Er
Epitaxial Si	A
Epitaxial Si	B
Epitaxial Si	A:Er
Epitaxial Si	B:Er
5.0 μm SOI	A
5.0 μm SOI	B
5.0 μm SOI	A:Er
5.0 μm SOI	B:Er

After implantation and annealing, some samples were fabricated to make LEDs (shown in Figure 9, Top) using wet etching and metalization. Two types of standard Si wet etches were used [125]. In the Surrey I samples, etching was performed using a KOH etch, described as follows. Samples were deposited with 100 nm of SiO_2 using PECVD. The SiO_2 was patterned using photolighography and a buffered HF acid etch. KOH was used to anisotropically etch the Si to a depth of 700-1000 nm , as monitored with an alpha stepper. The KOH solution used was H_2O:KOH:isopropona1 alcohol with mass ratio of 8:12:3. The solution was held at 50 °C by a water bath. This solution is a standard Si etch solution, with an etch rate on low doped <100> Si of ~180 nm/min. However, boron is a known etch stop for KOH etching. The etch rate through the DE layer was observed to decrease to ~20 nm/min, and to not etch uniformly. Although the KOH etch method successfully formed a working LED structure, the Surrey II samples were instead etched using the isotropic etch solution HNO_3:H_2O:49% HF

50:20:3 by volume, at room temperature. In this etch, a photoresist mask was used. Although better uniformity was achieved with the HNO_3 etch, the etch rate was very fast (1.2 μm/min), and sometimes cracked and peeled the photoresist. These are known properties of the HNO_3 etch. In retrospect, a dry etch process would have been a preferable fabrication method.

After the Si etch, electrical contacts were formed using a "lift off" process. A 120 nm thick Al film was thermally evaporated onto the sample, pre-patterned with photoresist. The regions with photoresist were then "lifted off" using an acetone bath.

Bulk LEDs were also fabricated with bottom side *n*-contacts. These were fabricated using InGa eutectic, which was dabbed on using toothpicks. The InGa droplets were then immobilized with a coating of silver paint. The process is undeniably crude, and was difficult to control the contact size and position. However, the process was simple, and resulted in ohmic contacts. The design was limited to bulk Si samples since a buried oxide would have prevented current flow. Bulk Si LEDs were fabricated using both designs shown in Figure 9.

3.3 Design and fabrication of integrated Si-ncs

3.3.1 Design of integrated Si-ncs

Two waveguide structures are considered in this work, and are shown in Figure 10. In the two-sectioned device, Figure 10 (Top), a Si-nc layer is integrated with a SiN_x core waveguide. In the emission section, a Si-nc layer forms the upper cladding of the waveguide. When optically pumped from above, Si-nc emission is coupled into the waveguide mode. However, the Si-nc layer also introduces a large propagation loss. For this reason, the emission section is coupled to a low-loss Si-nc free transmission section. This allows the generated light to propagate with lower loss, as would be desirable in a photonic circuit. This design also increases the modal overlap with air[11] in the transmission section, improving the utility for evanescent sensors with integrated emitters.

In the conventional design, Figure 10 (Bottom), a thick Si-nc layer forms the waveguide core. As is discussed in section 2.3.2, this design is very common in the literature due to its simplicity and it suitability to explore stimulated emission in Si-ncs. However, there are several disadvantages in this conventional design for device integration. The low index contrast between core and cladding results in waveguides that require thick films, have wide modes, and have large

[11] In an evanescent sensor, the top cladding material to be "sensed" may be contained in a liquid such as a water or alcohol solution, instead of air. The higher refractive index of these liquids (typically near 1.3) would in an increased modal overlap with the liquid compared to an air cladding.

modal overlaps with the core resulting in high loss propagation. Such devices would be required to be pumped in all regions and are best suited for short propagation lengths. In comparison, the two-sectioned device uses SiN_x which exhibits low propagation loss in the visible regime, is VLSI compatible, and has a relatively high refractive index allowing for smaller waveguide dimensions.

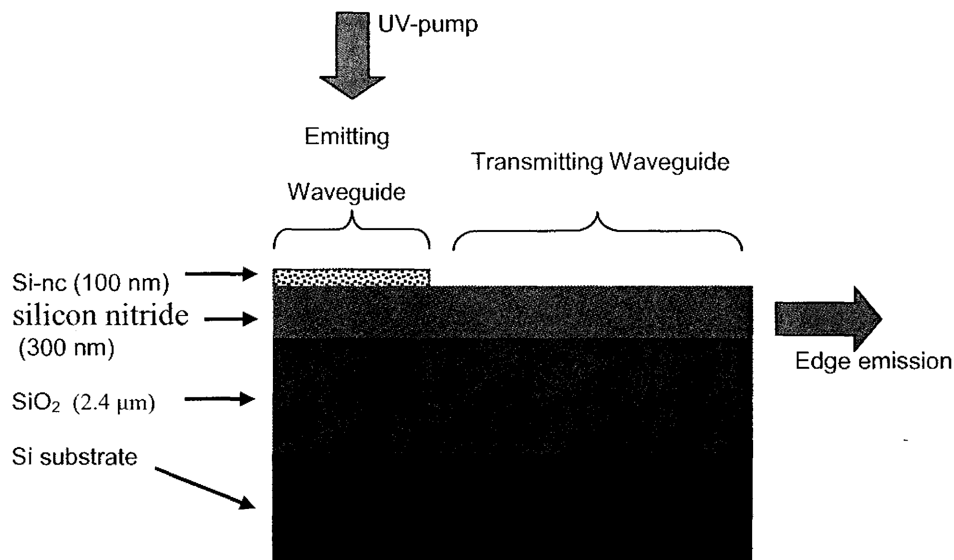

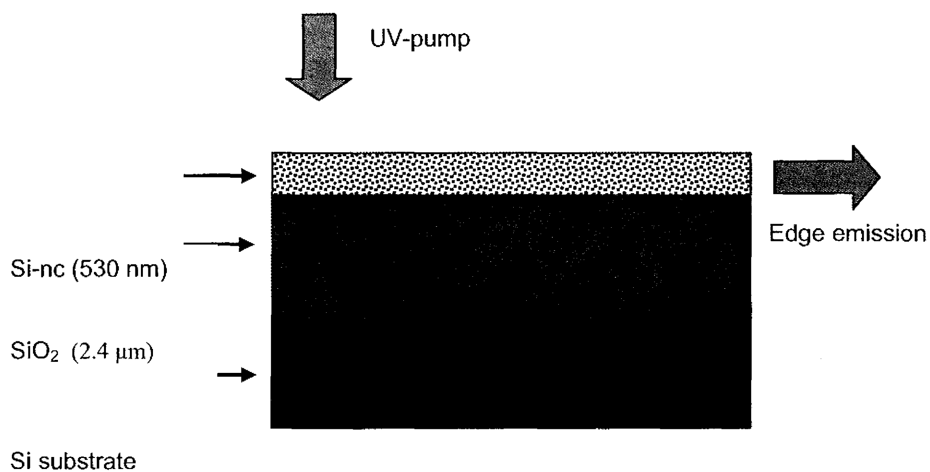

ıematic of a two-sectioned waveguide with integrated Si-nc transmission section, coupled to a low-loss transmission section. (Bottom) Schematic of a conventional Si-nc core slab waveguide.

Silicon nitride was chosen as the waveguide core due to its transparency in the optical region of interest, its high refractive index (~1.9) relative to SiO_2 which permits small waveguide dimensions, and its VLSI compatibility. The design allows control of the modal overlap with the Si-nc layer (and hence the loss), and the ability to couple to low loss transmitting regions using a simple fabrication procedure. There is a large parameter space that yields single mode operation while simultaneously keeping the mode tail away from the absorbing Si substrate, and having only a small coupling loss between the two waveguide sections. Silicon nitride waveguides on Si have been studied for a number of years [126], but the majority of that work has concentrated on the propagation of light in the 1.5 μm wavelength telecommunication band, and on the closely related but more versatile SiON material system [127]. Recently, there has been renewed interest in silicon nitride photonic circuits operating in the visible region for applications such as optical interconnects in computers [128]. The two-sectioned device makes use of the developing field of SiN_x photonic circuits.

In the design of the two-sectioned device, the SiN_x core remains an uninterrupted plane for passive alignment and is placed below the Si-nc layer so as not to act as a diffusion barrier to H_2, a known enhancer of light emission efficiency in Si-ncs.

The refractive indices of the films were measured using spectroscopic ellipsometry. The refractive index of the Si-nc and SiN_x films at 850 nm were

~1.6 and 1.9 respectively, and showed only a small material dispersion in the band of interest. Based on the thickness and index of the films, the mode intensity overlap integrals, effective indices, and beam propagation were calculated. For example, results are shown in Table 5 for a conventional and two-sectioned device. The coupling loss between the emission and transmission sections, assuming an infinitely abrupt transition, is simulated to be 0.09 and 0.18 dB for the TE and TM modes, respectively. Here, coupling loss is defined as the loss experienced by the fundamental mode of the emission section as it propagates through the transition point and into the transmission section, and is calculated as $-10\log(P_T/P_E)$, where P_E and P_T are the mode power on the emission and transmission sides of the transition. The coupling loss is due, primarily, to the spatial mode mismatch of the two sections.

Three chip designs are presented in this thesis. The first is shown in the schematic of a two-sectioned device, Figure 10 (Top). A 2.4-3 μm thick bottom SiO_2 cladding is used, although simulations show that a cladding thickness as thin as 500 nm is sufficient to achieve less than 0.01 dB/cm of loss from absorption of the mode tail in the Si substrate. The thickness of the SiN_x core is selected to be 300 nm. This results in a single mode waveguide far from cutoff, with a low coupling loss between the emission and transmission sections. As the thickness of the SiN_x core is increased, the waveguide remains single mode until a core thickness of ~390 nm. At this thickness, the TE polarization in the emission section has two modes. As the SiN_x core thickness is decreased, cutoff of the

fundamental mode will occur at a core thickness of ~150 nm (assuming an infinitely thick bottom SiO_2 cladding). This takes place first in the TM polarized mode of the transmission section. In reality, the bottom cladding thickness is finite, and the Si substrate will significantly absorb mode power with core thickness greater than the cutoff of 150 nm. This is demonstrated in Figure 11. Such loss can always be avoided by increasing the thickness of the bottom SiO_2 cladding. Note also that as the SiN_x core is decreased, the coupling loss between the two sections will increase, though will remain relatively low, as shown in Figure 12. The preferred thickness of the Si-nc layer is selected to be 100 nm, since that thickness overlaps the majority of the mode tail, yet is thin enough to be "lifted off" from the transmission region during fabrication. Devices with 200 nm thick Si-nc layers are also fabricated. The waveguide properties of the emission and transmission sections of a two sectioned device, calculated at a wavelength of 850 nm, are given in rows 1 and 2 of Table 5.

Table 5: Waveguide mode properties of the conventional and two-sectioned devices shown in Figure 10, calculated at 850 nm. The two-sectioned device consists of a 300 nm thick SiN_x core, with a 100 nm thick Si-nc film in the emission section. The conventional design consists of a 530 nm thick Si-nc core.

Structure	N_{eff}		TE Modal Overlap (%)				TM Modal Overlap (%)			
	TE	TM	SiO_2	silicon nitride	Si-nc	air	SiO_2	silicon nitride	Si-nc	air
Emission	1.73	1.67	9.7	80.8	8.0	1.5	22.0	61.4	10.9	5.7
Transmission	1.71	1.62	12.6	82.7	--	4.7	32.1	55.8	--	12.1
Si-nc core	1.54	1.52	14.9	--	83.2	1.9	24.9	--	71.1	3.9

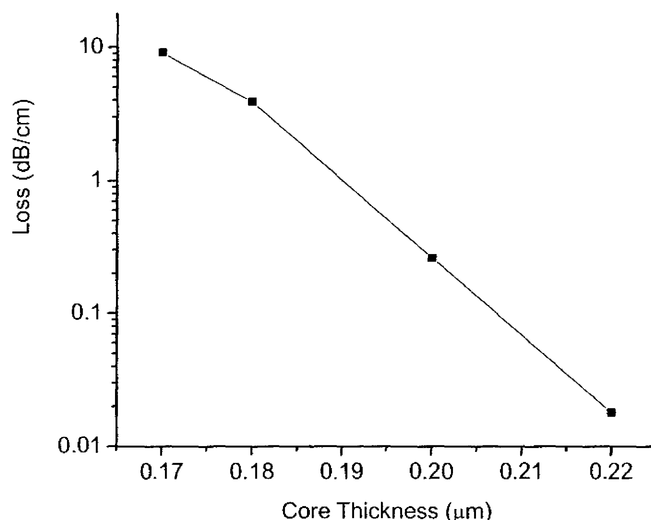

Figure 11: Simulated waveguide loss in an air/SiN_x/SiO_2 waveguide grown on a Si substrate. Loss is introduced by absorption of the mode tail in the Si substrate and is calculated for the TM polarization at a wavelength of 850 nm using a variety of SiN_x core thicknesses. The SiO_2 cladding is kept at 2.4 μm. The simulation is performed using R-soft BPM software. Note that it is very difficult to directly solve for the mode of this structure with the Si substrate present in the simulation. To perform the simulation, the mode shape is first solved using BPM's mode solver with an infinitely thick SiO_2 cladding. This "loss-free" mode solution is then launched into the structure with the Si substrate present, and the total power in the waveguide is monitored as a function of propagation distance.

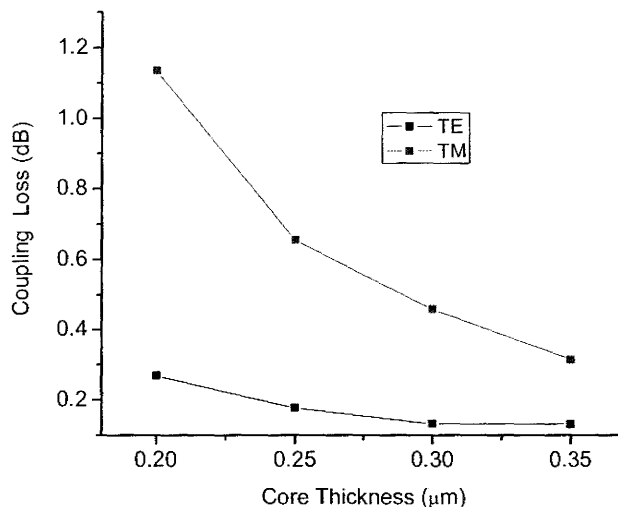

Figure 12: Simulation of the coupling loss between the emission and transmission sections of a two-sectioned device with varying SiN_x core thicknesses. Simulations are performed at a wavelength of 850 nm. To obtain worst case results in the simulations, a 200 nm thick Si-nc layer is used as opposed to the 100 nm thick Si-nc layer in used in Table 5.

In order to make isolated measurements of the optical properties of the SiN_x and Si-nc films, two additional waveguides were also designed. The first design is a nitride core waveguide which is identical to the transmission section of the two-sectioned device shown in Figure 10 (Top). The optical properties of this waveguide are therefore identical to row 2 in Table 5. The second design is a Si-nc core conventional waveguide that employs a 530 nm thick Si-nc core with a 2.4-3 μm thick SiO_2 bottom cladding, shown in Figure 10 (Bottom). The Si-nc layer thickness is selected in order to achieve a waveguide above cutoff, with a mode tail that does not extend into the Si substrate. The properties of the Si-nc core waveguide are given in the third row.

The far-field half-width $e^{-1/2}$ intensity pattern of the mode in the emission section of the two-sectioned device is calculated to be 23.3° and 20.5° for the TE and TM modes respectively. From equation (12), β of the slab structure is $0.044\Delta\theta_y$, calculated using the average of the two polarizations.

3.3.2 Fabrication specifics of integrated Si-nc waveguides

SiN_x and SiO_x were deposited using ECR-PECVD (electron cyclotron resonance, plasma enhanced chemical vapor deposition), and the details are discussed elsewhere [129, 130]. The work in this thesis utilizes those results. The refractive indices at 850 nm were typically 1.9 and 1.6 for SiN_x and SiO_x

respectively. The refractive index of SiO_x films deposited in the chamber has been previously calibrated as a function of Si content using Rutherford backscattering. Here, the Si content is interpolated to be x=1.7. Unfortunately, the SiN_x deposition has not been calibrated, although based on the refractive index and on calibrations of SiO_xN_y deposited films, the Si content is expected to be close to stoichiometric Si_3N_4. Although in-situ ellipsometry was available in the deposition chamber, such monitoring is difficult for multi-layer films. Instead, the desired thickness of each deposited film was targeted using previously measured deposition rates. This typically resulted in a deposition thickness within 5% of target values.

Samples were deposited on either Si substrates, on thermally oxidized Si substrates (with an oxide thickness of 2.4 or 3.0 μm), or on fused silica substrates. In the former two cases the Si substrates were p-type, lowly doped to 1-100 Ωcm with boron, oriented in the <100> direction, and were grown by the CZ method.

To fabricate a patterned Si-nc layer after deposition of the SiN_x layer, the SiO_x deposition was masked using either a glass cover slide or using photoresist. In the latter case the SiO_x was selectively removed via a photoresist lift-off process using a bath of AZ 400T stripper, heated to 50 °C, placed in an untrasonic cleaner. In the masked region, the two methods (glass slide, or resist lift-off) yielded chips with identical loss within the measurement uncertainty. As an alternative to masked deposition, post-deposition etching of the SiO_x layer is

possible. However, this was not attempted since a high selectivity (~1:30) wet etchant is not readily available, while dry etching roughens the core and introduces significant excess loss.

The photoresist liftoff process was performed using a staircase mask pattern. This resulted in sections of varying lengths, as shown in Figure 13. While edge emission can be collected out of any of the 4 facets, such a design was useful for measuring the coupling loss between the emission and transmission sections by comparing the SES edge emission (SES is discussed in Chapter 4) along paths A-D.

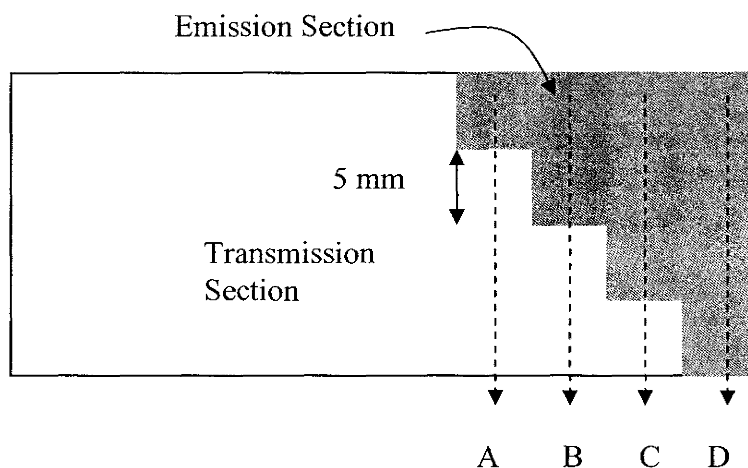

Figure 13: Staircase pattern of a two sectioned device. This top view schematic shows the transmission sections (white) and emission sections (grey). Edge emission from 4 different excitation paths of the SES setup are shown by the dashed lines, A-D.

After deposition and processing, the samples were cleaved, then annealed using one of three recipes:

- A: 1100 °C in N_2 for 2 hrs

- B: 1100 °C in N_2: 5% H_2 for 2 hrs
- C: 1100 °C in N_2 for 2 hrs, followed by 500-600 °C in N_2: 5% H_2 for 2 hrs

The latter route is henceforth referred to as the two-step anneal. Unless otherwise stated, all single step anneals were performed at 1100 °C for 2 hours. A few samples were instead annealed using Ar_2 or Ar_2: 5%H_2, depending on the availability of N and Ar gas cylinders. Annealing was performed in a dedicated quartz tube furnace. The temperature was monitored using a thermocouple placed in close proximity to the samples. Prior to inserting the samples into the heat zone, the tube was purged with the annealing gas. Gas flow, maintained throughout the anneal, was directed to a bubbler flow valve to prevent air from entering into the furnace. Samples were slowly inserted and removed from the heat zone over a 7 minute period to minimize thermal shock.

In a previous study, similarly prepared SiO_x films deposited using the same chamber (but with flow rates yielding a slightly larger x=1.78 and annealed for 1 hour longer) were shown by glancing X-ray diffraction to contain Si-ncs with a mean diameter less than 2 nm [129]. It is noted that the PL spectra reported in [129] and from this report have the same shape and peak wavelength. It is therefore concluded that the films here contain similarly sized Si-ncs. Si-nc density measurements have not been performed. However, if it is assumed that the excess Si and SiO_2 matrix have the same density of bulk Si and thermal SiO_2

respectively, and that all excess Si forms spherical nanocrystals with a diameter of 2 nm, the Si-nc concentration (ncs/volume) is estimated to be $2*10^{19}$ cm^{-3}.

To compare the emission properties of the deposited films, a Si-nc sample was also formed from ion implantation. Si ions were implanted into a thermally oxidized film with an energy of 90 keV, with a dose of $7.4*10^{16}$ cm^{-2}. The implanted sample was then annealed for 70 minutes at 1100 °C in N_2, then for 130 minutes at 500 °C in N_2: 5%H_2. The implantation was performed at the University of Western Ontario. Such a recipe has been shown by others to produce Si-ncs of a similar size and density to the films deposited here. For example, reference [131] characterizes samples implantation at 100 keV with a dose of $8*10^{16}$ cm^{-2}. After annealing for 60 minutes at 1100 °C, Si-nc with mean diameters of 3 nm are formed at a concentration of $4*10^{18}$ cm^{-3}.

In Chapter 5, results from the Si-nc devices are presented. For clarity, sample names are assigned to the more heavily discussed devices. Table 6 documents these sample names, and the corresponding structure and fabrication recipe. In Chapter 5, an effort is made to provide a brief description of the sample in close proximity to its presentation. This is done to avoid a frequent need to refer to Table 6.

Table 6: A partial Si-nc sample list. Column 1 shows the sample name. The first three digits correspond to one or two depositions on a sample. An "x" signifies the sample has been cleaved into multiple samples prior to annealing. For example, 051x1, 051x2, 051x3 were fabricated from the same deposition but were annealed separately. The substrates were either Si or thermally oxidized Si. The depositions are listed from the surface down, in the opposite order in which they were deposited. SRSO indicates deposition of silicon-rich-silicon-dioxide (or SiO_x). For example, 034x1 is an air/SRSO/SiN/SiO_2:Si waveguide on a silicon substrate.

Sample Name	Substrate	Deposition (nm)	Annealing Route	Pattern method
014x8	3 μm SiO_2	SRSO 100	B	
014x9	3 μm SiO_2	SRSO 100	1000 °C for 2 hours in A_2:H_2	
014x10	3 μm SiO_2	SRSO 100	900 °C for 2 hours in A_2:H_2	
015x6	3 μm SiO_2	SRSO 300	C	
016x3	3 μm SiO_2	SRSO 500	C	
034x1	3 μm SiO_2	SRSO/SiN 200/100	C	
034x2	3 μm SiO_2	SRSO/SiN 200/100	B	
035x1	3 μm SiO_2	SRSO/SiN 200/300	C	
051x1	2.4 μm SiO_2	SiN 300	No anneal	
051x2	2.4 μm SiO_2	SiN 300	A, then 500 °C in N_2:H_2 for 2 hours, then 600 °C in N_2:H_2 for 2 hours	
051x3	2.4 μm SiO_2	SiN 300	B, then A	
053x3	Si	SRSO 100	B	
053x4	Si	SRSO 100	A	
070x1	2.4 μm SiO_2	SRSO/SiN 100/300	A	Glass slide
071x1	2.4 μm SiO_2	SRSO/SiN 100/300	A (but for 1.5 hours instead of 2 hours)	Lift off
080x1	2.4 μm SiO_2	SRSO/SiN 200/300	A	Lift off

Sample Name	Substrate	Deposition (nm)	Annealing Route	Pattern method
Implanted	2.4 µm SiO_2	Implant Si 90 keV $7.4*10^{16}cm^{-2}$	1100 °C for 70 min in N_2 Then 500 °C for 130 min in N_2:H_2	

Chapter 4. Measurement Techniques

4.1 Surface emission from multi-layer film stacks

Photoluminescence (PL) is indispensable as a diagnostic tool since it allows non-destructive characterization of the luminescence properties prior to device fabrication. Interpretation of PL from SOI structures is not straightforward owing to the optical cavity formed by the high refractive index contrast of the silicon overlayer and the buried oxide. A full correction procedure to enable comparison of samples of varying dimensions is described below. The method is tailored to PL in SOI, although the procedure is general to multi-layer films, and to different pumping methods, such as electrical.

In multi-layer films, PL generated within the emission overlayer undergoes wide angle and multi-path interference, as shown in Figure 14 for emission in SOI. The interference effect on the PL is very sensitive to the refractive indices of the films, layer thicknesses, observation angle, and wavelength. Depending on the film stack, the modulation period may be smaller or larger than the PL spectral width, hence the presence of interference is not always obvious. Interference of luminescence generated in thin films has been described analytically by Lukosz et al. in [132]. However, in the specific case of light emission from Si, analysis of the interference effects have often made little use of the body of knowledge available, and in some cases have even been

neglected altogether leading to false conclusions. This deficiency has only recently been acknowledged, and the topic is receiving renewed interest [85, 133] and has pointed out explicitly [134].

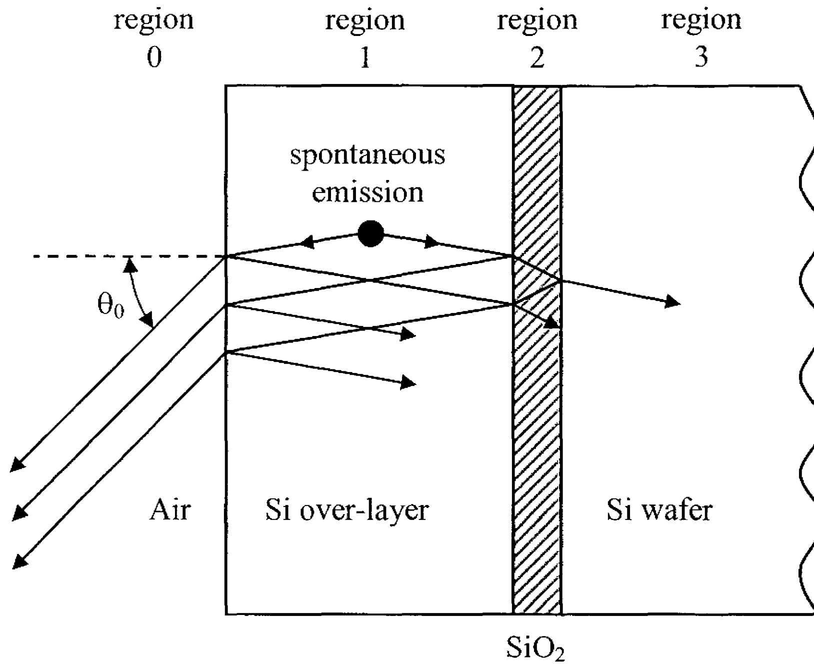

Figure 14. Schematic showing the origin of interference of spontaneous emission generated within the Si overlayer. The entire overlayer is emitting uniformily, but for clarity only emission from a small volume, at one observation angle, is shown.

Here, the cavity modulation effect is modeled following the analytic description of luminescence in thin films given by Lukosz in [132]. The emitting film is taken to be a collection of incoherent dipole oscillators of equal strength, oriented over all directions, and uniformly distributed throughout the film over a depth, H, of the layer. Emission is assumed to occur in the material region from

the surface to a depth, H. H is less than or equal to the thickness of the emitting film, x_1. The films are considered to be isotropic, planar, and transparent. The substrate is taken to be infinitely thick. Such an approximation implies that the interference period from reflections off the bottom substrate surface is beyond the resolution of the detection spectrometer. The collection medium is assumed to be air. For uniform emission throughout the emitting layer, and with $k_zH>>1$, the interference function of the film resembles its transmission spectrum [132]. Here, k_z is the wavevector component (in layer 1) in the surface normal direction, and x_1 is the thickness of the emitting layer. Under this condition, wide angle interference is negligible and emission is more simply described as uncorrelated forward and backward plane waves generated within a layer of a dielectric stack [135]. In this restricted circumstance, the observed time-averaged PL is proportional to

(16)

$$I = <|\delta(\lambda)|^2> \frac{t_{10}^2(1+|r_{12}|^2)}{|1-r_{10}r_{12}e^{i\phi}|^2} = <|\delta(\lambda)|^2> F$$

(17),

$$\phi = \frac{4\pi n_1}{\lambda} x_1 \cos(\theta_1)$$

where θ_1 is the observation angle in region 1 and t and r are the Fresnel transmission and reflection coefficients. The two subscripts indicate the boundary

of regions 0, 1 and 2 corresponding to air, Si overlayer, and buried oxide respectively as shown in Figure 14. Here, r_{12} is an effective (complex) reflectivity accounting for the buried oxide layer and has not been expanded for clarity. Equation (16) describes F for a single layer film. Additional layers, such as the burried oxide, are easily accounted for using an "effective" reflectivity for layers to the left or right of the emission layer. The matrix method is well suited to calculate the effective reflectivity [135]. The quantity $<|\delta(\lambda)|^2>$ is the time averaged spontaneous emission spectrum generated within the Si overlayer, and is the true (or "intrinsic") emission spectrum unmodified by the interference function, F. The function F is interpreted as the output from a white light source located within the Si overlayer. For the modeling described here, the average of both polarizations from equation (16) is taken, and is found to well-approximate the solution derived by Lukosz for all SOI films considered in this thesis.

Code was written to apply the model. The code was verified to result in values in agreement with examples given in [132], as well as transmission functions given in [135]. Other simple checks on the code were performed. For example, at normal incidence the TE and TM polarizations of F are identical, as expected. When all film indices in the stack are set to be equal, a constant F is produced. The fringe period of F, which is easily calculated in stacks that contain one film which is thicker than all the others, is correct.

To apply the model and obtain the intrinsic emission, it is possible to simply divide the observed surface emission, I, by the calculated F. However, F is a periodic function requiring accurate optical constants. To add credibility to the fit, it is desirable to obtain $<|\delta(\lambda)|^2>$ another way. This can be accomplished either from samples that contain no films (ie, an emitting substrate), or in samples contained in stacks that result in an F with a sufficiently flat band as to introduce negligible modulation. In the case of SOI, the former is easily accomplished using bulk Si. In the case of Si-nc, Si-nc films may be deposited on quartz[12]. This intrinsic emission, multiplied by the appropriate F, should then resemble emission from the multi-layered film. The underlying assumption is that the intrinsic emission spectrum is not affected by the presence of the film stack.

This technique is conceptually similar to that described in [134] and [136] which model the emission of Si-nanocrystals in dielectric films. However, as is shown in section 6.1, specific structure and properties of silicon (and SOI) require additional considerations and a separate approach to determine the model parameters different from those described in these works. In previous works specific to SOI, [85, 86, 137], F is taken to be equal to the transmission of the

[12] For single layer Si-nc films with a thickness <700 nm and index of ~1.6 deposited on Si, distortion from the interference effect is small. Similarly, edge emission from Si-nc waveguides also resembles the intrinsic emission spectrum.

system which is a reasonable approximation when $k_z H >> 1$, but in the general case underestimates the fringe contrast of F.

Surface PL spectra from silicon structures were obtained using the apparatus at the University of Surrey, shown in Figure 15 (Top). The samples were held at room temperature, and pumped with 60-210 mW of 514.5 nm light from an Ar ion laser. Surface emission was collected by a lens, and directed to a grating spectrometer. The angle of incidence of the pump laser and the angle at which PL is collected was not well controlled[13]. Output from the spectrometer was detected with a Ge *p-i-n* detector, cooled with liquid nitrogen. Lock-in detection was used. The spectral response of the system was calibrated using a thermal light source.

Surface PL spectra for Si-nc films were obtained using the setup shown in Figure 15 (Bottom). Samples, held at room temperature, were optically pumped with 17 mW of 325 nm light from a HeCd laser. The beam waist was measured to be 1 mm in diameter. PL was collected perpendicular to the surface plane by a lens, and was directed to the multi-mode fiber input of an Ocean Optics CCD array spectrometer. The spectral response of the system was determined using a calibrated Ocean Optics thermal source.

---

[13] Measurements taken by staff in the Surrey lab did not include a collection angle. In their apparatus, the sample is free to rotate about all angles, with no accurate alignment tools. In measurements taken by me on unimplanted SOI, the collection angle was measured to be between 55-60°.

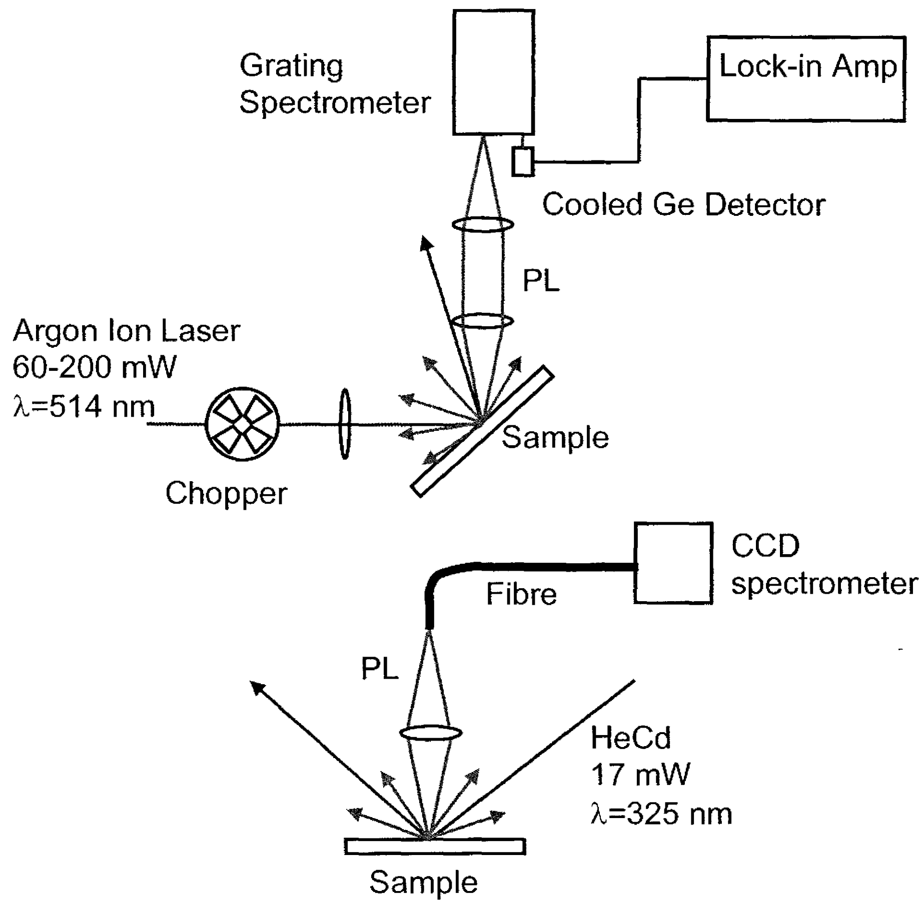

Figure 15: Schematic of experimental setup for measuring surface PL spectra. (Top) PL setup for Si samples. (Bottom) PL setup for Si-nc samples.

4.2 Emission efficiency

In an emitting device, a parameter of great physical and engineering interest is the emission efficiency. The three most commonly quoted types of

efficiencies are the power efficiency, internal quantum efficiency, and external quantum efficiency, η_{power}, η_{int}, η_{ext} respectively. While η_{power} usually relates the ratio of the emitted usable power to the power supplied to the device, the quantum efficiencies give the ratio of the rate of radiative carrier recombination to total carrier recombination. Whereas η_{int} is defined as the quantum efficiency within the device, η_{ext} takes into account the fact that not all the generated light will be emitted from the device. Measuring emission efficiency is a problem in the field of radiometry. Accurate measurements of efficiency require the use of calibrated power meters, as well as careful consideration of the collection geometry.

The following is a derivation of the relationships between the measured emission power, η_{int} and η_{ext}. Consider Figure 16, where light is generated inside a material through either optical or electrical excitation. It is assumed that the material has a higher refractive index than its surroundings. The emitted light then travels to the surfaces (ignoring absorption/scattering). Only the fraction, f_{TIR}, of the light incident at angles less than the critical angle, θ_{cr}, will transmit through the surface. Although the interface is planar and not spherical, f_{TIR} is always approximated to be the ratio of the surface area of the cone subtended by the critical angle of the material/air interface with that of a full sphere. Modeling the emitting film as a point source, $f_{TIR}=(1-\cos\theta_{cr})/2$. Further, it is approximated that light throughout the escape cone undergoes the same normal incident Fresnel transmission, resulting in further loss of $T=1-R$, where R, T are the reflection and

transmission coefficients respectively. While this description is employed universally in the literature, it ignores reflections from bottom layers and therefore cavity effects.

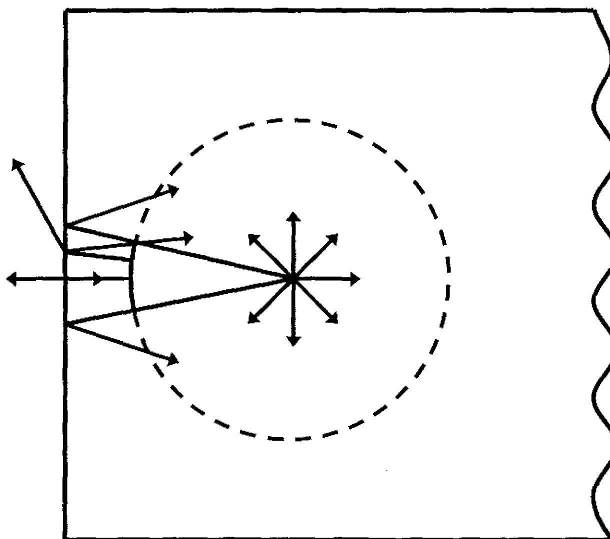

Figure 16: Schematic of a point source within a material emitting over 4π str. Only rays within the escape cone escape the material.

Of the light emitted through the half sphere of the surface, not all will be collected by the power meter. Power meters have finite areas, and are sensitive to the direction of incident light. At large angles, the light will strongly reflect. Power meters are often calibrated only for near normal incident light. A lens or lens pair can be used to direct light from the source to the power meter. A lens will capture only a fraction of the emitted light, f_{lens}=(1-cosθ), where θ is the half

angle subtended by the lens. There are three issues with this type of experimental setup[14]. The first is that the system must be well aligned. The second is that it is assumed that the limiting aperture is the first collection lens, not any subsequent lenses, or the power meter. Note that the object is an extended source, and not a true point source. It is assumed that the collection efficiency is constant over the entire source. The third issue is that power meters are wavelength sensitive, and are calibrated to measure one narrow band at a time. To properly measure a wide band signal, or multi-band signal, a spectrometer is required. However, if the power meter is set to the centre of the emission band, it still provides a reasonable approximation of power. Indeed, if the emission spectrum is symmetric about its centre λ, and if the meter's wavelength responsivity is linear with λ over the emission band, then there is no error at all.

The internal and external quantum efficiencies are then related by

$$\begin{aligned} \eta_{ext} &= \eta_{\text{int}} f_{TIR}(1-R) \\ &= \eta_{\text{int}} \frac{1-\cos\theta_{cr}}{2}(1-R) \end{aligned} \quad \textbf{(18)}$$

[14] A more elegant solution would be to use an integrating sphere, with the source placed inside or at the entrance of the sphere. The advantage of integrating spheres is that the ambiguity of geometry and alignment are removed. However, integrating spheres direct only a small amount of light to the detector and are therefore not suited for low signal measurements. Additionally, integrating spheres require accurate calibration, and spheres are very expensive compared to lenses.

for the case of emission in Si, where n=3.55, η_{ext}=0.014η_{int} ; for the case of Si-nc's with n=1.6, η_{ext}=0.10η_{int}.

In LEDs, the rate of carrier injection is given by I/q, where I is the current, and q is the charge on one carrier. The photon detection rate is given by $P/(hc/\lambda)$, where P the optical power, h is Planck's constant, and c is the speed of light. The η_{ext} and the detected power are related by

$$\eta_{ext} = \frac{P}{I}\frac{q\lambda}{hc}\frac{1}{f_{lens}} \quad \textbf{(19),}$$

Note that the above definition of η_{ext} includes all light emitted from the hemisphere of the device surface. The usefulness of this is questionable since no optical system is able to make use of emission throughout the entire hemisphere. However, it is the standard definition.

For optically pumped devices, such as those using Si-ncs, equation (18) is still valid, although the rate of carrier excitation is given by $A/(hc/\lambda_p)$, where A is the pump power absorbed, and λ_p is the pump wavelength.

(19) is then modified to

$$\eta_{ext} = \frac{P}{A}\frac{\lambda}{\lambda_p}\frac{1}{f_{lens}} \quad \textbf{(20),}$$

Measurement of A is accomplished by subtracting the reflected and transmitted pump power from the incident pump power. This assumes all loss is due to

material absorption, and ignores other loss sources such as Raleigh scattering, and scattering from dirt on the surface.

The experimental setup for the LED characterization is shown in Figure 17. The LED was contacted using metal probes, and was biased with a curve tracer. For accurate voltage and current measurements, a Keithly 179A digital multimeter was inserted into the circuit. The LED was rested on a 1.6 mm thick copper sheet, and positioned over a 5 mm through-hole. Emission from the bottom of the LED was directed to a power meter using a gold mirror, and two plano-convex lenses. The lenses were AR coated, are 25.4 mm in diameter, and have focal lengths of 25.4 mm. The setup was aligned such that the first and second lenses are positioned to be one focal length from the LED and the power meter respectively. The lenses were positioned two focal lengths apart in the beam path. The detector was an ILX FPM 8200 power meter, specified to have 5% accuracy, with a circular active area with a diameter of 3 mm. Due to the long path length, not all the optical power collected by the first lens was coupled to the power meter. The setup was calibrated with a more accurate butt coupling setup, and found to read power measurements a factor of ~1.9 times too small. In the butt coupling setup, EL was measured with the LED placed 4.6 mm from the power meter.

The power meter wavelength was set to 1.1 μm. For samples not implanted with erbium, this gives a reasonable estimate of the EL power. For samples implanted with erbium, emission is contained within the two 1.1 μm and

1.5 μm bands. To quantify the power within each band, two measurements were taken at each current bias, with and without a long pass filter placed within the beam path. The filter transmits light longer than 1300 nm with a transmittance of 85%. The EL power contained within the two bands was then calculated, taking into account the different responsivity of the power meter at the two wavelengths.

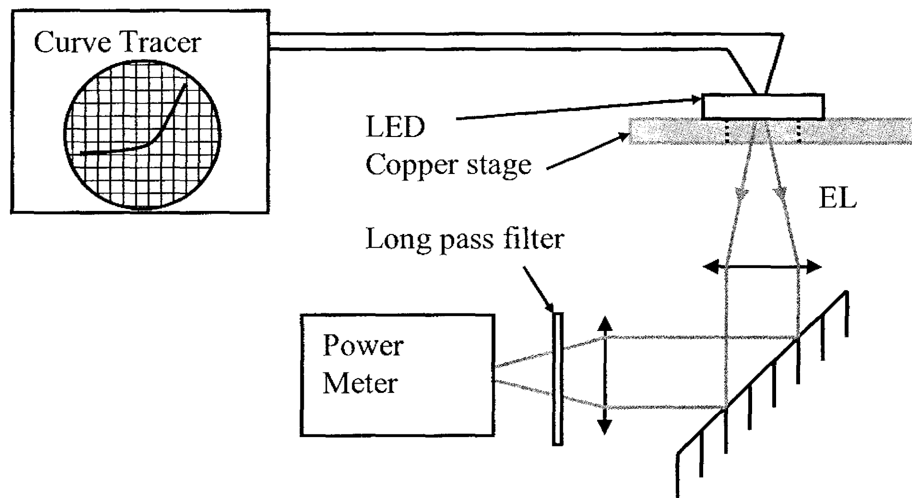

Figure 17: Experimental setup diagram used for LED characterization.

Figure 18 shows the setup used to measure the optically excited η_{ext} of the Si-nc films. Since the absorbed pump power must be measured, Si-nc films deposited on Si substrates were not appropriate, since an unknown quantity of pump power would be absorbed in the Si substrate. Efficiency was therefore only measured on films deposited on silica. An Ophir PD 300-UVcalibrated power meter, with 3% accuracy, was positioned and repositioned to sequentially measure the incident pump power, reflected pump power, transmitted pump power, and PL

power. The pump light was oriented with the electric field aligned to the plane of incidence/reflection/transmission, and directed to an angle of incident with the sample close to Brewster's angle. This minimized the reflected power to an insignificant level, and increased the path length of the pump light through the sample, increasing the absorbed power. PL was collected at normal incidence using an AR coated 35 mm focal length lens, with a diameter of 25.4 mm. The lens was placed 58 mm from the sample surface. A 3 mm thick RG665 glass filter was used to block pump light. Due to the low signal level of the PL power, care was taken to avoid all sources of background light, such as room lighting, instrument light and stray pump light.

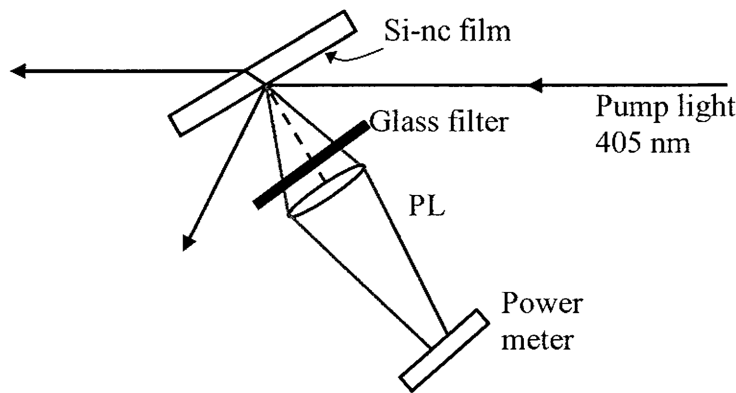

Figure 18: Experimental setup used to measure PL efficiency of Si-nc films.

4.3 Waveguide properties

Waveguide properties of the integrated Si-nc devices, such as N_{eff}, and α, were measured using a prism coupling set. Prism coupling is a method whereby light is coupled from the evanescent tail of a totally internally reflected beam into

a waveguide mode using frustrated total internal reflection, as shown in Figure 19 (Top). Coupling occurs when the propagation constants in the *z* direction matches the propagation constant of the waveguide mode. The phase matching condition is given by the simple relation [138],

$$N_{eff} = n_p \sin(\theta_p) \tag{21}$$

where n_p is the refractive index of the prism. A high refractive index prism, with $n_p > N_{eff}$, is required. For strong coupling, the air gap should be close to the wavelength of light.

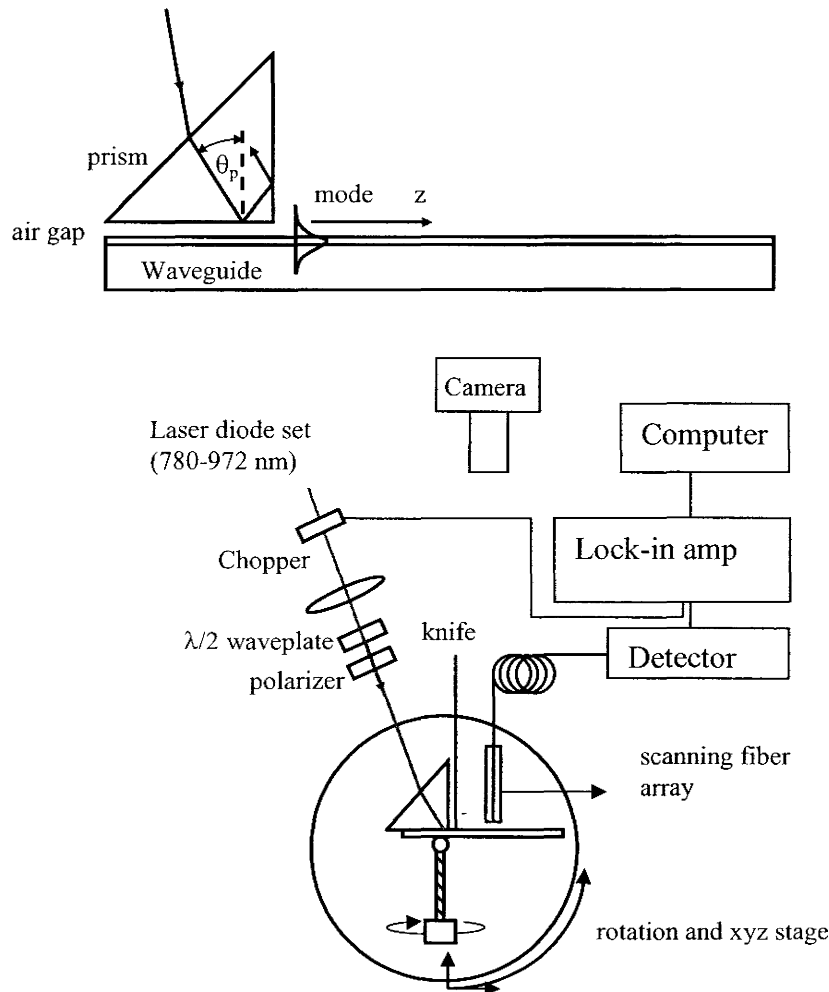

Figure 19: Prism coupling diagram showing the measurement of N_{eff} and α. (Top) shows prism and waveguide arrangement. (Bottom) shows a schematic of the experimental setup.

The experimental setup is shown in Figure 19 (bottom). The prism coupler setup used a right angle rutile prism, with two 45° corners. Rutile is birefringent, having a refractive index at 633 nm of 2.58 and 2.87 in the ordinary and extraordinary directions respectively. Collimated laser diode light was directed toward the prism coupler setup. A set of continuous wave 5 mW single

mode laser diodes were interchanged to obtain measurements at 780, 850, 892 and 972 nm. The laser light was focused with a 150 mm lens. The lens was positioned such that the focal point was at the bottom corner of the prism. This coupling method is particularly useful for slab waveguides since the light remains approximately collimated in the unguided waveguide direction. To accomplish the same feat with butt coupling would require the fabrication of ridges. To control the air gap, the waveguide and prism were gently pressed together using a turn screw. A ball bearing was placed between the screw and back of the sample, slightly bowing the sample and forming the coupling point. The prism was secured to the stage with a teflon clamp (not shown in diagram). The sample and prism were placed on a rotation stage, and *xyz* stage. The axis of rotation was positioned within the prism to minimize the distance the beam wandered from the coupling spot as the setup was rotated. A $\lambda/2$ wave plate and polarizer were used to change the polarization of coupling light to obtain both TE and TM measurements. The angle at which coupling is achieved is a measurement of N_{eff}[15], as described by equation (21). When coupling is achieved, a streak is visible (with a silicon camera) along the length of the waveguide. The accuracy

[15] A more accurate method, called the m-line method, exists for measuring N_{eff}. The intensity of the totally internally reflected laser beam, after exiting the prism, can be monitored as a function of angle. At modal coupling angles, the light is partially coupled to the waveguide, causing a local minimum in the reflected intensity:angle curve. If viewed on a screen, a dark line appears through the reflected beam [138]. The m-line method is not heavily used in this thesis since it requires orienting the prism with its hypotenuse against the sample, and establishing a coupling point near the hypotenuse centre. This is not a desirable setup for loss measurements.

of the rotation stage for measuring angle introduces as an uncertainty in the effective index measurement of ~ +/- 0.03. A photograph of the streak generated in a prism coupled waveguide is shown in Figure 20. The streak is due to surface scattered light from the propagating mode. Scattering occurs inhomogeneously along the waveguide due to scratches, dirt, and defects, but also occurs homogeneously from Raleigh scattering and from surface roughness. The intensity decay of the streak can then be measured to obtain the waveguide loss, with the inhomogeneous component of the scattering introducing noise. This method of loss measurement is commonly used by others [112]. The surface scattered light was collected using a linear array of 12 multimode fibers, positioned close to the waveguide and translated along the streak in the direction of propagation, parallel to the waveguide surface. An array of fibers was used instead of one fiber to allow for misalignment between the propagating mode direction and the fiber translation direction. The fiber array was oriented perpendicular to the propagation direction. The length of the fiber array was larger than the width of the streak; hence the collection efficiency was constant across the measurement. The spatial resolution of this system was measured to be much smaller than required to resolve the decay curve. At the other end of the fiber array, a *p-i-n* biased Si diode detected the fiber coupled light. The detector was connected to a lock-in amplifier, communicating with an acquisition computer using GPIB and LabView. A knife was positioned on the prism face to block stray beams exiting the prism. For waveguides that exhibit high loss, only a

short streak was detectable. To make use of as much of the streak as possible, the setup was aligned with a coupling point as close as possible to the right angle corner of the prism. This also reduced back-coupling of mode light into the prism, since the prism ended close to where coupling occurs. Although the coupling efficiency into the waveguide is very sensitive to positional changes of the setup, once aligned, the signal did not drift over the measurement time.

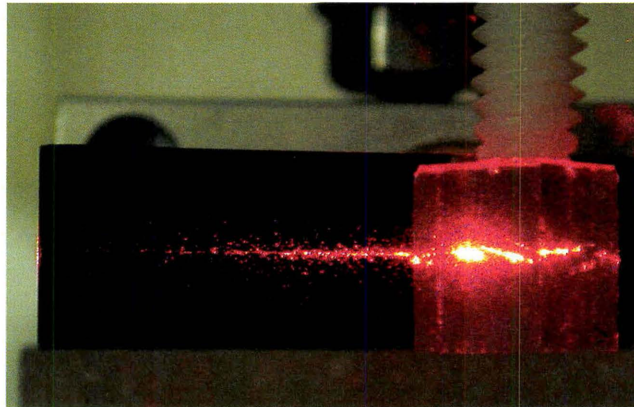

Figure 20: Photograph of the streak generated from prism coupled light. In this example 633 nm laser light is coupled to an air/SiN_x/SiO_2:Si waveguide.

The prism coupling setup was also used to search for gain in Si-nc waveguides. The setup, shown in Figure 21, monitors the facet emission of prism coupled probe light. A 405 nm pump laser beam, expanded using a cylindrical lens, was aligned with the coupled probe streak. The pump light was continuous wave, while the probe light was chopped at the lock-in reference frequency. Direct measurement of pump light was therefore rejected. To search for gain, probe light was monitored with and without the pump light. This method has been used by others [139].

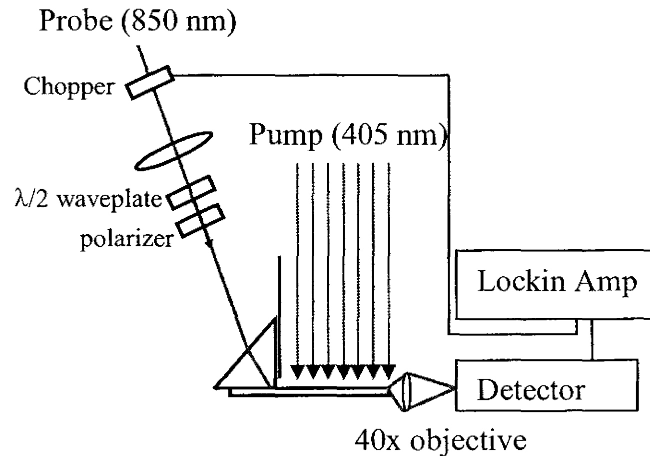

Figure 21:Pump probe setup used to measure gain in Si-nc waveguides.

Thus far, the waveguide characterization methods discussed rely on externally coupled light sources. In waveguides containing Si-nc films, some PL couples into the waveguide mode and therefore may serve as a probe to measure the propagation loss. This was accomplished in the "scanning excitation spot" (SES) technique [96]. In the SES technique, a surface pumped laser spot is scanned across the device while monitoring the edge emission, as shown in Figure 22. The pump laser generates PL within the Si-nc film. The PL couples to radiation modes which leak power into the air and substrate, as well as setting up standing waves within the films. More importantly, a portion of the generated PL is also coupled to the guided mode of the waveguide, as discussed in section 3.1.3. The guided mode propagates to the edge of the device, experiencing a waveguide loss, $e^{-\alpha z}$. A plot of the edge emission power versus z is therefore a measurement of loss. This assumes α is wavelength independent. In general, loss

is wavelength dependent, and the decay of power experienced by the propagating mode is given by

$$P(z) = \int S(\lambda) e^{-\alpha(\lambda) z} d\lambda \tag{22}$$

where $S(\lambda)$ is the PL power coupled to the guided mode at z=0. It is assumed that $S(\lambda)$ is equally generated at any given spot along the scanning path.

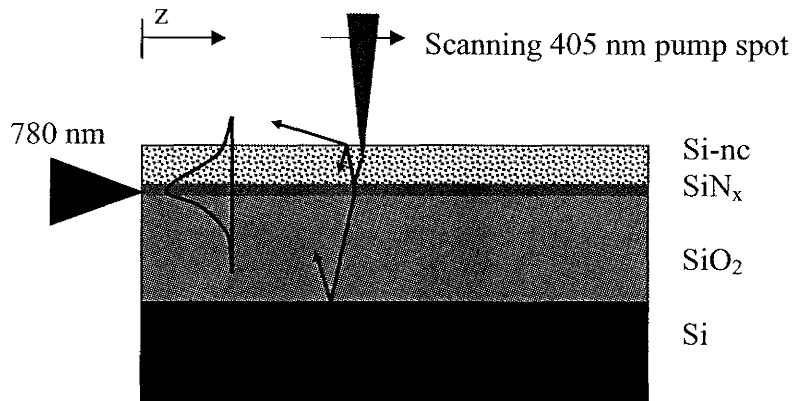

Figure 22: SES measurement technique. A pump laser is scanned in the z direction while monitoring edge emission. Radiation modes are excited in a continuum of directions, although for clarity, only one angle is shown. The guided mode is also excited, and is shown propagating towards the exit facet. Since the waveguide has no confinement in the plane of the film, guided modes will actually propagate in all 2π directions in the film plane.

There are two major complications associated with the SES method. In [96, 97], it is pointed out that a system dependent loss may exist depending on the collection optics. In [98, 148], concerns are raised over differentiating between the radiation modes and the guided mode. Each of these issues will now be described.

The presence of a system dependent loss is obvious when the SES setup is viewed from a top-view, as shown in Figure 23. Since the waveguide does not confine light in the lateral direction, the guided mode propagates in all 2π directions within the waveguide plane. However, only a portion is collected by the detection optics. Consider the high magnification setup in Figure 23 (Top), where the collection lens is positioned with the focal point near the facet, as would be desirable for maximum light collection. The detector aperture is placed in the image plane of the facet. As the excitation spot is moved further from the facet, two effects are apparent. The first effect is that the collection angle subtended by the lens will decrease. This lowers the collection efficiency of the lens, introducing a component of system loss. The second effect is that the excitation spot is no longer in focus, and eventually an excitation spot position is reached whereby the detector, instead of the front lens, becomes the limiting aperture. This combined system loss is an artifact of the measurement setup, and can be severe. It should also be noted that astigmatism of the image is present. Whereas the PL diverges from the excitation spot in the lateral direction, the mode is confined in the transverse direction, and diverges from the facet at the far field angle. Regardless of the position of the excitation spot, in the transverse direction the light diverges from the facet plane. As well as introducing system loss into the measurement, the form of the SES measurement will deviate from a simple exponential decay [97], although the size of the form of the deviation depends on

measurement optics. Further, deviations from a simple exponential may also be introduced in other ways, such as through a wavelength dependent $\alpha(\lambda)$.

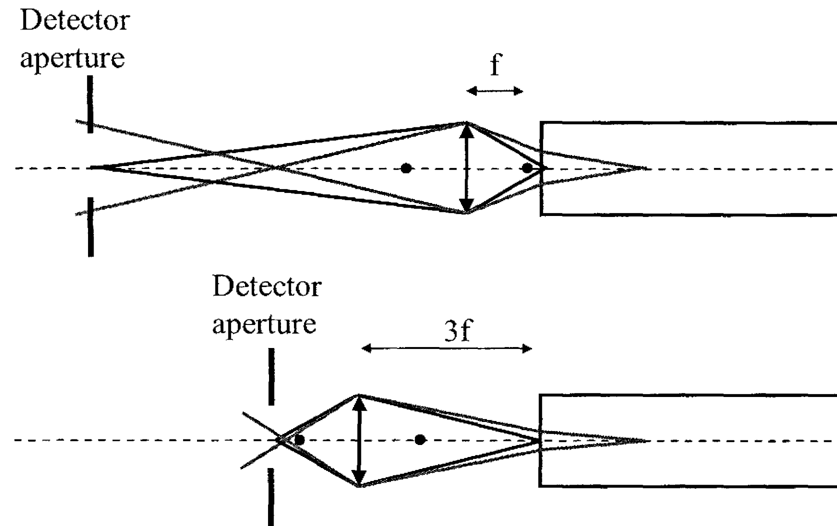

Figure 23: Top-view of the SES measurements showing the introduction of system loss. (Top) diagram shows a high magnification arrangement with the lens positioned a distance slightly larger than *f* from the facet. (Bottom) diagram shows a low-magnification setup with the lens positioned a distance 3*f* from the facet. In each diagram, the detector aperture is positioned at the facet image plane. Two excitation spots are considered in each setup.

The system loss can be reduced by adopting a low-magnification setup, shown in Figure 23 (Bottom). The lens is positioned several focal lengths away from the facet. Compared to the high magnification setup, as the excitation spot is translated away from the facet, a smaller change of collection angle is introduced. Similarly, the excitation spot image does not change its position as severely. Hence larger scanning lengths are possible before the detector becomes the limiting aperture.

The difference in loss measurements made using either the high or low-magnification setup can be very large. For example, in an air/Si-nc/SiN_x/SiO_2

waveguide, using a 25.4 mm diameter lens with a focal length of 35 mm, the low-magnification setup resulted in a loss measurement of 14.0 dB/cm, whereas the high magnification setup (with the detector placed 1 m from the lens) resulted in a loss measurement of 19.5 dB/cm.

The low-magnification setup, while minimizing system loss effects, is a broad band measurement. The PL has a broad, ~150 nm wide spectrum, the loss in the waveguide may be wavelength dependent, and the detector has a spectral response. For these reasons, it is desirable to collect SES edge emission using a spectrometer. Here, a 1/2 m grating monochromator was used. The monochromator's slit widths were set to 600 μm, resulting in a resolution of ~8 nm. The setup, shown in Figure 24, was designed to avoid introducing system loss. To accomplish this, the spectrometer as placed as close as is technically convienent to the facet. Two lenses were used to couple edge emission into the spectrometer. A 25.4 mm diameter lens, with a focal length of 50 mm was positioned 50 mm from the facet. While a longer focal length lens would further reduce system loss, it would couple less light resulting in an insufficient signal strength. A periscope was used to rotate the image of the facet to align with the vertical entrance slits of the spectrometer. A 25.4 mm diameter lens with a focal length of 150 mm was used to couple light into the monochromator. Although the facet image was magnified, the image was rotated. The entrance slits aperture the facet image in the perpendicular waveguide direction, which has a very small image size, and does not distort with increasing excitation spot positions.

The SES measurement, collected through the monochromator was performed in two ways. With the excitation spot held constant, the grating was rotated, resulting in a measurement of the edge emission spectrum. The spectral response of the system was calibrated using an Ocean Optics thermal source. With the grating held at a fixed wavelength, the excitation spot was translated away from the facet, resulting in a spectrally resolved SES measurement of the waveguide loss. When the spectrometer was set to the peak emission wavelength, and when the slit widths were doubled to accept a larger bandwidth, the measured loss values were consistent with loss values measured using the low-magnification setup. Further, these SES loss measurements were in good agreement with streak measurements. For these two reasons it is believed system loss has been sufficiently avoided.

It is necessary to block radiation modes from entering the collection optics. Surface emission can be easily blocked using a knife edge positioned on the top surface near the facet. However, some radiation modes propagating within the lower cladding will emerge from the facet. In fact, some radiation modes, traveling at shallow angles within the lower cladding will propagate with very little loss. In [98], angularly filtered SES measurements show that contributions from radiation modes can be significant. There, Si-nc films deposited on silica are studied. The bottom cladding is necessarily relatively thick. Radiation modes within the lower cladding propagate only at downward angles since there is no strong reflector to generate a standing wave. In contrast,

in this thesis the bottom SiO_2 cladding was 2.4-3 μm thick, and was grown on an opaque Si substrate. In these devices, radiation modes will transmit through the facet at both upward and downward angles. Loss measurements there were made using the SES technique are in good agreement with those made using streak measurements. It appears, then, that although radiation modes may be present in the SES signal, the power in the guided mode is dominant.

As is shown in section 5.2, Si-nc PL emission degraded with exposure to pump light. Further, the absorption was found to increase with exposure to pump light, as shown in 5.6. Both properties may impact the SES technique. To reduce this effect, SES measurements were performed with as low a pump intensity as possible. During loss measurements, two scans were performed prior to data collection so that each excitation spot has been degraded to a relatively stable emission efficiency. Care was taken to ensure that pump exposure on each excitation spot was the same throughout a measurement. For each data point, exposure lasted approximately 3 seconds.

In this work, two pump sources were used. Most measurements were made using a 405 nm diode laser. The laser, modulated with a function generator, can achieve powers as high as 50 mW continuous wave. In the SES setup with edge emission collected through the monochromator, typically only 10.8 mW was used, although the laser was modulated with a 50% duty cycle resulting in an average power of 5.4 mW. In the low-magnification SES setup, typically only 1 mW peak power was used. In both setups, the laser was focused onto the sample.

The laser spatial mode was measured to be singly peaked in its TE direction, but was multi-peaked in its TM direction. To quantify the pump intensity, the "scanning knife edge" technique was used, described in [140]. There, a knife was alternately scanned across the TE and TM directions of the beam while monitoring the partially blocked power. The width of the beam that contains 80% of the power (from 10%-90%) is quoted as the clip width. An effective intensity of the beam is calculated as the total power divided by the clip area. For most SES measurements, effective beam clip widths of the focused spot were 350 204 μm^2, resulting in an effective peak pump intensity of 7.6 W/cm^2 +/- 25%.

In addition to a pump laser, an LED pump source was used. The LED was a Nichia NSPB500S, specified to emit light in a spectrum peaked at 470 nm, with a spectral FWHM of 30 nm. The far-field beam from the LED is specified to have a FWHM of 14°. The LED was biased with 100 mA at a 50% duty cycle, resulting in a peak power of 15.8 mW.

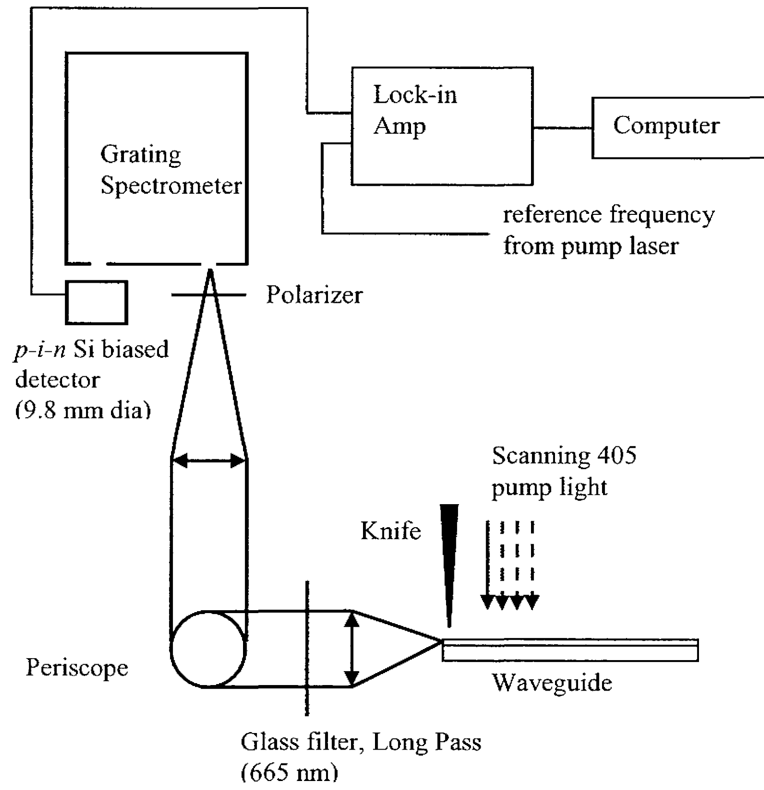

Figure 24: Schematic of the SES experimental setup.

Chapter 5. Results and discussions on Si-nc devices

5.1 Surface Emission

Surface emission spectra were collected from Si-nc films deposited on bare Si, as well as on SiO_2 or SiN_x/SiO_2 systems. As is discussed in section 4.1, surface emission is modified by the cavity function, *F*. Even emission from single layer Si-nc/Si films is impacted.

Recall that Table 6 on page 78 describes the structure and processing history of each device.

The interference phenomenon is considered *theoretically* for the case of a Si-nc layer of index 1.6 deposited on bare Si. Since most researchers in this field use films with n~1.6, in thicknesses ranging from 100-1000 nm, there is some value in showing the theoretically predicted modulation. In Figure 25 it is shown that for thin films <500 nm, the intrinsic emission from the considered Si-nc film will only be slightly distorted, and the peak will shift by ~10 nm compared to that expected from bulk material. For thicker films, the modulation increases in severity.

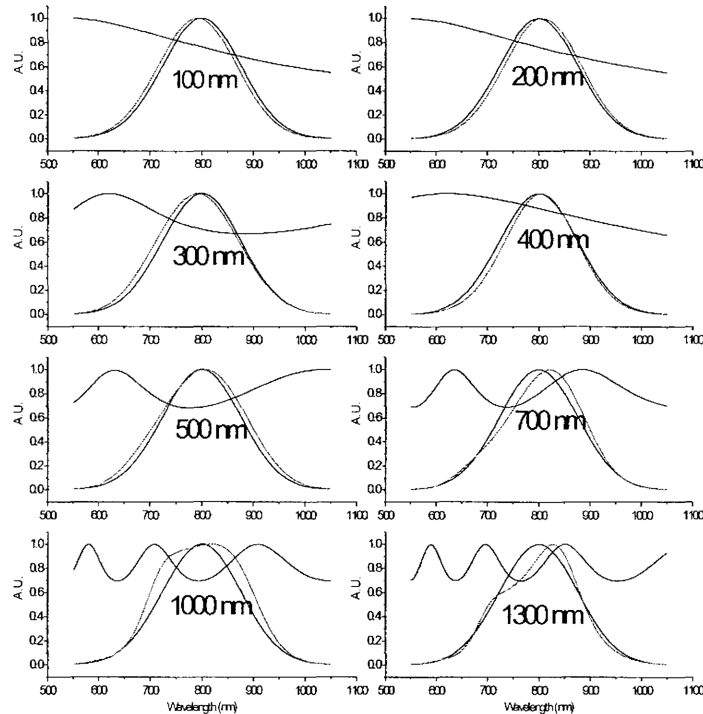

Figure 25:Theoretical modification of surface emission of an emitting material, collected at normal incidence. Here, emission is modeled to intrinsically emit a Gaussian spectrum, centred at 800 nm with a FWHM of 150 nm. The film material is modeled with a refractive index of 1.6, and the substrate is modeled as Si. The above graphs show theoretical spectra from 8 different film thickness. Each plot shows the intrinsic Gaussian emission spectrum (dark) as well as the theoretically modified surface emission that would actually be observed (light). Also shown is the modulation function, *F*. For these simulations, emission is assumed to occur uniformly throughout the film, even though the pumping intensity will actually be periodic.

Figure 26 shows an example of surface emission from a single layer Si-nc film, deposited on a Si substrate. The modulation effect from the cavity (of the single layer film) has a small impact. In this example, the emission is peaked at 793 nm with a FWHM width of 154 nm. The spectrum is close to symmetric, and its shape is well approximated as Gaussian.

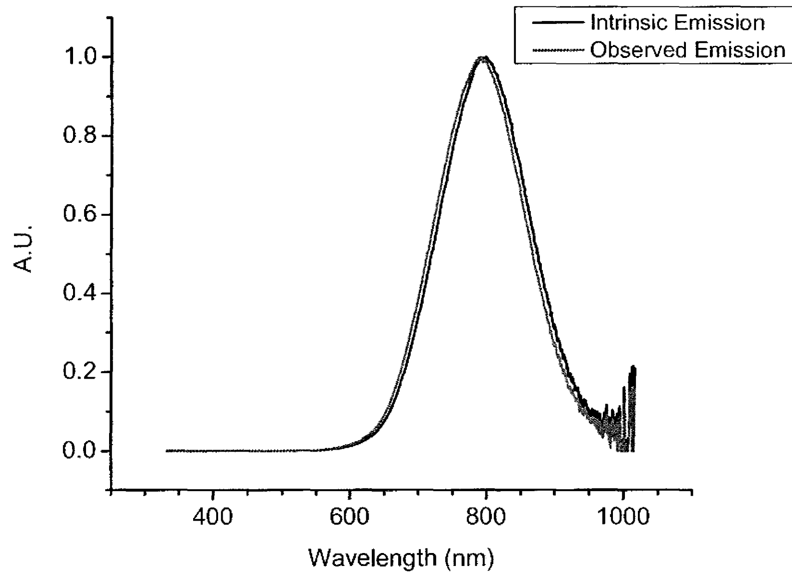

Figure 26: Surface emission spectra from a single layer Si-nc film. The film (053x3), has an index of 1.6, thickness of 98 nm, and has been annealed for 2hrs at 1100 °C in N_2+5%H_2. The observed emission spectrum, as well as the calculated "intrinsic" spectrum, are shown.

The emission efficiency improved after annealing in the presence of 5% H_2 (with either 95% N_2 or Ar_2) in support of the literature reviewed in section 2.2.2. No difference in the PL was observed between samples annealed in N_2 or Ar_2 atmospheres. Figure 27 shows PL emission from two multi-layered samples from the same deposition, but having undergone three different annealing recipes. Note that two curves are from the same sample, while the third is from a second sample from the same deposition.

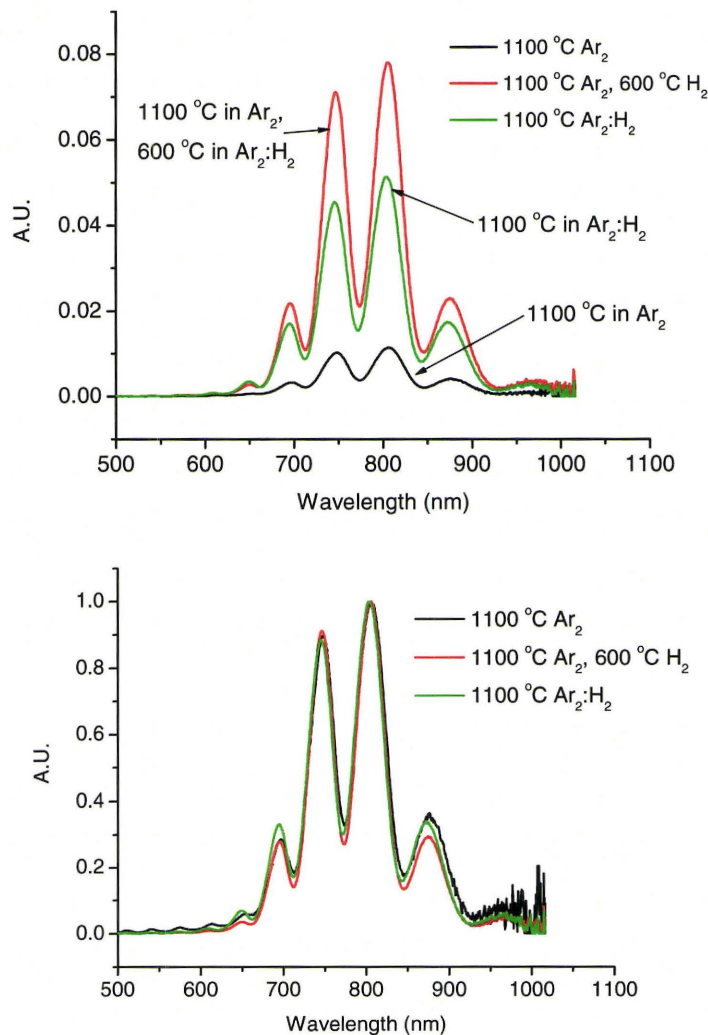

Figure 27: Surface PL of multi-layer Si-nc films under different annealing conditions. Top graph shows relative PL emission from two samples from the same deposition, measured after three different annealing recipes (034x1 and 034x2). All anneals were for a 2 hour duration. The sample having undergone the two-step annealing recipe was measured after each of the two steps. Bottom graph shows the same spectra, but normalized to the peak emission of each curve.

As can be seen, there is considerable modulation in the spectra. This will be discussed further below. Here, it is observed that the emission efficiency improves when the film is annealed in the presence of H_2. Integrating the spectra

of Figure 27 (Top) from 600 nm to 975 nm (above which the noise becomes excessive), reveals that, compared to the Ar_2 anneal, a 2nd low temp H_2 anneal improved the output PL by a factor of 6.2, while annealing once in Ar_2:H_2 (instead of Ar_2) improved the efficiency by a factor of 5.5. Further, Figure 27 (Bottom) reveals there was some shift in the spectral shape between annealing recipes. This has been studied more extensively by other researchers using films from the same chamber, deposited with similar compositions and annealing recipes [64]. Here, it is noted that the change in spectral shape was small and might possibly have been introduced through thickness/index variations across the sample, or furnace temperature differences between the two 1100 °C anneals.

There was a small amount of PL signal between 300 and 600 nm. From other experiments, its origin was found to be due to the SiN_x film. The signal was ~500 times weaker than the peak of the Si-nc emission at ~800 nm, and is not considered further.

To properly apply the Lukosz model [132] to the surface emission of the multi-layer films, the following procedure was taken. The "intrinsic" PL emission was measured by collecting PL from a Si-nc/Si sample, and then divided by the corresponding F of the single layer film. This Si-nc film is of the same refractive index and has undergone the same annealing recipe as the Si-nc film in the multi-layer waveguide. Alternatively, the intrinsic emission was collected from the edge emission from the waveguide, with the PL excitation spot close to the exit

facet. Next, *F* was calculated for the multi-layer S-nc/SiN_x/SiO_2/Si stack, and multiplied by the intrinsic emission.

For the model to accurately predict the peaks and valleys of the PL spectrum, the thickness and refractive indices of the films were required. The refractive index of the Si-nc and SiN_x films were characterized using variable angle, spectroscopic ellispometry performed at the University of Montreal, and analyzed at McMaster. Single layer films were deposited on bare Si. The dispersion curves are shown in Figure 28. The refractive index fits well using the Sellmeier equation, $n^2=1+B\lambda^2/(\lambda^2-C)$, with λ in nm. For an as-deposited SiN_x film, the fitting parameters for the range λ=(350-1000nm) are B=2.50153, C=15843. For an SiO_x film after annealing at 1100 °C for 2h in Ar_2+ H_2 5%, the fitting parameters for the range λ=(350-1000nm) are B= 1.55877, C= 23331.4. The estimated accuracy of index calculated with the ellipsometry model is +/- 0.02. Using fixed angle, fixed wavelength ellipsometry at 633nm, the thickness and index were found to not change within measurement uncertainty after annealing at 1100 °C for 2h in Ar_2 or Ar_2+ H_2 5%. The variation of film thickness across a given sample was 7%, with most of the non-uniformity occurring as a reduction of thickness a few mm from the edge of the sample.

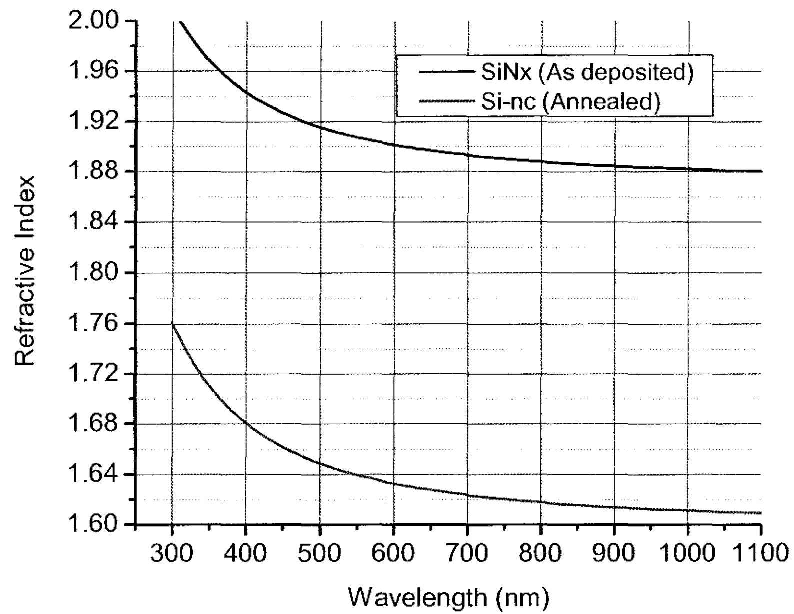

Figure 28: Refractive index of a Si-nc and aSiN$_x$ film as measured using spectroscopic ellispometry. The Si-nc film was annealed 1100 °C for 2h in Ar_2+ H_2 5%. The SiN$_x$ film was measured as deposited.

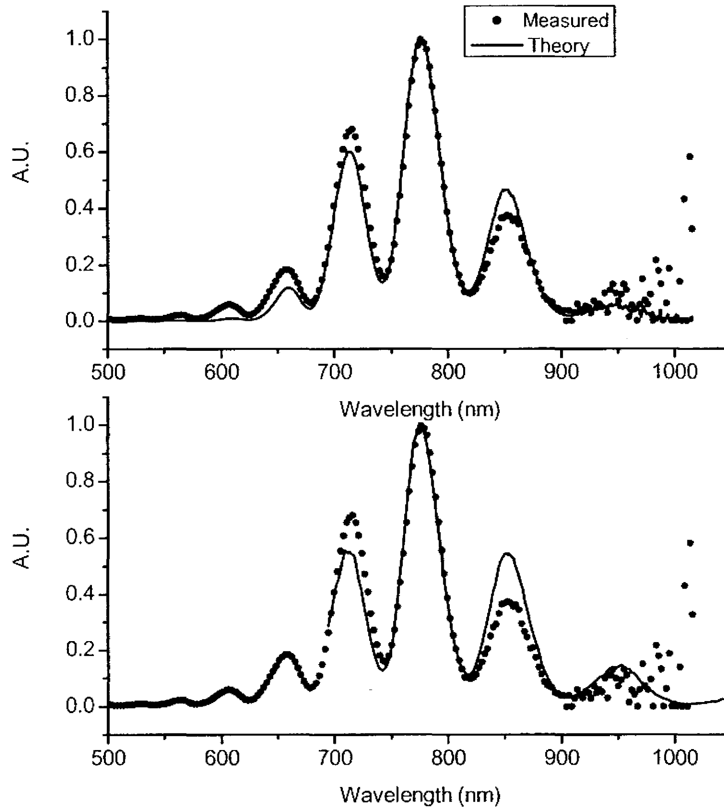

Figure 29: Fitted surface PL from air/Si-nc/SiN_x/SiO_2/Si sample 071x1. The measured values in both graphs are identical, but are fitted using different procedures. In the top graph, the intrinsic emission is obtained from a separate single layer Si-nc film, identically deposited and annealed to the Si-nc layer in 071x1. In the bottom, intrinsic emission is obtained from the edge emission of sample 071x1 using the SES setup, with PL excited ~200μm from the facet. In both graphs, the fitting function assumes target values for index and thickness whereas the thermal oxide thickness and *H* are used as fitting parameters. Here, the oxide thickness and *H* are set to 2.32 μm and 0.05 μm respectively. This value of *H* is half the Si-nc film thickness. The RMS difference between the two curves for the top graph is 0.04 (for data below 900 nm)

Figure 29 shows that the Lukosz model well-describes the data. The intrinsic emission can be taken either from a separate single layer sample, or from edge emission of PL excited close to the facet of the same device. Each method has a drawback. Using a separate sample introduces errors from variances between samples, from either the deposition itself or the post annealing. While

this error is eliminated by using edge emission from the same sample, edge emission is partially modified through absorption as it propagates the short distance from the point of excitation to the facet. As will be shown, absorption from the Si-nc layer is wavelength dependent. In this example, the modulation function is dominated by the thermal oxide cavity, and the quality of the fit is ~4 times more sensitive to relative change of the thickness (or index) of the thermal oxide film as compared to the properties of the two other films. Sensitivity tests show that spectroscopic ellipsometry provides sufficient accuracy of the films' indices and thicknesses to predict surface emission (with a quality of fit similar to the graph above). Although the wafer's thermal oxide is specified by the manufacturer to be 2.4 μm, spectroscopic ellipsometry revealed it is 2.34 μm thick, with a non-uniformity of ~20 nm. This is in good agreement with the fitting value used in Figure 29. The Lukosz model assumes uniform emission over the first H distance of the film thickness. As discussed in section 4.1, the optical pump light forms a standing wave pattern. Carrier tunneling to neighbouring Si-ncs is not expected to be large due to the oxide host. Pump light incident normal to the stack forms a standing wave with a period of $\lambda/2n=405/(2*1.68)=$ 120 nm, and a peak:valley ratio of 12.5 for the above structure. For the present study, H is taken as a fitting parameter, and the software code is not rewritten to reflect a non-uniform emission profile within the Si-nc layer. From sensitivity tests, F for the three layer film stack is relatively

sensitive to changes in H. For the Lukosz model to have predictive power of the fringe contrast, the non-uniform emission within the film needs to be accounted for. This may form the subject of future work related to the manufacturability of the current processes.

5.2 Fatigue of PL

The photoluminescence of Si-nc films was observed to decrease in time with increasing exposure to pump light. This characteristic, called fatigue, is reviewed in section 2.2.4. It is *possible* that fatigue was more severe in the limited samples studied in this thesis compared to samples from other groups where fatigue has not been reported. However, fatigue was also observed in the sample produced through ion implantation at Western University. This suggests fatigue may be a characteristic general to Si-nc films, albeit under-reported.

Fatigue limits the utility of the system, and can complicate standard measurements such as PL vs pumping power, SES, and VLS. In this section, fatigue is characterized in a limited parameter space for the purpose of highlighting the magnitude of the problem, documenting the pump intensity dependence, and to demonstrate the need for further study.

Two PL setups were used to characterize fatigue. The first was the HeCd PL arrangement, where an Ocean Optics CCD spectrometer provided a fast spectral readout in ~5 seconds (much faster than would have been possible with

the SES setup which used a monochromator). Using an excitation source at 325 nm from a 17 mW HeCd laser, with a *1/e* spot of 1mm, fatigue was observed in Si-nc films. The total integrated PL power decreased by ~9% over the first few minutes. In almost all samples tested, the spectral shape remained constant throughout the measurement.

Since the spectrum remained approximately unchanged during exposure to pump light, total PL emission measured directly with a *p-i-n* detector allowed quantitative characterization of PL fatigue with a much faster response time. For this reason the SES setup was used. The collection lens was optionally re-oriented to collect surface emission at ~45° from the surface normal instead of edge emission, since surface emission power was larger than edge emission power. As expected, edge emission and surface emission exhibited the same fatigue characteristics. Figure 30 shows a typical fatigue measurement of a Si-nc film. Care was taken to ensure that the measured PL area was not been exposed previously to pump light. The lock-in amplifier integration time was set to 30 ms, and data was acquired every 68 ms. It seems likely that the true peak signal at the start of the measurement, where the rate of change of PL is largest, was not fully resolved. The measured fall times from the peak value are therefore underestimates of their true values. The PL was seen to decrease with time, and exhibit a partial recovery when the beam is temporarily blocked. This property was observed in all deposited samples tested, and the sample produced through implantation, shown in Figure 31. When the deposited sample was left to recover

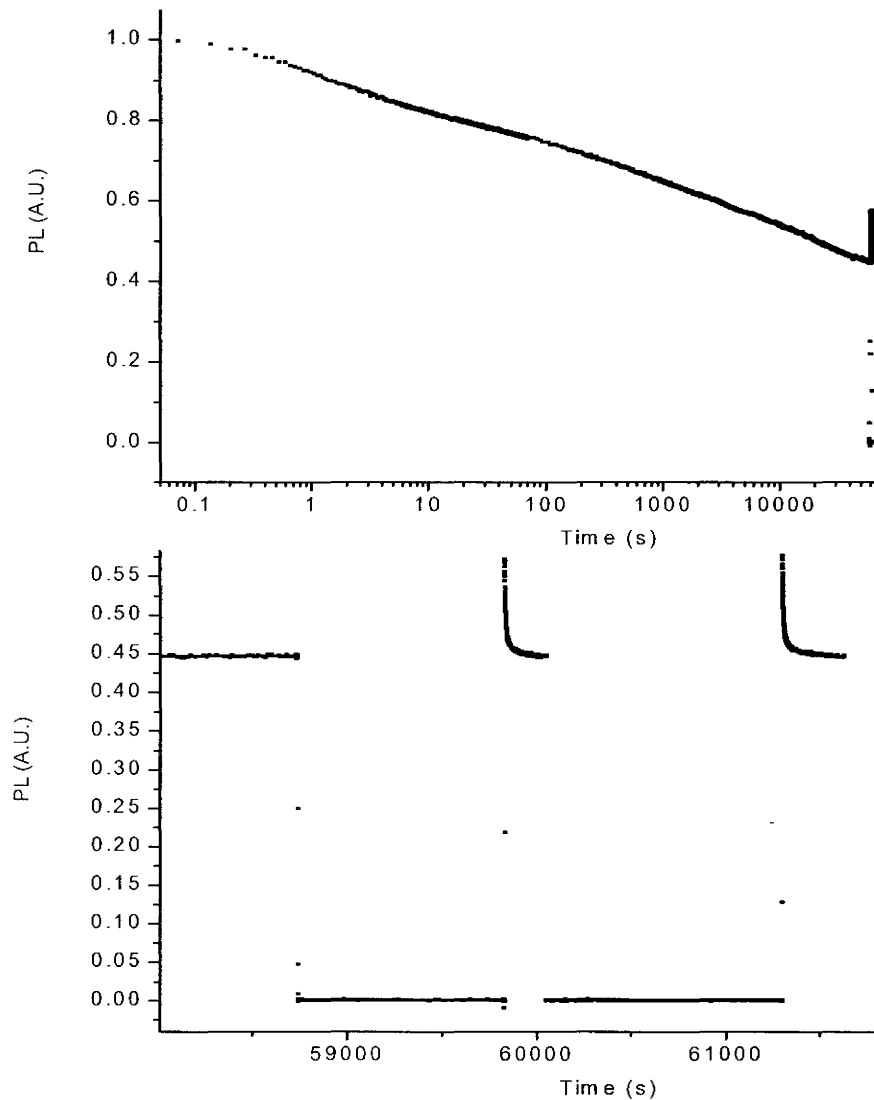

Figure 30: Fatigue measurement of the surface PL from sample 053x3 under 15 W/cm^2 of pump light. Top shows PL decay for the first 60,000 s (16.7 hrs). For clarity, the first few data points that show the initial rise from zero signal to full signal are not shown. The scale is normalized to the peak PL signal level, set to t=0. (Bottom) Enlargement shows the partial recovery of PL after the pump beam is momentarily blocked twice near the end of the acquisition. Note that the horizontal axis in the bottom plot is in linear time units whereas the top plot is logarithmic.

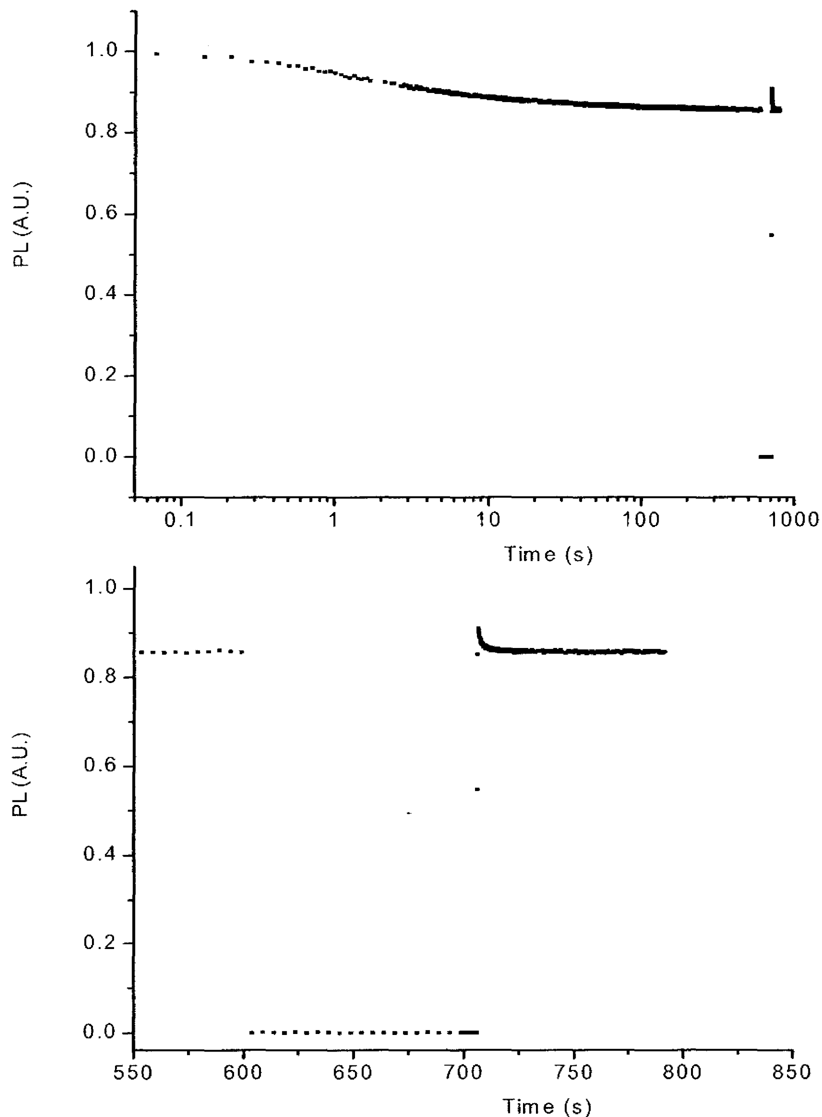

Figure 31: Fatigue measurement of the surface PL from the implanted sample while being pumped with 15 W/cm^2 of pump light. Top shows PL decay for the first 1000 s (16 min). Bottom enlargement shows partial recovery after the pump beam is momentarily blocked near the end of the acquisition. Note that the horizontal axis in the bottom plot is in linear time units whereas the top plot is logarithmic.

for a longer period, 18 hours, the recovery was only ~90% of the original emission power. This suggests that part of the fatigue is recoverable, and part is irrecoverable.

The amount of fatigue was found to be strongly related not only to the duration of pump light exposure, but also to the pump intensity, and may have been related to the dose. Fatigue curves wrere measured on three samples (053x3, 053x4, implanted) with three different pump intensities, and are shown in Figure 32. The beam was modulated with a 50% duty cycle, hence the quoted intensities are peak values (twice the average), and have an error of ± 25% [16]. Samples 053x3 and 053x4 were from identical depositions, with n=1.60, but annealed at 1100 °C in N_2:5%H_2 and N_2 respectively. Fatigue from the Si-nc film formed through ion implanted sample is also included. It is clear that the rate of fatigue increaseed with increasing pump intensity. The fatigue curves are not well fitted to a single exponential decay. A double exponential decay results in a better fit; however, the resulting two time constants are sensitive to the number of data points and data spacing considered in the fitting routine. In agreement with [75], the fatigue curves fit well (with an $R^2>0.99$) to the form

$$P = \frac{A}{(t+\tau)^B} \quad \textbf{(23)}$$

for all nine curves, except for the high intensity pumped curves for the implanted and 053x4 sample, where $R^2<0.95$. Here, A, B, τ are fitting constants, P is PL

[16] The largest source of error on the intensity measurements is introduced through lens alignment. Based on multiple measurements, this error is 25%

power, and t is time in seconds. Note that the fits cover over 4 orders of magnitude in the time scale.

Table 7 shows the time duration to reach 95%, 90% and 85% of the starting signal[17], and

Table 8 shows the fitted values of the nine curves to equation (23). The RMS difference between the data and the fitted functions is <0.006 for all but the 053x4 sample under maximum pump intensity, where the difference is 0.02. For comparison, in [75] Si-nanocrystals formed from P-Si are reported to have a B of 0.3, and a τ of 111 ms under an excitation power density >1.8 kW/cm^2. A partial recovery of PL when the pump light is blocked is also observed in this reference.

Sample 053x3, which was annealed in the presence of H_2, showed a faster fatigue than the other two samples, which were annealed in N_2 at the same temperature and for the same length of time. This suggests that while H_2 increases PL efficiency, the sample fatigues more quickly. The implanted sample showed less fatigue than samples produced through deposition, but degraded nonetheless. The implanted sample was included in this study to show that fatigue is not unique to Si-nc films prepared by ECR-PECVD at McMaster, and may be a property more general to Si-ncs embedded in SiO_2. The result is rather

[17] Since it is not clear that equation (23) is the correct equation that describes the underlying physical process of fatigue, fall times are also quoted.

discouraging since the power law decay implies signal will, eventually, diminish to zero.

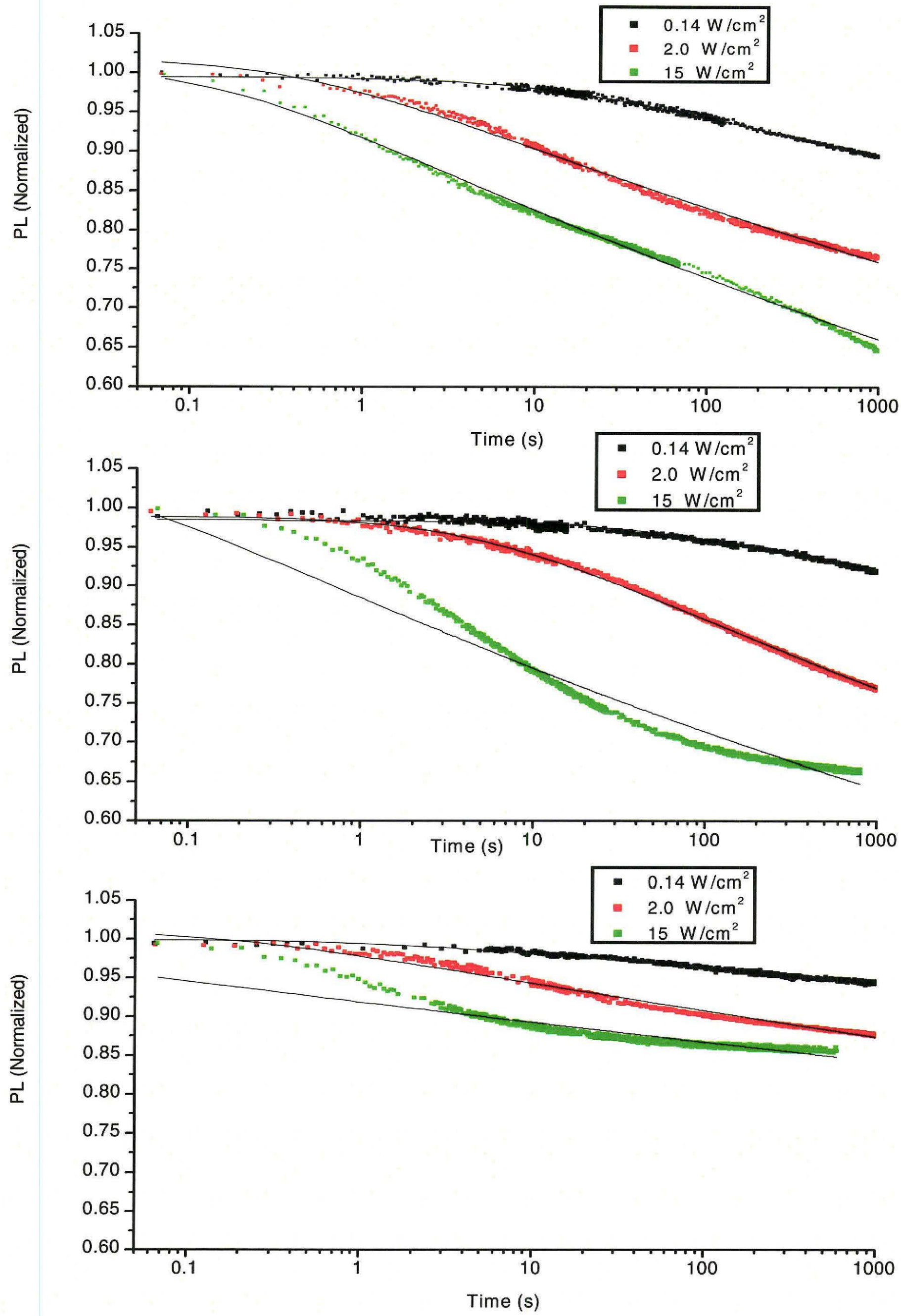

Figure 32: Fatigue measurements on three samples, with three different pump intensities. Top is from sample 053x3 (N_2:H_2 annealed), middle is from sample 053x4 (N_2 annealed), bottom is from the implanted sample. The symbols are measured values, and the lines are the curve fits using equation (23).

Table 7: Fall times, in seconds, for the PL signal from Figure 32 to fall to 95% and 90% of the starting value. Based on noise in the measurement, the fall times have a relative error of 20 % in the worst case. NA indicates acquired data did not reach the 90% threshold.

Sample	0.15 W/cm^2		2.0 W/cm^2		15 W/cm^2	
	95%	90%	95%	90%	95%	90%
053x3	73	840	3.0	12	0.5	1.4
053x4	180	NA	6.8	36	0.6	1.7
Implant	412	NA	7.6	110	.9	5.1

Table 8: Fitting parameters for the PL signal from Figure 32.

Sample	0.15 W/cm^2			2.0 W/cm^2			15 W/cm^2		
	A	τ (ms)	B	A	τ (ms)	B	A	τ (ms)	B
053x3	1.06	12.6	0.0242	0.998	.455	0.0381	.924	.166	0.0486
053x4	1.08	52.5	0.0235	1.07	5.22	0.0478	.886	0.0280	0.0470
Implant	1.00	1.15	0.00813	0.980	0.149	0.0166	0.919	0.0010	0.0125

Fatigue was also characterized for samples having undergone different annealing temperatures. Figure 33 shows fatigue measurements made on samples from deposition 014 after annealing at three different temperatures, 900, 1000, 1100 °C for 2h in Ar_2: 5% H_2. All three samples showed fatigue, although the amount of fatigue was less in the 900 °C anneal. Integrated surface PL showed that the PL signal levels ratios were 1:4.9:22 for the three temperatures 900, 1000, 1100 °C respectively. While a lower temperature 900 °C anneal resulted in less fatigue than the two higher annealing temperatures, the overall signal was much lower.

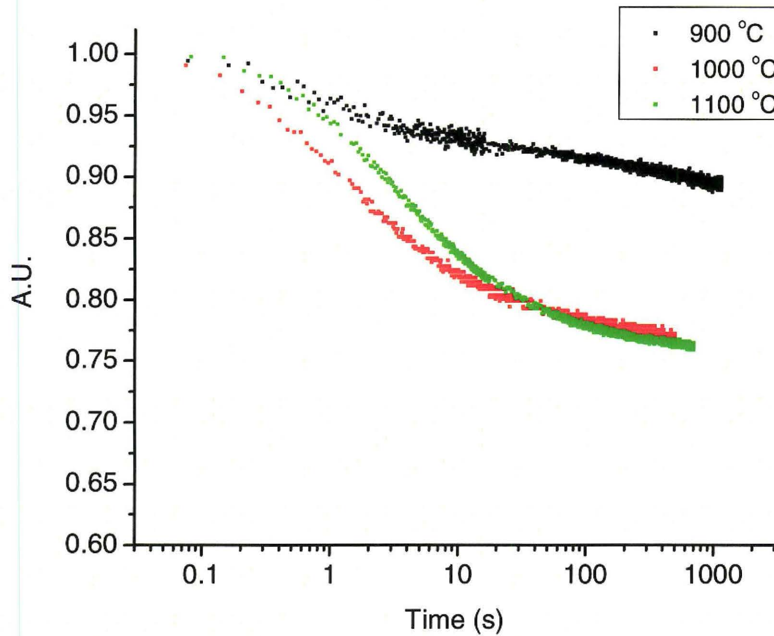

Figure 33: Fatigue measurements on sample 014, annealed for 2 hrs in Ar_2: 5% H_2 at three different temperatures. The pump intensity is 15 W/cm^2.

5.3 Emission Efficiency

Figure 34 shows the total output *PL vs pump intensity* for a typical Si-nc film. Surface emission was collected directly with a detector, without spectral correction. Based on other measurements, the PL spectra blue-shifted slightly with increasing pump intensity, although the shift is small compared to the emission width. Because of fatigue, there is expected to be considerable hysteresis in the curve. Prior to taking the measurement, the spot was exposed to the maximum available pump intensity for 20 minutes, then PL signal was quickly measured with various pump powers. The 20 minute pre-exposure attempts to keep each data point at the same level of fatigue/recovery. Sufficient time was

allowed for the laser's temperature controller to stabilize (~20 s) between measurements. It is seen that the PL *power vs. pump* intensity is sub-linear, showing that efficiency decreases with increasing pump intensity. Such curves have been observed by others in Si-nc films prepared by deposition [141] and implantation [142]. The sub-linear shape is commonly attributed to a saturating effect from Auger recombination that limits free carrier density within a nanocrystal [143].

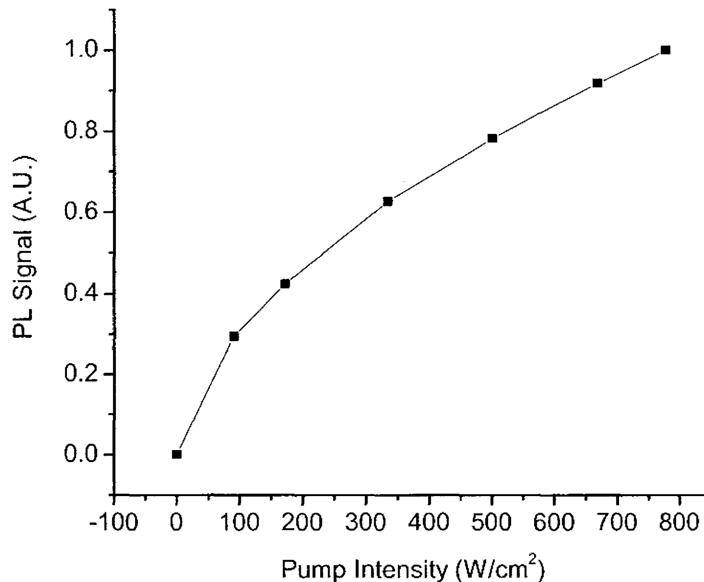

Figure 34: PL signal with different pump laser peak intensities, taken on sample 015x6, annealed at 1100 °C in Ar_2: 5% H_2 for 2 hrs.

The PL emission efficiency of Si-nc films was measured using the technique described in section 4.2. The efficiency was measured for three different pump intensities on a 543 nm thick Si-nc film, deposited on a quartz

substrate, and annealed for 2hrs at 1100 °C in Ar_2: 5%H_2. The results are shown in the table below.

Pump Intensity (W/cm^2)	η_{int}
0.0208	0.15
0.186	0.14
2.24	0.10

Table 9: Internal quantum efficiencies of sample 031x1 measured at different pump intensities. The uncertainty in the pump intensity and efficiency is +/-25% and +/-30% respectively.

A second sample from a different deposition with a 300 nm Si-nc film, 030x1, was also measured and gave similar results within experimental error. Based on these measurements, the absorption coefficient of 405 nm light in the Si-nc layer is 2,380 cm^{-1} ±30%. For comparison, the absorption coefficient of bulk Si at this wavelength is known to be 75,608 cm^{-1} [144].

The η_{int} of the Si-nc films is seen to be near 0.14 +/- 30 % for pump intensities below ~0.19 W/cm^2 (This corresponds to an η_{ext} of 0.031 if light emitted from both surfaces of the substrate is included). Note that this film has undergone high temperature annealing in Ar: 5% H_2, and that the emission area was not "fatigued" prior to measurement. At a higher pump intensity of 2.2 W/cm^2, the efficiency is almost 50% lower. This reduction is likely due to both the fatiguing and saturating effects discussed in the previous section. For comparison, in reference [145], an η_{ext} of 0.045 is reported for Si-nc films

prepared by RF sputtering. There, the films have an index of 1.7, silicon content of 38%, and are annealed for 1 hour at 1150 °C (the gas species present in the furnace during annealing is not reported).

In this thesis, the PL efficiency of the Si-nc film *as a whole* is of interest, since that is the quantity that pertains to device performance. Some researchers are more interested in measuring the efficiency of only those Si-ncs that emit light. In a simple description, there will be a large subset of of Si-ncs within the film that will not emit light very efficiently, either due to impurities or surface defects. The entire PL emission from the film is thought to result from the few Si-ncs that are defect and impurity free. For this reason, references [146] and [147], aim at measuring the PL quantum efficiency of Si-ncs embedded in SiO_2 through analysis of the PL lifetime of films placed in controlled proximity to a strong reflector.

5.4 Si-nc core slab waveguides

The prism coupling setup revealed many interesting properties of the air/Si-nc/SiO_2 waveguides[18]. The presence of a streak and an m-line at the expected coupling angle indicated that modes were indeed present. Further, the prism coupled light maintained its polarization as it propagated along the

[18] All waveguides in this thesis are on Si substrates, hence the structure should properly be written as air/Si-nc/SiO_2:Si. Since the Si substrate is not involved with guiding, it is omitted.

waveguide. There does not appear to be strong coupling between the TE and TM polarized modes as might be introduced through scattering in the waveguide or in transmission through a non-perfect facet[19]. This was measured quantitatively on sample 016x3, which is a 500 nm thick Si-nc film deposited on 3 μm of thermal SiO_2, annealed in the two-step process. After propagating 5 mm from the coupling spot and exiting the facet, 850 nm prism coupled light was measured to maintain its polarization to a ratio >308:1 for both the TE and TM polarizations. Similar polarization preserving propagation properties were also observed in nitride waveguides with integrated Si-ncs. This property is an important assumption in the SES measurement technique.

The loss of the Si-nc core waveguide was measured at four wavelengths using the streak method. Four different diode lasers were used to obtain results at these different wavelengths. SES measurements were also made on the same sample. The loss values are shown in Figure 36 and Table 10. Examples of streak and SES measurements used to obtain four of these data points are shown in Figure 35.

[19] Transmission through a perfectly smooth, planar surface preserves the polarization of light. A surface with non-zero roughness may randomize the polarization (and direction) to some degree.

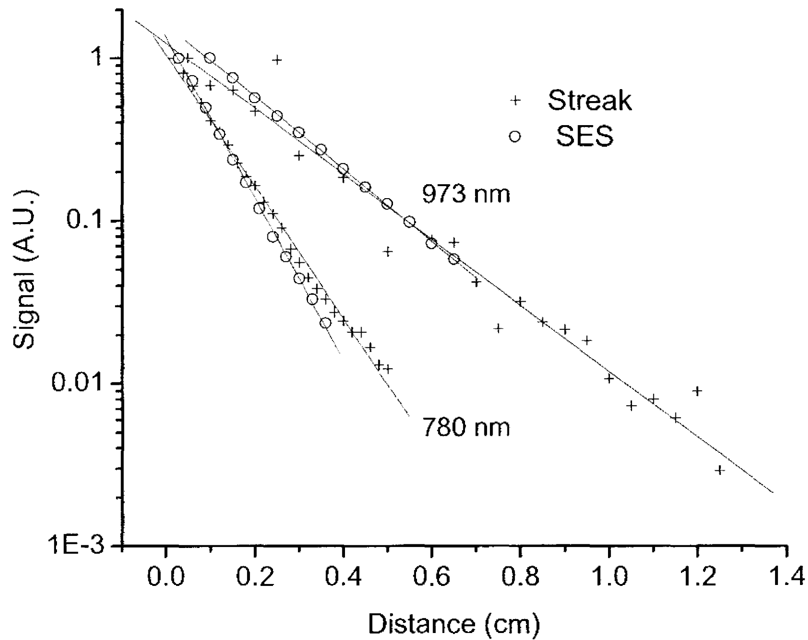

Figure 35: Example of streak and SES measurements of the TE loss on sample 016x3 at two wavelengths. Streak measurements were obtained using the prism coupler with an alternate set of four different diode lasers. SES measurements were obtained by directing the edge emission through a monochromator held at a fixed wavelength. The shown lines are the linear regression fits.

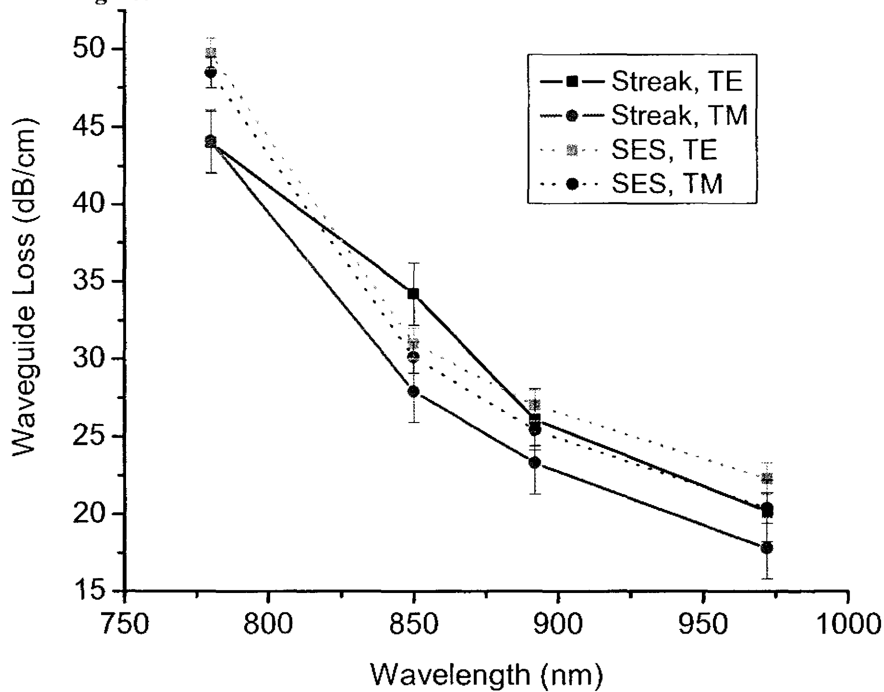

Figure 36: Waveguide loss measurements v.s. wavelength of the Si-nc core waveguide, 016x3.

Wavelength (nm)	Waveguide Loss (+/- 2 dB/cm)		TE/TM Meas. (+/-0.2)	TE/TM Theory	Material Loss (+/- 3 dB/cm)
	TE	TM			
780	44	44.1	1.0	1.1	49
850	34.2	27.9	1.2	1.1	36
892	26.1	23.3	1.1	1.2	29
972	20.2	17.8	1.1	1.2	23

Table 10: Waveguide loss measurements of a Si-nc core waveguide, 016x3, at different wavelengths using the streak method. The data corresponds to that of the above figure. Measured and theoretical ratios of the waveguide loss of the two polarizations are shown in columns 4 and 5.

In the above graph, the streak measurements are estimated to have an error of +/-2 dB/cm, whereas the SES measurements have an error of +/- 1 dB/cm. These errors take into account the reproducibility of the measurement across the sample, and error in the regression used to obtain each data point. Comparing the two techniques, the streak measurements contain more noise, but are more accurate, whereas the SES measurements contain less noise, but the scale is prone to calibration issues.

If it is assumed that the Si-nc film introduces a polarization independent loss throughout the bulk of the film, then modal analysis coupled with equation (7) can be used to calculate the *material loss* [20]of the Si-nc film. This is shown in the last column of Table 10. The two polarizations should result in an identical

[20] Waveguide loss is the total loss of the waveguide, whereas *material loss* has been defined as the loss due to material absorption and scattering within the bulk of a film. A waveguide will also have scattering loss introduced through surface roughness.

material loss, hence the average is shown. Here, it is assumed that all waveguide loss is due to material absorption and scattering, and ignores scattering from interface roughness. For clarity, it is henceforth understood that the calculation of material loss makes these three assumptions (polarization independence, uniformity, neglecting interface roughness). The loss of the Si-nc material can be easily converted to a Si-nc absorption cross-section,

$$\sigma_{Si-nc} = \frac{\alpha_{Si-nc}}{\rho} \quad \textbf{(24)}$$

where ρ is the Si-nc density, calculated in section 3.3.2 to be $2*10^{19}$ cm^{-3}. For example, at 850 nm an absorption cross section of $4.1*10^{-19}$ cm^2 is calculated. .

Table 10 also shows that the measured ratio of the waveguide loss of the TE/TM polarizations is close to what is theoretically predicted under these assumptions. This is essentially a test of the validity of the loss description given by equation (7).

From Figure 36, the SES measurements are seen to fall within 3.2 dB of the streak measurements for all but the shortest wavelength where the difference is within 6 dB. It is possible that the system loss of the SES setup was wavelength dependent. Such an artifact could be introduced by a misaligned input. Alternatively, when the modal loss is high, the edge emission may have more significant contributions from radiation modes that experience an even higher loss.

Based on the streak measurements, there was a large wavelength dependent waveguide loss of -0.14+/- 0.03 dB/(cm*nm). Across the FWHM of the Si-nc emission band, the loss changes ~42%. The origin of material loss, and its wavelength dependence, is assumed to arise both from material absorption within the Si-ncs, as well as scattering within the bulk of the film. In section 5.7, experiments are suggested to differentiate between these two sources of loss. Other researchers have calculated the scattering loss from the inhomogeneous refractive index of Si-nc films to be much smaller than the total observed loss, as will be reviewed near the end of this section.

Edge emission spectra from sample 016x3 are shown Figure 37. The polarization resolved spectra show no structure within the resolution of the instrument (5 nm), and the spectrum is seen to distort when the excitation spot is placed further from the facet. The distortion can largely be described as a red-shift of the spectral peak. The red-shifting continues as the excitation spot is moved further and further from the facet. This is consistent with the earlier streak measurements which show a wavelength dependent loss. The distortion of the spectrum is therefore of the form $e^{b\lambda z}$, where b is a positive constant, and z is the propagation distance. The edge emission spectra are seen to be very similar to the surface emission of similarly prepared single layer Si-nc films (which are not complicated by interference effects). Recall from section 5.1 that edge emission collected from an excitation spot located close to the facet may be successfully

used as the "intrinsic" emission in the interference model for surface emission. This strongly supports the model presented in Chapter 3 for an integrated emitter.

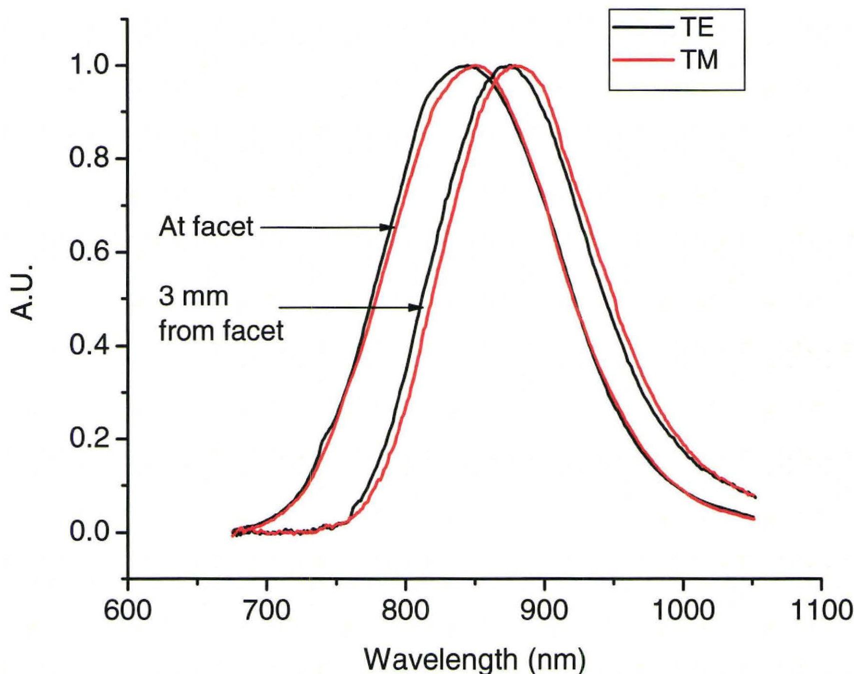

Figure 37 Edge emission spectra of sample an air/Si-nc/SiO_2 waveguide, 016x3. Emission is measured with the excitation spot in two places, at the facet (0.3 mm) and 3 mm from the facet.

The repeatability of loss values in Si-nc films with the fabrication process is untested. During this work, Si-nc core waveguide structures were deposited at the beginning and end of the project, for the purpose of measuring the reproducibility of Si-nc film loss. The sample presented above was deposited at the beginning of the project. A second sample, with the same (target) refractive index as 016x3 but deposited 13 months later and (annealed with the same recipe) is measured to have a loss value ~15 dB/cm higher that that of 016x3 at each wavelength (as measured using the SES method). The loss in this sample is too

high to perform streak measurements. The source of these changes is theorized to have resulted from changes in the properties of the deposition, as the annealing steps are relatively simple and easily controlled. In the duration spanning the two depositions, scheduled (and unscheduled) repairs to the deposition chamber were performed, such as the introduction of new pumping equipment, new mass flow controllers, and a replaced thermocouple. While the changes were minor and not expected to impact the deposition properties, it appears the calibration of the chamber may have drifted. During this time interval, single layer depositions were performed and the gas flow rates recalibrated against the resulting refractive index. However, RBS, XRD, and TEM have not been performed on more recent calibration samples. The PL properties of the calibration samples spanning the project are comparable, both in signal strength and in spectral shape, however, it appears that this may not be a reliable predictor of material loss. Further, during the deposition of films for the two-sectioned devices, the sample temperature during deposition was lowered from 120 °C to 100 °C to avoid overheating the photoresist. Such a change may have decreased the film density. For these reasons, the quantitative loss measurements presented in this section cannot be applied with great confidence to other devices without further test samples. (In contrast, the SiN_x films exhibited low loss in samples spanning the entire duration of the project).

Despite the variation in Si-nc material loss, the results in this section clearly show waveguide behaviour in support of the propagation description given

in section 3.1.3. Waveguide loss appears to arise from the Si-nc film, and the edge spectra shape corresponds to the "intrinsic" Si-nc emission distorted by a wavelength dependent loss.

This is an important observation as there has been debate recently on observed "spectral filtering" of SES edge emission in Si-nc core slab waveguides fabricated on silica substrates. It is unclear whether edge emission on air/Si-nc/silica slab waveguides is dominated by a propagating mode, or from radiation modes propagating in the substrate. For example, reference [98] shows the difficulties in differentiating between guided and unguided edge emission in Si-nc core waveguides fabricated on silica samples. Radiation modes propagating in the cladding do so with considerably less loss than the fundamental mode (since they propagate entirely in the transparent silica), hence edge emission may be dominated by radiation modes as opposed to guided modes. Some of these modes propagate at grazing angles to the film boundaries and will escape the facet to be detected on top of the guided mode signal. In some waveguide designs, the light from these radiation modes may contain considerable spectral structure, giving rise to "spectral filtering" of the edge emission. The polarization dependence, and collection angle dependence of spectral filtering has been calculated [98, 148]. Other reports [99, 152] argue that spectral filtering can be described entirely by considering guided mode propagation and birefringence of the Si-nc film. It must be noted that the vast majority of reports of spectral filtering are observed on waveguides on silica substrates. The samples in this thesis use a 2.4-3 μm thick

bottom SiO_2 cladding, thermally grown on Si. The Si substrate introduces a source of loss for radiation modes propagating in the lower cladding.

Propagation losses of Si-nc core waveguides have been reported in the literature and the results vary drastically, ranging from ~10 dB/cm to ~176 dB/cm. Results presented in this thesis fall in the middle of that range. Variations are expected to arise from actual differences in the optical absorption in differently prepared Si-nc films, differences in modal overlap within the waveguide, losses introduced through surface roughness, and possibly to measurement interpretation.

In [149] and [97], a waveguide loss of 77 dB/cm is measured in air/SiO_2/Si-nc/silica slab waveguides made through deposition of SiO_x using PECVD, followed by high temperature annealing at 1250 °C for 1 hour. The reports use the SES method, with the edge emission presumably coupled to a monochromator set to 750 nm. The Si-nc film has an index of 2.0, and the authors report a confinement factor of the mode with the Si-nc layer of 0.83. The authors do not mention polarization, though it appears they quote values for the TE mode. Using the dimensions of their reported waveguide, the confinement factors are calculated here as 0.82 and 0.60 for the TE and TM polarizations respectively, and the ratio of the waveguide loss for the TE/TM polarizations is calculated theoretically to be 1.3. It is not clear if the authors have neglected to account for differences in polarization, or if they have neglected to mention the

presence of a TE aligned polarizer within their collection optics. Assuming the latter, their waveguide loss corresponds to a material loss of 85 dB/cm at 750 nm.

In [150], absorption losses of two Si-nc waveguides are reported. The Si-nc film is fabricated through reactive magnetron sputtering followed by annealing. Samples with refractive indices of 1.776 and 1.565 are reported to have material losses of 70+/-5 and 57+/-4 dB/cm respectively at 830 nm. The loss measurements are made on a ridge waveguide by theoretically calculating the coupling efficiency of probe light into and out of their chip. In the lower index sample, a wavelength dependence loss is reported. From their data, the loss spectrum appears to be linear in the visible region, with a slope of -0.4 dB/(cm*nm). Based on TEM measurements of the Si-nc size and density, the estimated loss from scattering is calculated to be <0.5 dB/cm. Based on surface AFM measurements, the loss due to roughness is calculated to be <3 dB/cm.

In [151], photo-thermal deflection spectroscopy is used to measure the material absorption of Si-nc films produced through ion implantation and annealing. While the technique does not easily provide a calibrated loss scale, it is insensitive to scattering, and the presented results show that material absorption of the Si-nc layer is smooth over the visible range, and decreases monotonically with increasing wavelength.

In [152] Khriachtechev et al. report much smaller losses. The authors use the SES method on waveguides with Si-nc cores deposited on silica substrates. The index of the Si-nc film is 1.67, and they report a waveguide loss of ~10.8

dB/cm at 780 nm. A small wavelength dependence in the loss is observed across the emission band, decreasing with increasing wavelength. However, the observed edge emission spectra has significant structure, interpreted by some to be the result of propagation through radiation modes, as discussed in section 4.3. It is only appropriate to assign waveguide and material losses for modal propagation.

In [153] a waveguide loss of 176 dB/cm is reported at 730 nm. The slab waveguides are formed from Si-nc films deposited using magnetron sputtering of an amorphous Si/SiO_2 superlattice on top of a thick SiO_2 cladding, followed by high temperature annealing. The refractive index, or Si-nc density is not reported. The reported loss is measured using the VSL method under continuous wave pumping. (Under pulsed excitation, the authors report gain of 215 dB/cm). Note that in this reference, the optical loss associated with Si-nc is measured under optical excitation.

In [102], a waveguide loss of 11 dB/cm is reported in Si-nc core ridge waveguides. The losses are measured using the streak method at 633 nm and 780 nm. Very little difference is observed in the loss between the two wavelengths. The Si-nc layer is formed from multiple ion implantation of Si into SiO_2, followed by annealing at 1100 °C for 1 hour. The resulting refractive index of the layer is 1.61. Based on Si-nc size and density measurements, the scattering loss is theoretically calculated to be 2 dB/cm at 780 nm.

5.5 SiN_x core passive slab waveguides

Waveguide loss from air/SiN_x/SiO_2 waveguides were characterized using the streak method. Figure 38 shows the measured loss of a typical device at three different wavelengths. Devices from three other depositions showed similar results, indicating the fabrication process is reproducible. Table 11 summarizes the data, as well as the calculated ratio of the waveguide losses of the TE/TM polarizations, and the calculated material loss. The measured and calculated ratios of the waveguide loss for the TE/TM polarizations are in reasonable agreement, in support of the material loss description. However, since the loss values are low, the relative uncertainty is quite high and other loss mechanisms, such as scattering from interface roughness, may be present but unresolved. The material loss is seen to be ~3 dB/cm, with a small wavelength dependence. The origin of this loss is unconfirmed, but is likely due in part to both material absorption and bulk scattering. The data shown was acquired after the sample had undergone three annealing steps: 1100 °C in N_2 for 2 hours followed by two anneals at 400 °C for 2 hrs in N_2:H_2, and 600 °C for 2 hrs in N_2:H_2. Streak measurements at 850 nm after each annealing step shows the loss does not change significantly between anneals. The measured waveguide loss of an as-deposited sample (from the same deposition) reveals a loss of 2.9 and 2.3 dB/cm at 850 nm for the TE and TM polarizations respectively.

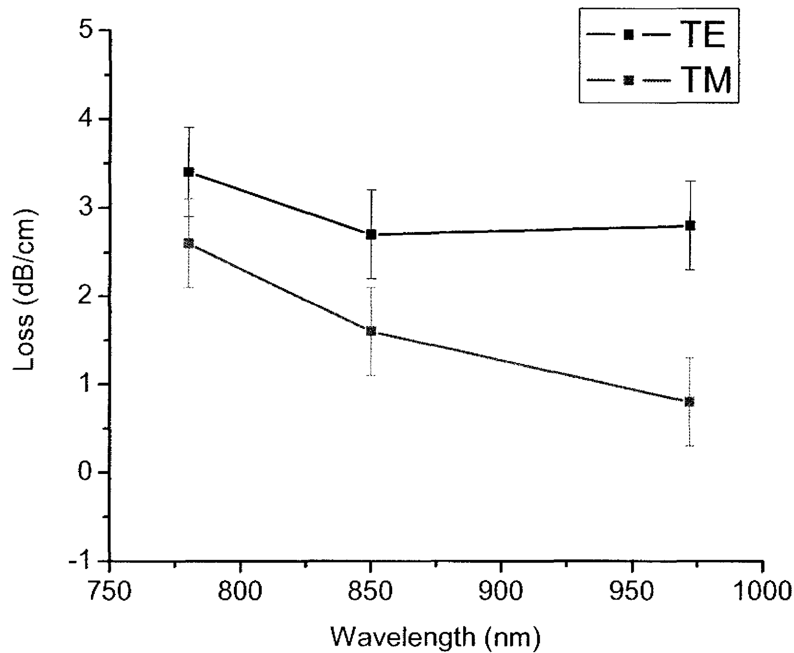

Figure 38: Loss measurements of an air/SiN_x/SiO_2 passive waveguide, made using the streak method. The sample, 051x2, has a 300 nm thick SiN_x core, and was annealed at 1100 °C in N_2 for 2 hours followed by two anneals at 400 °C for 2 hrs in N_2:H_2, and 600 °C for 2 hrs in N_2:H_2.

Wavelength (nm)	Waveguide Loss (+/- 0.5 dB/cm)		TE/TM Meas.	TE/TM Theory	Material Loss (+/- 1 dB/cm)
	TE	TM			
780	3.4	2.6	1.3±0.3	1.3	3.6
850	2.7	1.6	1.7±.06	1.4	2.7
972	2.8	0.8	3.5±2.3	1.6	2.3

Table 11: Loss measurements of a SiNx core waveguide. The data corresponds to the above graph.

Using the calculated material loss values, a small wavelength dependence of -0.006 +/- 110% dB/(cm*nm) is measured, noting that the error on this value is

quite large. The SiN_x material loss was not significantly affected by annealing in the presence of H_2 for (at least) 2 hours, provided the temperature was less than (at least) 600 °C. However, the material loss of SiN_x was seen to increase from 3 dB/cm, to 12 dB/cm after annealing at 1100 °C in N_2:H_2 for 2 hours. This is demonstrated in Figure 39, which shows streak measurements of the TE polarization waveguide loss for three co-deposited samples. One sample was measured in its as-deposited condition, and another sample (051x2) was measured after each of the following 2 hour annealing steps:

1. 1100 °C in N_2
2. 400 °C in N_2:H_2
3. 600 °C in N_2:H_2

The as-deposited and annealed samples all measureed waveguide loss near 3 dB/cm. A third sample, 051x3, was annealed at 1100 °C for 2 hrs in N_2:H_2, and measureed a waveguide loss of 12 dB/cm. For clarity, the slopes at 3 and 12 dB/cm are also shown.

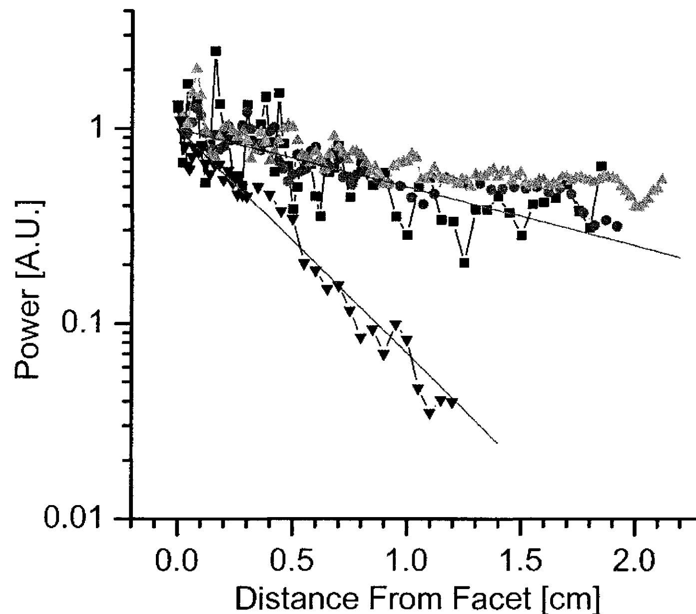

Figure 39: Streak measurements of three air/SiN_x/SiO_2 waveguides from the same deposition under different annealing conditions. Down pointing triangles show the measurement for the sample annealed at 1100 oC in N_2H_2. The other symbols show the streak measurement for samples annealed using steps 1, 2 or 3, as described in the text.

The impact of annealing at high temperature in the presence of H_2 appears to be partially recoverable through further annealing at high temperature in N_2 (ie, H_2 free). This is shown in Figure 40. Here, streak measurements are shown for the TE polarization at 850 nm for sample 051x3 after a first anneal in N_2:H_2, and a second anneal in N_2. Both anneals were performed at 1100 °C for 2 hours. A streak measurement for an as-deposited sample from the same deposition is also shown. The waveguide loss is seen to change from 2.9 dB/cm to 10.7 dB/cm after the first anneal, and then partially recovers to 3.6 dB/cm after the second H_2-free anneal.

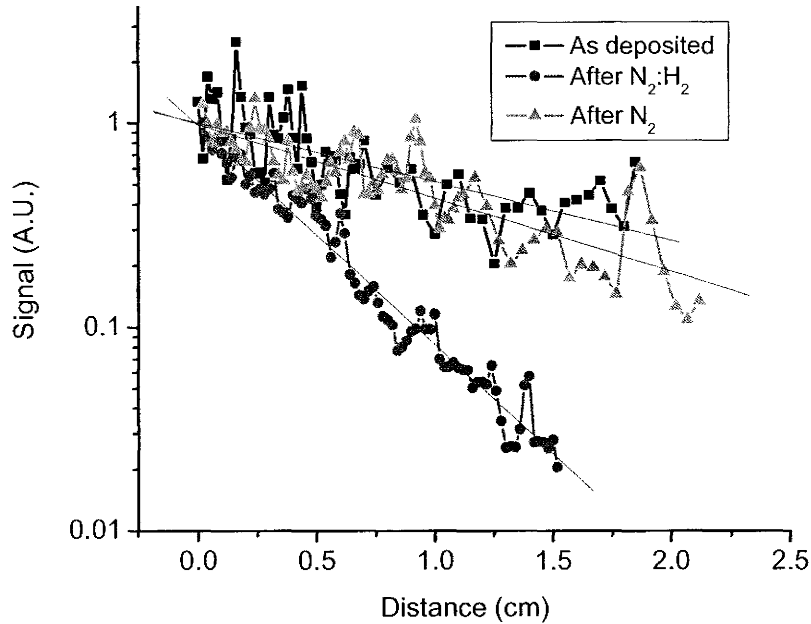

Figure 40: Streak measurements of a air/SiN_x/SiO_2 after high temperature annealing showing H adsorption followed by H desorption.

Hydrogen is known to increase the absorption of light near 3 μm and 1.5 μm in SiN_x and SiO_yN_x systems from overtones of N-H stretching modes. The presence of N-H bonds, and the associated loss, has been shown to be eliminated by desorption of H through annealing in ambient N_2 gas at high temperatures >1000 °C [154].

Hydrogen transport in SiN_x films deposited using plasma CVD has been studied by others, mainly to explore electronic device passivation in back-end processes. There, the films are treated as a source of H, introduced through the CVD process. As-deposited films made using plasma source silane, typically contain large quantities of H, ranging from 2-10 at %, and should more properly

be written as $SiN_x:H_y$. Annealing these films at temperatures higher than the deposition temperature causes H to diffuse within the film, and escape through the surfaces/interfaces. The transport of H[21] can result from slow diffusion of atomic H [155], or from fast diffusion of molecular H_2 (and/or NH_3) [156]. In molecular diffusion, the transport rate is limited by the rate of dissociation of H from the matrix and formation of the molecule. The diffusion of the molecule is too rapid to measure. While this desorption of H from $SiN_x:H_y$ films has received most attention, adsorption of H during film annealing in the presence of H_2 has also been observed [155]. Recently, it has been shown that slow atomic diffusion is the dominant transport process in high density films deposited through PECVD, whereas fast molecular diffusion is the dominant transport mechanism in lower density films [157, 158]. The transport mechanism may therefore change throughout an annealing process since films tend to densify as annealing progresses. Although H diffusion has been studied in films prepared by similar methods to ECR-PECVD (as used in this thesis), in light of references [157, 158] it seems likely that H transport in films may vary significantly between samples prepared in different laboratories. Further, the films studied in this thesis were pre-annealed at high temperatures, the impact of which on H diffusion has not been tested. In addition, the SiO_2 cladding and Si substrate will absorb H,

---

[21] The symbol H has been used in this thesis to represent the element hydrogen, with no reference to its bonding arrangement. "Atomic H" refers to an un-bonded H atom.

complicating matters considerably (not to mention the presence of 4 interfaces). For these reasons, quantitative analysis of H diffusion into and out of SiN_x films (and its impact on optical loss) is not attempted in this thesis.

Qualitatively, the data presented in this section is consistent with the references described in the previous two paragraphs. All samples yielded a low ~3 dB/cm loss, except when annealed at high temperatures in the presence of H_2. The remaining loss may be due to either residual H in the film and/or to scattering. It appears that high temperature annealing at 1100 °C for 2 hours in N_2:H_2 incorporates H into the film, significantly increasing the material loss. The incorporated H can be (partially) desorbed though a second high temperature anneal in N_2. Note that while the diffusivity of atomic H in SiN_x is very small, H is considered to be mobile in SiO_2 at temperatures as low as 400 °C [61] This provides a fabrication window whereby H can be absorbed into Si-nc films without significantly impacting the loss of the SiN_x. This annealing window appears to be as high as 600 °C for 2 hours. Further, SiN_x may act as a diffusion barrier, and therefore must be placed under the Si-nc layer. While a fabrication window exists for Si-nc in SiO_2 films, the situation may not exist for Si-nc films embedded in a SiN_x host.

5.6 Si-ncs integrated with SiN_x core slab waveguides

Si-nc films integrated in slab waveguides were fabricated using an air/Si-nc/SiN_x/SiO_2 structure. Devices were characterized with streak and SES measurements. The samples were two-sectioned devices that contained an emitting section with a Si-nc layer, and a transmitting section with no Si-nc film, as shown previously in Figure 10 (Top) on page 68. The two sections have distinct waveguide loss values. The transmission sections are air/SiN_x/SiO_2 waveguides, and have been discussed in the previous section.

In the SES setup, PL is generated at a spot within the emission section, and propagates out the left facet (of the emission section) as well as the right facet (of the transmission section) of the device. Ignoring reflections at the facets, left traveling light is not affected by the presence of the transmission section, and may therefore be used to independently characterize the emission section. This is considered first. Emission from the right facet, showing the operation of the two-sectioned device, is considered later in this section.

Figure 41 shows loss measurements of an air/Si-nc/SiN_x/SiO_2 waveguide, made at different wavelengths using the streak and SES method. In the SES measurements, light was collected from the emission section facet. In the streak measurements, only the emission section was measured.

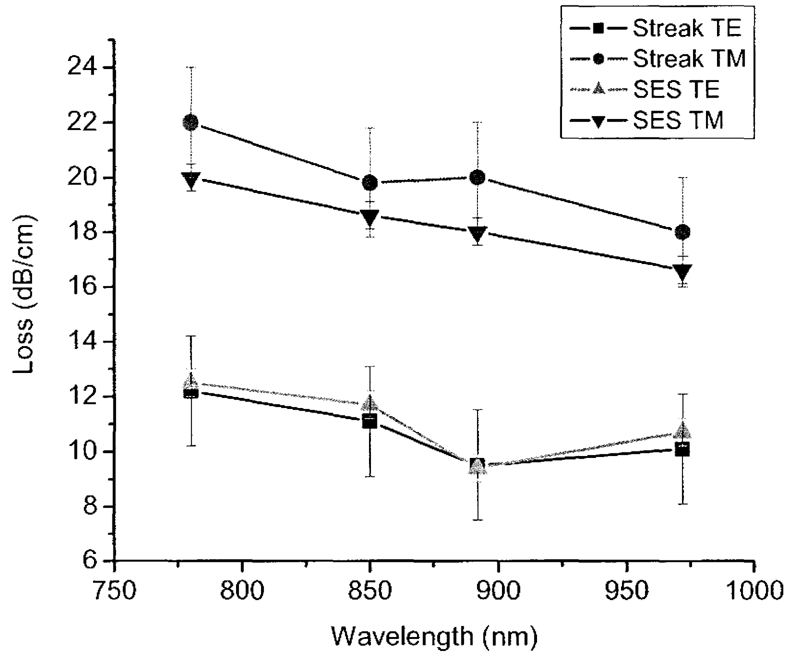

Figure 41: Loss measurements of an air/Si-nc/SiN_x/SiO_2 waveguide (035x1) at different wavelengths. The device contains a 200 nm thick Si-nc film, deposited on a 300 nm thick SiN_x film, and has been annealed in the two-step process.

Wavelength (nm)	Waveguide Loss (+/- 2 dB/cm)		TE/TM Meas. (+/-30%)	TE/TM Theory (+/-0.05)	Material loss from Si-nc layer (dB/cm)	
	TE	TM			TE (+/- 25%)	TM (+/-15%)
780	12.2	22.0	0.49	0.61	96	119
850	11.1	19.8	0.49	0.63	77	99
892	9.5	20	0.40	0.64	60	98
972	10.1	18	0.48	0.68	60	85

Table 12: Loss measurements of an air/Si-nc/SiN_x/SiO_2 waveguide at different wavelengths using the streak method. The data corresponds to that of the above figure. The 4th and 5th columns of numbers show the measured and theoretical waveguide loss ratios due to the Si-nc layer, taking into accounted a 2.7 dB/cm material loss of the SiN_x film.

Table 12 shows the waveguide loss measured through the streak method at each wavelength. Although the material loss of the Si-nc layer is large, there is

only a 12 % and 20 % overlap of the layer with the mode for the TE and TM polarizations respectively. The resulting waveguide loss is much lower than the losses measured in Si-nc core waveguides. From the previous two sections, the SiN_x loss is known to be ~2.7 dB/cm, whereas the material loss from of the Si-nc film is much larger, though its reproducibility is yet untested. Despite this unknown, the description of loss presented by equation (7) can still be tested by comparing the ratios of the waveguide loss of the two different polarizations, though a small correction is required. Columns 4 and 5 show the measured and theoretical ratios of the TE/TM waveguide loss introduced by the Si-nc film. Columns 6 and 7 show the corresponding Si-nc material loss. For all four columns it is assumed that all waveguide loss is due to material loss from the Si-nc film, except for the small contribution from the SiN_x layer, $n_{SiNx}\Gamma_{SiNx}/N_{eff}$*2.7 dB/cm (this amount introduces ~2-3 dB/cm of waveguide loss throughout the four wavelengths). It is seen that the difference between the measured and theoretical values is very near (or just beyond) the limit of the measurement uncertainty. (If the SES measurements are used for the calculation instead of the streak measurements, the results are in much closer agreement). Whereas the material loss of the Si-nc film should be polarization independent, it is seen from columns 6 and 7 that the material loss based on the TM polarization measurements is consistently higher than the material loss obtained from the TE measurements. It is not clear if this is due to measurement uncertainty or if the loss description of

multilayer films given by equation (7) is an incomplete description, which needs to be modified to include surface scattering loss. It is expected that as the waveguide loss decreases (as a result of a thinner Si-nc layer), interface scattering losses will become more significant. Note that the measured material loss of the Si-nc film is approximately twice as high as that measured on sample 016x3 (section 5.4), although the wavelength dependence is similar. Three other air/Si-nc/SiN_x/SiO_2 waveguides have been fabricated. Streak and SES measurements show material loss values for the Si-nc layer ranging from that of 016x3 to that of the just presented sample, 035x1. This is further evidence that an irreproducibility of loss exists in the Si-nc fabrication process. However, all four devices functioned as waveguides with optically pumped integrated emitters, as evidenced by the consistency of the streak and SES measurements.

The amount of power coupled to the slab waveguide is given by the spontaneous emission factor, β. As discussed in section 3.1.3, β can be approximated as being proportional to the modal overlap with the emitting layer, $\Gamma_{Si\text{-}nc}$. This assumption was tested by comparing the ratio of the SES signal for the TE and TM polarizations. Since the two polarizations experience different propagation losses in the SES measurement, the ratio of the TE and TM polarized SES signal must be measured at (or extrapolated to) the facet. The results are shown in Table 13. The approximation of β's proportionality on $\Gamma_{Si\text{-}nc}$ appears to be reasonable, however, only a small range of $\Gamma_{Si\text{-}nc}$ is explored in this work.

Since the polarized modes experience different waveguide losses, during SES measurement the ratio of the power at each polarization emitted out the facet will depend on the position of the excitation spot, as demonstrated in Figure 42.

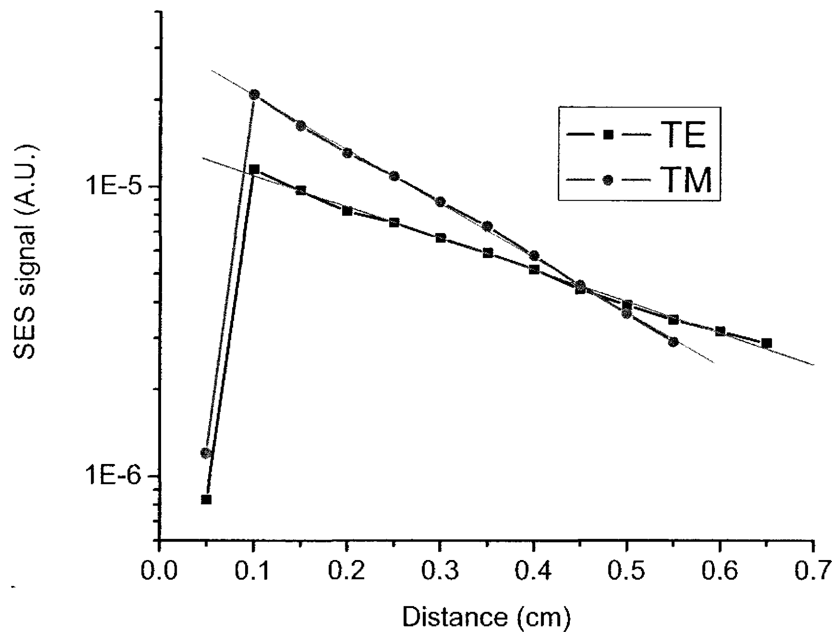

Figure 42: SES measurement showing the un-normalized power carried by the TE and TM polarizations for sample 035x1. (Other SES plots shown previously have the TE and TM powers normalized to the peak signal separately). Light was collected in the low-magnification SES setup, hence is a broad band measurement dominated by the peak wavelength. The initial rise in signal shows the location of the facet, with lines to "guide the eye". Lines of best fit (ignoring the initial rise) are also shown, and have slopes of 10.9 and 18.7 dB/cm for the TE and TM polarizations respectively. The spatial resolution of the measurement is determined by the laser beam clip width of 204 μm. The horizontal axis is aligned to acquire the peak signal.

Sample	$\Gamma_{TE,Si\text{-}nc}$	$\Gamma_{TM,Si\text{-}nc}$	Theory $\Gamma_{TE,Si\text{-}nc}/\Gamma_{TM,Si\text{-}nc}$ (+/-0.05)	Measured Edge Power *TE/TM* (+/-4%)
035x1	0.12	0.19	0.63	0.52
080x1	0.12	0.19	0.63	0.68
070x1	0.08	0.11	0.73	0.71

Table 13: Ratio of the measured edge power of the TE and TM polarizations of SES measurements. Measured values were taken with the PL excited at the facet, in the low-magnification SES setup. Calculated values for the confinement factors of the Si-nc layers at 850 nm are also shown. Three samples are considered. The first two are comprised of a 200 nm thick Si-nc layer, while the last sample contains a 100 nm thick Si-nc layer. All three devices contain a 300 nm thick SiN_x core.

As is the case with Si-nc core waveguides, edge emission spectra collected from air/Si-nc/SiN_x/SiO_2 waveguides is consistent with the description presented in Chapter 3. The edge emission spectrum resembles the "intrinsic" emission from the Si-nc layer, subject to a distortion of the form $e^{b\lambda x}$ introduced by a wavelength dependent loss. Due to the lower loss values, this distortion is much smaller than is observed in Si-nc core waveguides. This behaviour was consistently observed in all four waveguides tested. For example, consider the edge emission from the device presented in Figure 43. The TE and TM polarized edge emission spectral shapes overlap. Further, both spectra resemble that of surface emission from a single layer Si-nc film. (Note that the Si-nc films of the waveguide and single layer film were deposited with the same refractive index, but the single layer film was been annealed at 1100 °C in Ar_2:H_2, where as the waveguide was annealed in the two-step process. The impact of the different annealing procedures on the PL spectrum has not been rigorously tested, but, from measurements in section 5.1, is believed to be quite small). Regardless, the edge

emission with an excitation spot close to the facet was successfully used in section 5.1 to model the surface emission in the same sample. It appears that while β differs in magnitude between the two polarizations, it is largely wavelength independent over the emission spectrum. This is consistent the approximation that β is proportional to $\Gamma_{Si\text{-}nc}$. For this structure, $\Gamma_{Si\text{-}nc}$ varies by only 6% over the FWHM of the emission spectrum.

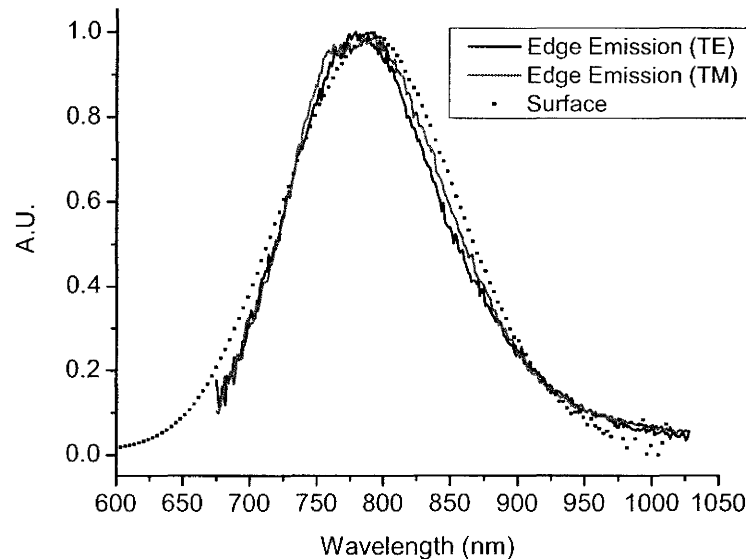

Figure 43: Edge emission spectra of an air/Si-nc/SiN$_x$/SiO$_2$ waveguide. PL is excited 2 mm from the facet of sample 035x1. Also shown is the surface emission from a single layer Si-nc film. All curves are normalized separately.

An example of the distortion introduced by the wavelength dependent loss is shown in Figure 44. The red-shifting of the spectrum with increasing distance of the excitation spot from the facet is apparent, although, through normalization, highly influenced by the noise. A small shoulder in the TM spectra is apparent at 760 nm, and is believed to result from improperly blocked surface emission, as will now be explained.

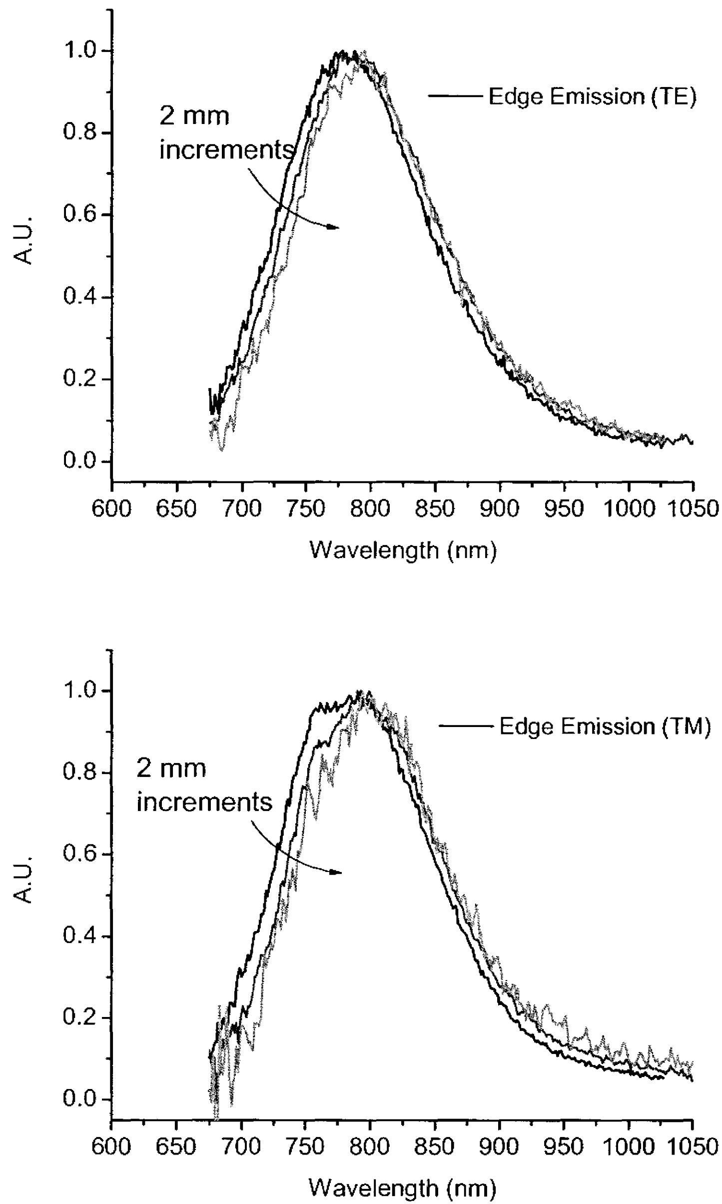

Figure 44: Edge emission spectra of an air/Si-nc/SiN_x/SiO_2 waveguide with incrementing excitation positions. PL was collected in the SES arrangement on sample 035x1 with the excitation spot positioned at 2 mm increments from the facet, starting at 2 mm from the facet. The top and bottom show the TE and TM polarized edge emission respectively. Each curve is normalized to its peak value separately.

While the edge emission appears to be largely dominated by light traveling as waveguide mode, radiation modes are also present. Radiation modes propagating in the lower cladding at angles almost parallel to the film surface are spatially and angularly indistinguishable from the guided mode after transmission through the facet. Since the waveguides are formed on a Si-substrate, these radiation modes will be propagating in both upwards and downwards directions. Facet emission cannot be spatially filtered (by blocking a portion of the facet) since the mode extends into a large portion of the lower cladding (the substrate is opaque, and does not need to be blocked)[22]. However, surface emission may be easily blocked with a knife edge, as discussed in section 4.3. Here it is noted that significant spectral structure may be observed if surface emission is improperly blocked. For example, Figure 45 (Top) shows two knife positions that sufficiently blocked surface emission. With the knife at the surface height, and either resting on the sample or positioned well in front of the facet, surface emission was entirely blocked. With the blade positioned in front of the facet, ~1/2 of the guided emission (and any radiation modes emerging from the facet and propagating at upward angles) was also blocked halving the overall signal. The (Bottom) graph shows two knife positions that did not sufficiently block the

[22] Facet emission may be angularly resolved and filtered using Fourier optics. Such a procedure was used in [98] to block substrate radiation modes propagating at downward angles in Si-nc waveguides fabricated on silica.

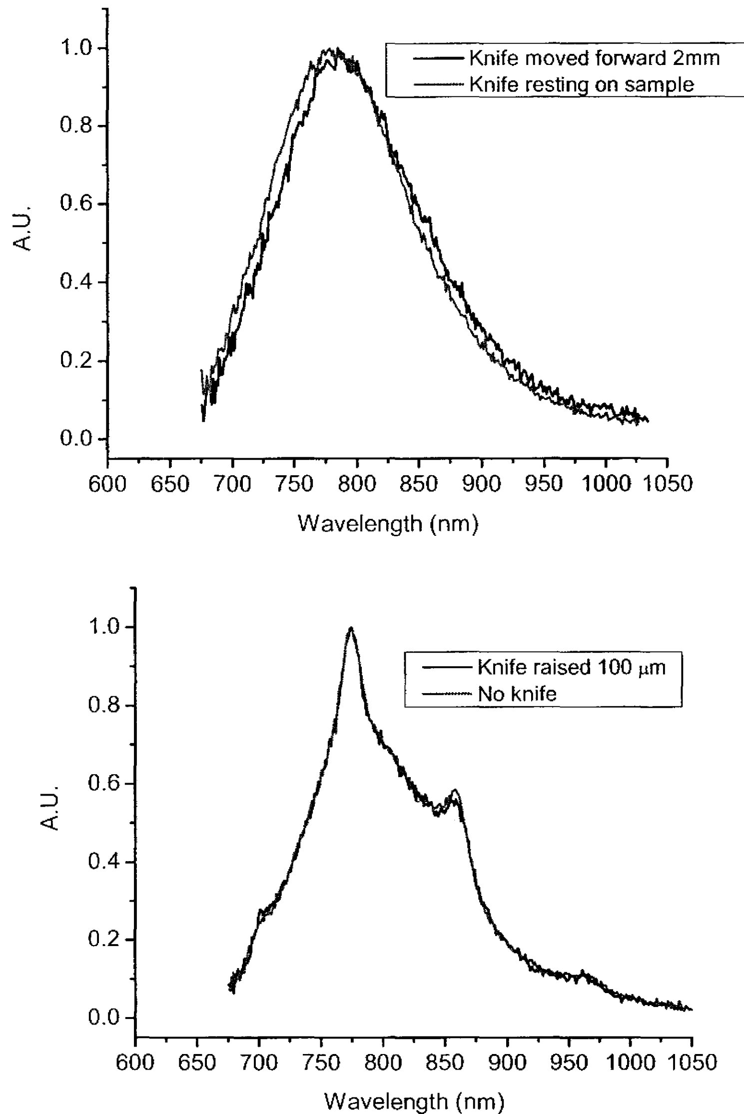

Figure 45: Edge emission spectra collected with the SES setup using 4 different knife positions. For both figures, the excitation spot was 2 mm from the facet, and the TE polarization spectra were measured, normalized each to their peak values separately. (Top) Shows emission spectra collected with the knife resting on the sample at the facet. Also shown is the emission when the knife was positioned at the surface height, but located 2 mm in front of the facet. (Bottom) Shows emission with the blocking knife positioned at the facet, but raised 150 μm from the surface. This allows a 4° window for surface emission to enter the collection optics. Also shown is emission spectrum with no blocking knife.

surface emission. With the knife edge raised or absent, some surface emission wsa allowed to pass. The wavelength spacing of the extra peaks was confirmed by simulation to be consistent with interference modulated surface emission collected at ~88° to the surface normal.

Emission collected from the transmission facet is now considered. Three two-sectioned devices have been fabricated, with Si-nc emission regions coupled to a 300 nm thick SiN_x core waveguide. Devices 070x1 and 071x1 contain a 100 nm thick Si-nc layer, whereas 080x1 contains a 200 nm thick Si-nc layer. Strong coupling from the emitting region to the transmitting region was evident in all three devices. This is illustrated in Figure 46 - 48, which show streak and SES measurements across the transition region for the TE polarization light at 780 nm. Each streak measurement produces two loss measurements; one for the emission and one for the transmission regions. In the two samples fabricated using a photoresist liftoff procedure, the emission regions are much shorter than the transmission regions, as a consequence of the mask design. For this reason, the prism was coupled to the longer transmission section, hence the mode was traveling backwards, towards the emitting region. This is the opposite direction compared to the normal operation of the integrated emitter. However, for a linear system, this result is reversible. A schematic of the measurement setup is included above each graph. Since a large signal spike was (sometimes) present at the transition point, linear fits were performed using the data on either side of the transition point, but not including data points near the transition point. SES

measurements were performed with the pump laser scanned across the emission region with PL collected out the transmission facet, after propagation through the low loss transmission section. The rising and falling of the SES signal correspond to the laser reaching the beginning and (possibly) ending positions of the emission section.

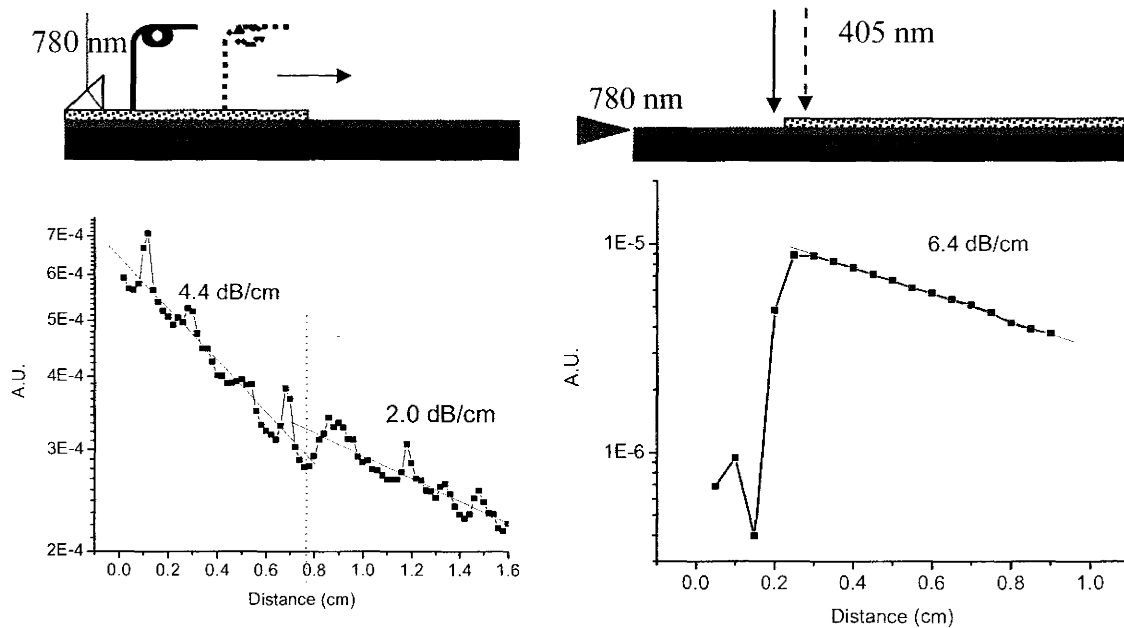

Figure 46: (Left) Streak measurement on the two sectioned device, 070x1, formed from masked deposition using a glass cover slide. TE polarized 780 nm light was prism coupled in the emitting region of the chip. A dotted line shows the transition point. (Right) SES measurement at the same wavelength and polarization. PL was collected out the transmitting facet after propagation through a 16 mm long transmission region.

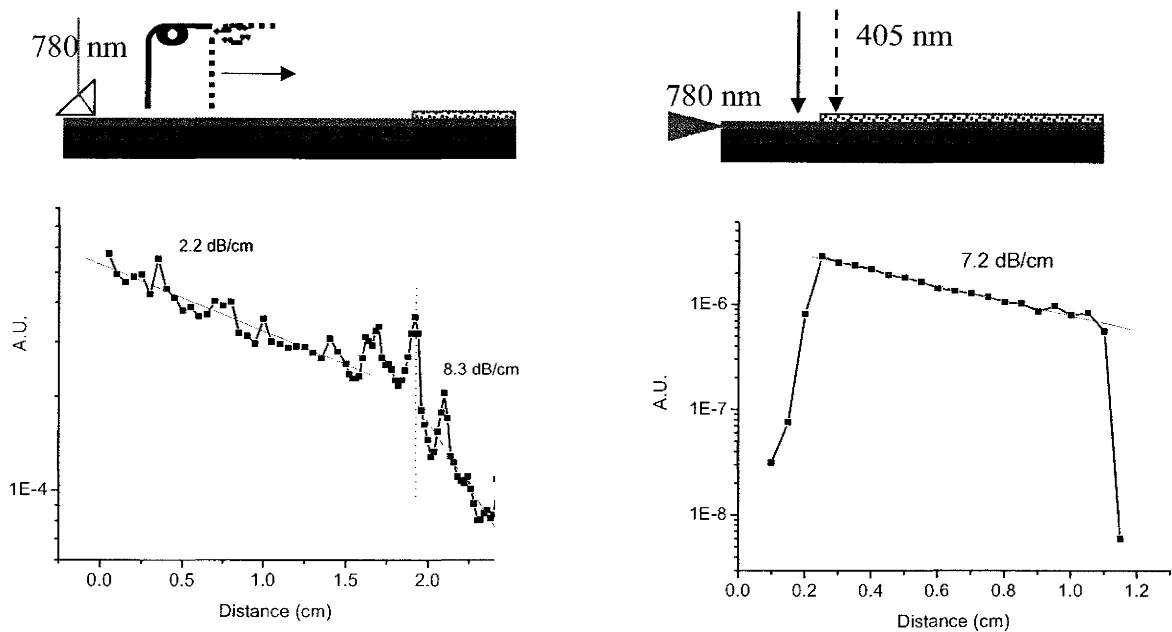

Figure 47: (Left) Streak measurement on the two sectioned device, 071x1, formed from masked deposition using photoresist liftoff. TE polarized 780 nm light was prism coupled in the transmitting region of the chip. A dotted line shows the transition point. (Right) SES measurement at the same wavelength and polarization, collected out the transmitting facet after propagation through a 5.5 mm transmission region. The length of the transmission region is less in the SES measurement than in the streak measurement. This is due to the fact that a different area of the chip is used for the two measurements.

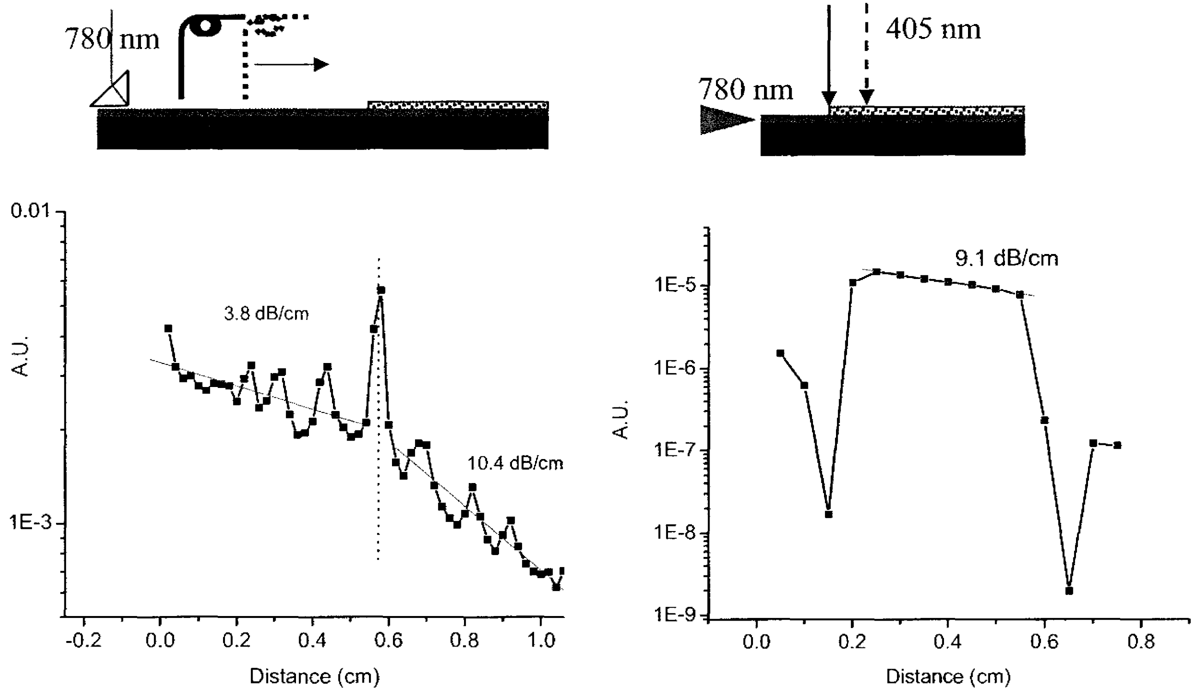

Figure 48: (Left) Streak measurement on the two sectioned device, 080x1, formed from masked deposition using photoresist liftoff. TE polarized 780 nm light was prism coupled in the transmitting region of the chip. A dotted line shows the transition point. (Right) SES measurement at the same wavelength and polarization, collected out the transmitting facet after propagation though a 6 mm long transmission region.

The streak measurements, based on the noise and reproducibility, have an uncertainty of +/- 1 dB/cm, whereas the SES measurements have an uncertainty of +/-0.5 dB/cm. Good agreement is observed between the loss of the emission regions as measured by the streak and SES techniques. (The SES loss measurement of device 070x1 appears to be 0.5 dB/cm too high. This may be an artifact of the measurement. In this device, the transmission region was very long, hence the excitation spot was very far from the focused facet which may introduce a system loss, as discussed in section 4.3). The agreement between the streak and SES measurements shows that the devices functioned as integrated

emitters, launching modal power from a Si-nc emission region into a SiN_x core waveguide. Both fabrication methods, either masked deposition using a glass cover slip or photoresist liftoff, yield similar results. A knee in the streak measurements is clearly visible.

Further inspection of the streak measurement reveals a signal spike at the transition point, presumably caused by the discontinuity of the waveguide. This spike is not present in the sample fabricated using a glass slide cover slip mask since the transition is visibly less abrupt. Note that extrapolation of the linear fits of the streak measurements across the transition point are approximately continuous. This suggests a high mode coupling between the two sections. Poor coupling would cause the signal level to drop after propagating through the transition region, creating an offset. If it is assumed that the probability of scattering out the surface is equal in the two sections, the offset of the loss line fits of the two sections at the transition point is a measurement of the coupling loss. Under this assumption, the coupling loss is buried in the noise of the measurement, and is therefore quantified as being less than 1 dB.

The coupling between the emission and transmission regions was also measured using the staircase pattern of device 071x1. This technique measured a coupling efficiency of 105% +/- 5%. Clearly a coupling efficiency greater than 100 % is unphysical, and is the result of an erroneous assumption. By scanning the pump laser parallel to the facet direction while monitoring the edge emission, it appears that the facet loss across the device was not constant, but varied by at

least 10%. It is also possible that the coupling efficiency was not constant along the transition region.

An example of edge emission spectra from a two-sectioned device is shown in Figure 49. As expected, the spectra resemble the “intrinsic” emission spectrum of the Si-nc layer. In this device, very little spectral shift from material loss is observed in the TE polarization, although some red-shifting is observed in the TM polarization, due to the higher propagation loss in that mode. The TM polarization spectra also contain a small shoulder at 760 nm, indicating a small contribution from radiation modes, most likely surface emission. Also shown is edge emission using a 470 nm pump LED instead of a 405 nm focused diode laser. The LED housing was suspended 1.0 mm from the substrate, above the transition region. The use of an LED demonstrates the plausibility of a pumping scheme with simpler alignment than can be accomplished with a collimated laser beam. The use of a pump LED provides a lower intensity over a larger area, and therefore reduces the alignment required of the setup at the possible expense of overall pumping efficiency. LEDs have been considered by others to be a low cost substitute for lasers in pumping Si-nc devices [104]. Compared to spectra obtained from laser pumping, the spectra from LED pumping is red shifted, which is expected since the LED pumps a larger area, which will result in longer propagation lengths through the emission region. Also, the LED pumping intensity was lower than from the focused laser, which results in a slightly red-shifted emission spectrum.

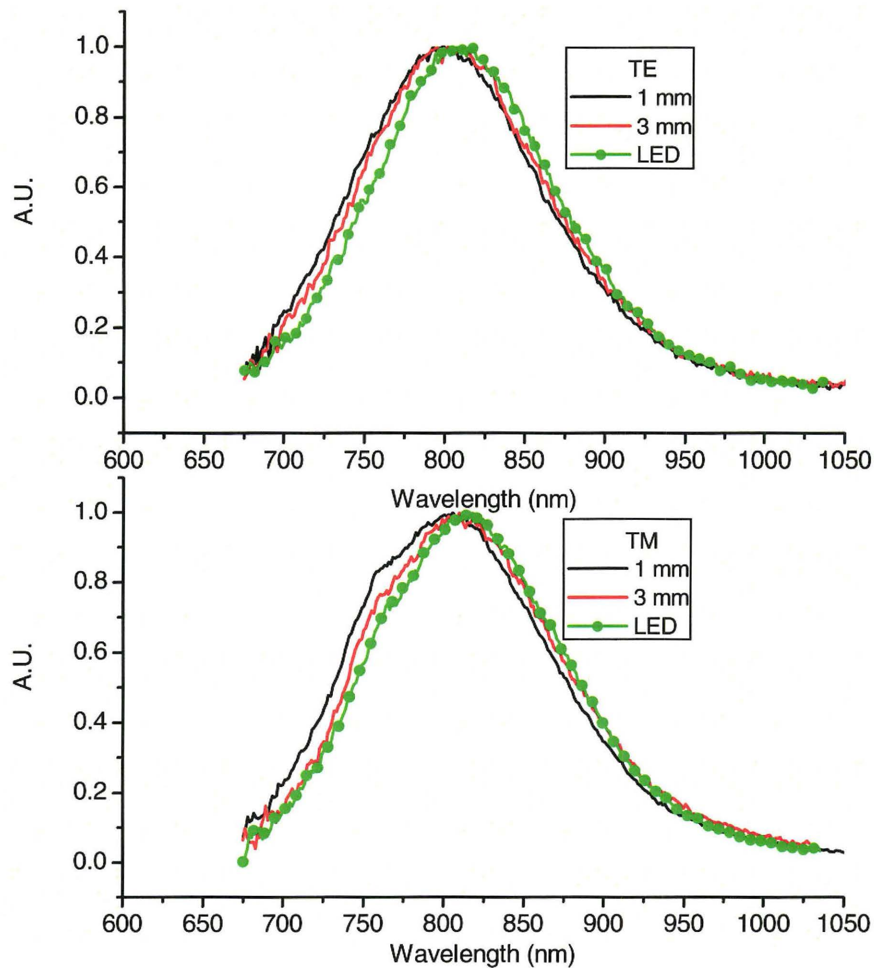

Figure 49: Edge emission spectra collected out the transmission facet of the two-sectioned device, 080x1 for the TE (Top) and TM (Bottom) polarizations. Two spectra are shown for each polarization, with the excitation spot positioned 1 and 3 mm from the transition region. The transmission section is 6 mm long. Also shown is the edge emission obtained using 470 nm LED pumping, with the LED positioned 1.0 mm above the sample surface, centred at the transition region.

The edge emission power was quantified on sample 070x1. With 460 μW of laser light excited at the transition point, 2.4 nW of broad band edge emission was detected at the facet after propagation through a 16 mm long transmission

region. From the model discussed in Chapter 3, it is difficult to predict the edge emission power based solely on the pumping arrangement and collection optics. Such a calculation would require detailed knowledge of the device. Half of this problem is circumvented by considering the relationship between the surface and edge emission power. The edge emission power, P_{edge}, can be written as

$$P_{edge} = P_{PL}\beta e^{-\alpha x} T f_{lens} \tag{25}$$

where P_{PL} is the PL power generated within the Si-nc layer, x is the distance from the excitation spot to the facet, T is the facet transmission, and f_{lens} is the collection efficiency of the output lens of the SES setup. Note that the collection angle of the lens in the plane of the waveguide is already included in the definition of β. The collection efficiency perpendicular to the plane of the waveguide is calculated as the partial integral of the far-field intensity of the mode with the collection angle of the lens. Similarly, equation (18) can be rewritten to describe the surface emission,

$$P_{surface} = P_{PL}\left(\frac{1-\cos(\theta_{cr})}{2}\right)(1-R) f_{lens} \tag{26}$$

Here, reflections from the bottom film boundaries are ignored. Comparison of $P_{surface}$ and P_{edge} is therefore independent of the pumping efficiency and quantum efficiency, since P_{PL} is constant and contains both quantities. This technique was carried out on sample 070x1. Edge emission was collected using the low-magnification SES configuration out the emission region facet while surface

emission was collected near normal incidence. Both measurements are therefore broadband. To calculate β, an average of the TE and TM parameters are assumed. To consider the validity of the above description, the discrepancy between the two measured values for P_{PL} is placed entirely on the parameter T. For the surface and edge power measurements to result in the same value of P_{PL}, T calculates to 0.093 (or, -10.3 dB). Although this is one tenth the theoretical maximum of 0.93 based on the Fresnel reflection, the value is reasonable for unpolished facets[23].

Thus far, only spontaneous emission has been considered. As reviewed in Chapter 2, gain in Si-nc waveguides has been observed by some groups using the VLS method. Here, gain was explored using the prism coupling setup, as described in section 4.3. The results are preliminary, not quantified, tested under only a limited parameter space, and are therefore relegated to Appendix I. However, the results are surprising, and therefore included in this thesis in the hopes of encouraging future work.

5.7 Summary of the integration of Si-ncs in waveguides

The evidence shown here supports the model described in Chapter 3. There, it is assumed that edge emission is due to the propagation of a fundamental

[23] It is difficult to compare this value with those from other groups. Very few groups publish facet loss values unless the facets have been polished. In our lab, unpolished facets from SOI waveguides, formed through cleaving, exibit losses of 8-12 dB.

mode. Such behaviour was shown to occur for waveguides formed with Si-nc as well as SiN_x cores. Waveguide loss was found to primarily result from absorption in the Si-nc layer. A two-sectioned device operating as an integrated emitter coupled to a low loss transmission waveguide has been demonstrated.

The potential for the system to function as an evanescent bio-sensor appears promising. As reviewed in section 2.3.1, such bio-sensors based on Si_3N_4 waveguides have been demonstrated and are under development. In this chapter, the observed knee in the streak measurements of the two sectioned devices shows there is a benefit to having a Si-nc free region. Compared to a single section device, light is directed to propagate not only to a region with lower loss but also a region with larger modal overlap with the upper cladding material (in this case, air). Such a property is desirable for evanescent sensors.

It is suggested that future work should aim at accurately measuring the loss of Si-nc films and SiN_x films under different annealing recipes with different refractive index samples. In the output from an integrated device, the emission efficiency is directly offset by loss (see equation 14). The ratio of pair must be considered. It is also possible that significant loss was introduced through surface roughness caused by strain relief during annealing steps. This should be investigated. Other researchers have reported very low loss values, < 1 dB/cm, in the visible for SiN_x films [128], which encourages the search for similar performance from the system at McMaster.

To understand the loss mechanisms, it is necessary to distinguish between absorption, and scattering from the bulk or surface. This may be accomplished several ways. Radiometric measurement of the scattering power is possible, but experimentally difficult. Interface scattering may be differentiated through comparison of waveguides with different core thicknesses. As already discussed, photothermal deflection provides a sensitive absorption measurement.

In several places in this chapter, conclusions were drawn from a small set of devices. Obtaining multiple, near identical samples has been identified as a means to measure the reproducibility of the material parameters. However, this does not test the correctness of the theory. To add credibility to the theory of device operation presented in this thesis, devices should be fabricated with a variety of film thicknesses.

Two unexpected properties in Si-nc PL were presented. The PL power was seen to fatigue and partially recover after optical excitation. Similarly, material loss was seen to increase and partially recover after optical excitation. These two properties warrant further investigation.

For development of a useful integrated emitter, future work should consider a ridge waveguide design. Such a design may benefit from a tapered waveguide geometry, with a wide ridge in the emitting region that narrows to a single mode ridge near the transition into the transmission section. Such designs are used routinely for mode converters, to aid fiber-chip coupling. With some restrictions on the taper angle, low loss propagation is still possible. This may

allow a larger emitting area (and therefore a larger PL signal) to be coupled to a single mode 3-D guide. Such a design takes advantage of LED pumping, which is cheaper, though less spatially confined than a laser source. A tapered design also relieves fatigue and saturation issues of the PL of Si-nc films by allowing the optical power to be delivered to a larger chip area.

The integrated device may benefit from a different fabrication method, using ion implantation to form the Si-ncs. For example, a two sectioned device may be formed from masked implantation of Si into thermal oxide, followed by annealing to form Si-ncs, followed by SiN_x deposition. Such a design has several benefits to the devices fabricated here. The SiN_x remains planar, but does not need to be annealed. This may improve surface roughness and waveguide loss.

Chapter 6. Results and Discussions on Defect Engineered LEDs

6.1 Photoluminescence of Defect Engineered Si

Photoluminescence of bulk and SOI structures were measured. While the end goal of the DE project is electroluminescence, PL spectra give valuable diagnostic information of the emission properties, without the need for processing electrical contacts. Since EL efficiency was easily obtained, PL efficiency was not measured.

Recall that Table 2 - Table 4, starting on page 64, describe the structure and processing route used to fabricate each device.

The PL process in crystalline Si is as follows. Pump light is directed into the sample through the top surface and is absorbed creating high energy electron-hole pairs which quickly thermalize to the band edge. The absorption coeffcient of the 514 nm pump light in Si is $1*10^4$ cm^{-1}. Therefore 86 % of the pump power is absorbed after only 2 μm of propagation into the sample. In the SOI samples used here, the majority of carrier generation occurs in the Si overlayer, as opposed to the substrate. The carrier diffusion length in Si is typically 10-100 μm, so although the carriers are generated close to the surface, significant diffusion will occur. In bulk Si, excess carriers will diffuse deep within the substrate. In the case of SOI with overlayer thicknesses of ~1.5-5 μm, it is approximated that

diffusion causes the carrier concentration to be uniform with depth. Lateral diffusion across the surface of the sample will also occur, but is insignificant relative to the pump beam diameter. This is the case for unimplanted samples. In implanted samples, which contain significant numbers of dislocations following post-implantation annealing, this description may not be valid.

The excess carriers diffuse and recombine, emitting light at the band edge (and at 1.5 μm if the sample contains Er). Re-absorption of PL is insignificant at the peak wavelength for the propagation lengths considered. The absorption coefficient of room temperature Si varies from 40-0.06 cm^{-1} over the range of 1.0-1.2 μm, and is only 0.35 cm^{-1} at the peak wavelength of 1.16 μm [144]. While the high energy emission tail may be slightly absorbed, the majority of the emission spectrum is not affected by re-absorption. Even in the SOI structures, where the PL takes multiple transits across the cavity, loss from re-absorption is insignificant compared to the Fresnel loss experienced from the reflection at each interface. Reflections from the backside of the wafer are ignored since the resulting interference period is beyond the resolution of the spectrometer. Further, the back surface is rough and therefore results in diffuse reflection.

An example of PL from bulk Si, implanted and unimplanted, is shown in Figure 50. The emission peak of the unimplanted sample was 1.158 μm, which is near the expected phonon down shifted band edge of 1.162 μm. The spectral FWHM was 62 nm. The DE sample also emitted light near the down-shifted band edge, centred at 1.147 μm, with a FWHM of 79 nm. The increase in spectral

width of the DE sample is predominantly in the high energy shoulder, perhaps indicating emission occured nearer the surface than the unimplanted sample, and therefore experienced less re-absorption. The DE sample also emitted a 217 nm wide band centred at 1.55 μm. Homewood attributes this peak to emission from Er since it is only observed in samples containing Er. Curiously, the DE sample emited less light than the unimplanted sample. The PL emission power (area under the spectrum) of the unimplanted sample was 5.7 times larger than the DE sample. Note that both wafers were initially obtained from the same wafer box. An identical reduction was observed with SOI samples from the Surrey II batch having undergone route A and route B. The DE technique appears to *reduce* the emission efficiency, at least under optical excitation. This observation contradicts previous reports from Homewood. In [36], it is reported that "No PL was seen from unimplanted material." Admittedly, the DE model only claims to enhance emission in the small volume between the loops (at a depth of ~100 nm) and the junction (at a depth of ~400 nm). Optical excitation explores a much larger volume of Si, exciting carriers more deeply within the sample. It is also curious that the epitaxial layered Si samples, both unimplanted and implanted, exhibit very low, almost undetectable, PL signals. Epitaxy is known to produce Si layers with much lower impurity concentrations than the CZ method. The low PL signal from expitaxially grown Si cannot be explained under the conventional framework discussed in Chapter 2.

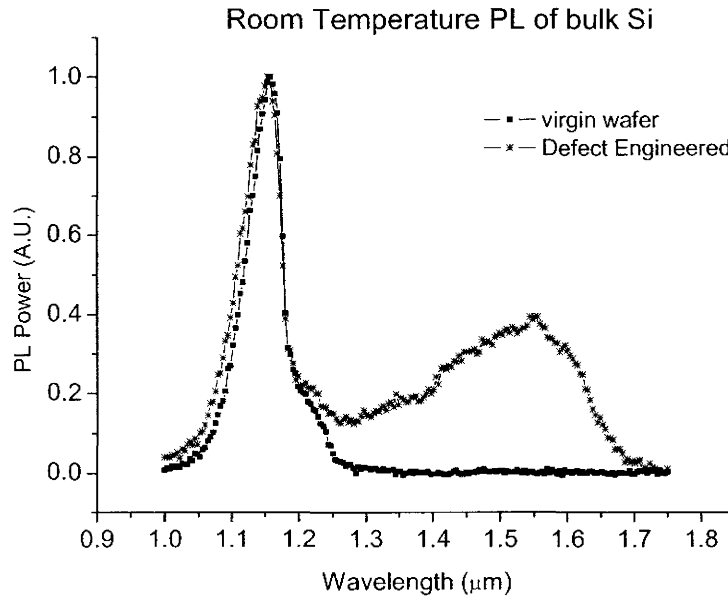

Figure 50: Room temperature PL of virgin and DE bulk Si fabricated by route C*:Er. Each curves is normalized separately to its peak value.

Photoluminescence from SOI is modified by the cavity. Calculation of the interference function, *F*, requires knowledge of the film thickness and material dispersion of all layers with high precision. These were measured with spectroscopic IR ellipsometry providing thickness measurements to within +/- 10 nm. In addition to material dispersion, the refractive index of Si will be severely modified through the free carrier effect introduced by the high density of carriers generated by the pump light. The introduction of lattice damage also would be expected to perturb the refractive index [159], although this is assumed to be a relatively small effect and has been ignored in this work.

In this analysis, dispersion (arising from the free carrier effect) and observation angle are used as all-encompassing fitting parameters. It is assumed

that identically prepared bulk Si and SOI wafers generate the same PL spectrum, except the later is modified by F. A fitted spectrum is obtained by multiplying the bulk emission spectrum by F. Due to carrier diffusion, emission is assumed to occur uniformly throughout the Si overlayer. Si material dispersion and collection angle are varied to obtain an acceptable fit. The refractive index, $n(\lambda)$, is shifted from its measured value $n_o(\lambda)$, in the second order, $n(\lambda)=n_o(\lambda) + A + B\lambda + C\lambda^2$. Due to the periodic nature of the interference function, there are several dispersion curves and angles yield fits of similar quality.

Examples of this analysis for unimplanted and two implanted wafers are shown in the spectra below. For the unimplanted material in Figure 51, the -0.02 shift in refractive index required for fit is consistent with a Drude description in terms of its size and sign [160]. For the two implanted samples, the refractive index shifts (0.522-0.6λ in Figure 52, and +0.05 in Figure 53) appear less physical.

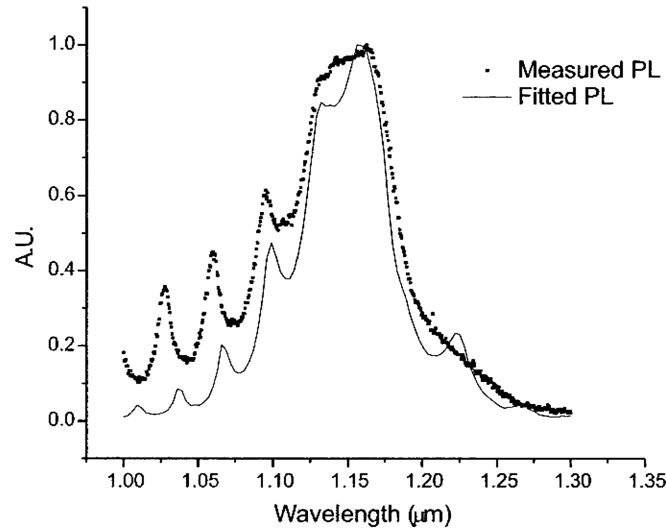

Figure 51: PL from unimplanted 5μm silicon overlayer on 1μm buried oxide SOI. Dots show measured PL. Line is the fitted theoretical PL using an angle of 60 degrees, and an index shift of -0.02 from the intrinsic material dispersion.

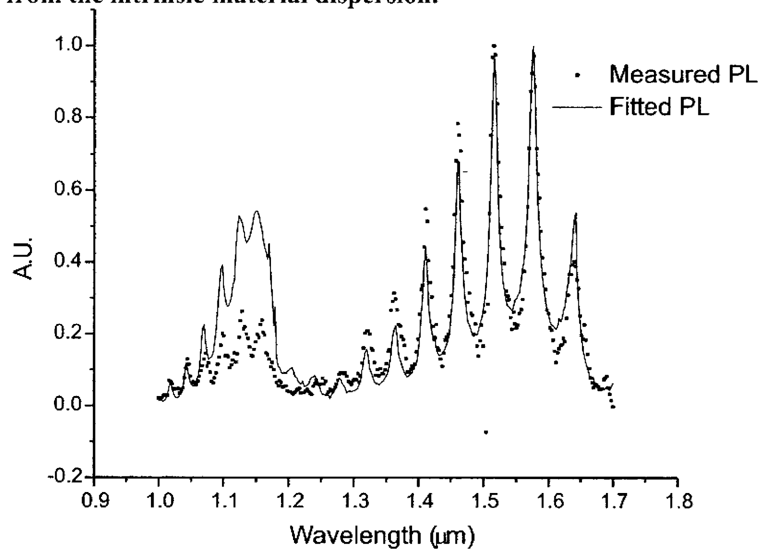

Figure 52: PL from implanted 5μm silicon overlayer on 1μm buried oxide defect engineered SOI, route C:Er. Dots show measured PL. Line is the fitted theoretical PL using an angle of 60 degrees, and an index shift of 0.522-0.6λ from the intrinsic material dispersion.

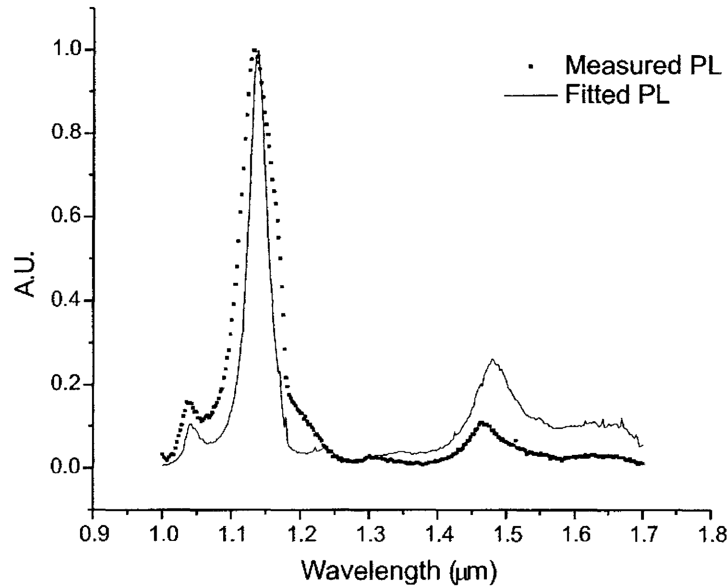

Figure 53: PL from implanted 1.5/1.0 μm SOI, route C:Er. Dots show measured PL. Line is the fitted theoretical PL using an angle of 30 degrees, and an index shift of 0.05 from the intrinsic material dispersion.

Sensitivity tests show that the overlayer thickness uncertainty of ±10 nm is an insufficient source of error to account for discrepancies. The main deficiencies of this analysis are believed to be an inadequate knowledge of the dispersion and collection angle, and to a lesser extent neglecting loss and assuming an infinitesimally narrow collection angle. A systematic fitting routine to minimize the root mean square difference of the theory and measured PL is found not to be effective given inadequate signal to noise ratio. The model has been modified to approximate the implanted region as a separate layer with a distinct dispersion curve from the remaining Si over-layer, but this offers no improvement to the quality of the fits.

This analysis highlights the problems associated with the characterization of light emission in SOI and more generally in multi-layer films. Broad band PL spectroscopy is physically similar to spectroscopic ellipsometry. There, elaborate dispersion and interface models are required for acceptable data fitting [161]. Interference must be accounted for to obtain true spectral features, to relate internal and external quantum efficiency, and most importantly to compare data between different samples or characterization setups. In addition to standard film specifications, such as layer thickness and indices, a detailed knowledge of the dispersion at high carrier concentrations is required over a large spectral width. The effect of implanted layers on the passive optical properties must also be known. These properties can be better accounted for by exploiting the similarity between the emission and transmission spectra for these thick SOI films. While optically pumping the film, the transmission spectrum can be measured with a separate source resulting in a better signal to noise ratio.

Further to this, the data does not rule out the possibility that the underlying assumption, that emission in implanted bulk Si and SOI are different only in that the latter is modulated by F, is incorrect. Indeed, the impact of a buried oxide in close proximity to the implant end of range could lend insight to the debate on the mechanism for the emission enhancement of defect engineered silicon. Also, aside from diagnostics, utilizing cavity induced interference in a positive manner is common place in photonics. For example, surface emission spectra has been

narrowed and external efficiency increased using internal reflectors and multilayer stacks [162].

6.2 Electroluminescence of Defect Engineered Si

EL spectra and the electrical characteristics of bulk LEDs with implantation and anneals similar to route C and C:Er have been published previously [35]. The McMaster facility is not equipped to measure the EL spectra for such low signals, however, an example of the EL spectrum at room temperature of a bulk LED with Er incorporation is supplied by the Surrey lab, and is shown in Figure 54. Forward biased EL and PL match very closely in spectral shape, hence emission is due to recombination of excess carriers, as opposed to a hot carrier impact process often discussed in nano-structured LEDs. In the present study, the LED structures from Surrey I exhibited current-voltage curves typical of a rectifying silicon *p-n* junction with a turn-on at 0.5-0.6V, an example of which is shown in Figure 55.

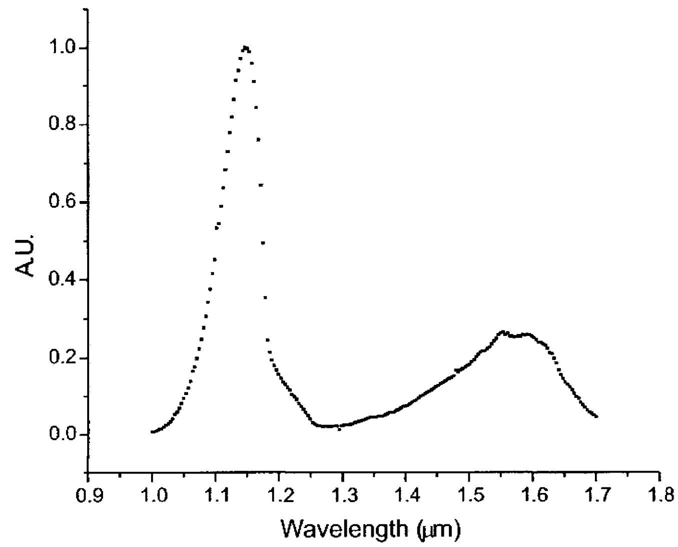

Figure 54. EL spectra of a bulk Si LED with Er implantation.

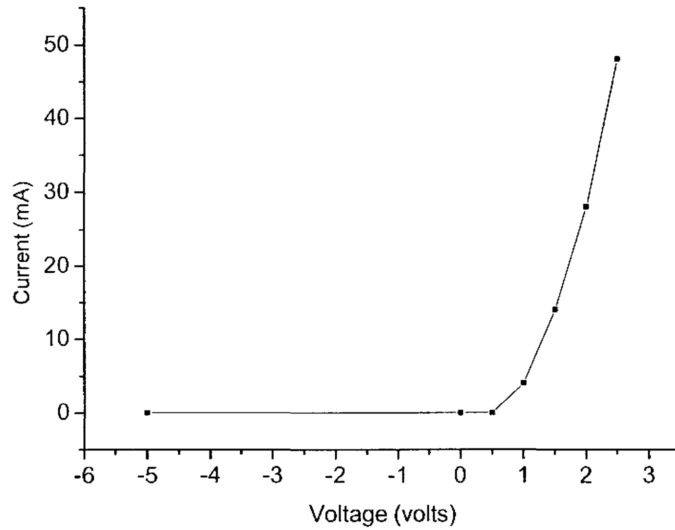

Figure 55: Example of and IV curve for a lateral injected LED. In this example, the device was a 1 mm diameter bulk Si sample, having undergone DE route C.

Figure 56 shows EL power versus current of an implanted bulk Si LED, from route C:Er. Shown are the contributions in the 1.1 and 1.5 μm bands. It is seen that the power emitted in the 1.1 μm band is highly linear with current, while the power in the 1.5 μm band shows signs of saturation and contributes only about a tenth of the overall power. Such saturation may be the result of a finite number of radiative Er centres, or a carrier dependent increase in the rate of back energy transfer of excited Er centres as discussed in section 2.2.5. The external quantum efficiency, η_{ext}, based on the slope of the line of best fit for the total power, is calculated to be $1.2*10^{-5}$ +/- 45%, and takes into account the finite area of the collection optics by assuming uniform emission over a half sphere. The corresponding η_{int} is $8.6*10^{-4}$. The uncertainty of this measurement is estimated from calculations of the sensitivity of the detection system to the optical alignment. Bulk Si LEDs with a backside *n*-contact (instead of an etched top-contact) were measured to be as efficient as top contact LEDs, indicating that introduction of the wet-etched surface does not influence efficiency by way of introducing non-radiative recombination centres. Further, the efficiency did not change by thinning the backside, showing optical absorption is negligible over the substrate thickness. However, the efficiency was found to be 1.5-3 times larger with a roughened back surface as opposed to one that is mirror polished. Such surface texturing has been shown previously both theoretically and experimentally to increase η_{ext} [7]. Some LEDs were found to exhibit a burn-in period (while

held in forward bias) of ~10 hours whereby the efficiency would improve by up to a factor of 2.

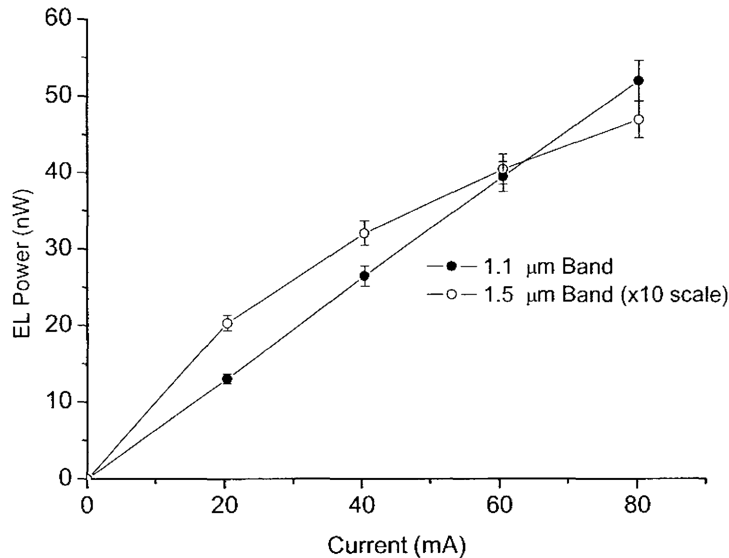

Figure 56: EL power of a laterally injected 1mm diameter bulk Si LED, fabricated using route C:Er. The power axis corresponds to the raw power meter reading in the two lens setup. The emission contains power at the 1.1 and 1.5 μm bands. Using a removable 1300 nm long pass filter, EL power contained in the two bands was measured.

In [31], an efficiency 17 times larger than that reported above is claimed for DE LEDs[24]. The experiments in this thesis were not designed to make a direct comparison. Reference [31] uses a 1000 °C annealing temperature instead

[24] In a communication with Prof. Kevin Homewood, an ambiguity in their reported experimental setup was discovered. Their measurement technique is reported as follows. "The emitted power from the face of the device was measured by placing it immediately adjacent to a large area calibrated power meter" [31]. A butt coupling setup was not in fact used. Instead, light was collected with a lens, directed to the power meter, and the reading was multiplied by an unspecified collection efficiency derived from the lens geometry.

of 950 °C, and does not contain an Er implant. Both studies use a 20 minutes annealing time. However, in [32] it is reported that a for a 20 minute annealing time, a 950 °C anneal results in ~1.4 times as much EL power as samples annealed at 1000 °C.

An example of integrated EL power vs current is shown in Figure 57 for an SOI-LED emitting in the 1.1 μm band. The power vs current is seen to be slightly sublinear. The external quantum efficiency, η_{ext}, at 40 mA is calculated to be $8.7*10^{-6}$ +/- 45%. The device is likely less efficient than previously reported bulk LEDs prepared in a similar manner due to heating effects arising from the higher current density, interference modulation from the SOI cavity, as well as a reduction in carrier life-time introduced by the buried Si/SiO_2 interface. It is noted that the η_{ext} of the current SOI-LED is larger than some reports of Si LEDs, monolithically integrated on SOI [84, 91], but is 16 times smaller than that reported in [87]. Regardless, the external efficiency of the LEDs reported here suggests further improvement in device design is required before integration with SOI waveguides provides edge emission compatible with applications in traditional optical communications. Unfortunately, SOI LEDs emitting at 1.5 μm have not been demonstrated. Although the necessary material has been implanted, an attempt with the Surrey I batch, route C:Er, was unsuccessful due to an error made by the experimenter during processing.

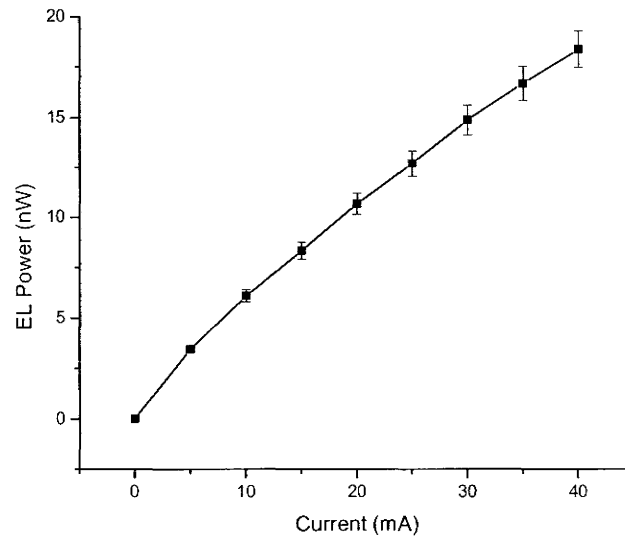

Figure 57: EL power vs current for a laterally injected 1 mm diameter LED integrated on SOI. The sample was fabricated with the DE route C, and emits at 1.1 μm. The power axis corresponds to the raw power meter reading in the two lens setup.

Co-implantation of phosphorous does not appear to improve efficiency. Simple junction theory [163] predicts that increasing the doping level on the *n*-side of the junction increases the proportion of the total current that is from electron injection. Based on the DE model, this should result in a higher EL efficiency. However, bulk LEDs formed from route A:Er and B:Er measure an η_{ext} near $1*10^{-5}$.

Problems in reproducibility were experienced. Compared to batch I, the SOI samples from the Surrey II batch, route A:Er, exhibited very different IV curves, with similar reverse bias currents, but requiring voltages ~18 times larger to achieve the same forward bias current. The IV characteristics may be more closely examined to characterize the diode behaviour, although this is left as

future work. The EL η_{ext} on these SOI devices is $1.5*10^{-6}$. The LEDs formed from the epitaxial Si exhibited normal IV curves, but resulted in very little EL power, measuring an η_{ext} of $5.6*10^{-7}$. It is not clear if these results are typical, are due to reproducibility problems with DE fabrication, or are due to the subsequent LED processing.

6.3 Summary of Defect Engineered LEDs

Photoluminescence from the SOI wafers showed a strong influence from the optical cavity. This effect was modeled, although the model was limited by the unknown change in refractive index caused by free carriers introduced by the pump light. The result is important since PL on SOI is explored in the search for an integrated Si emitter [85, 86, 88, 137] as well as for material characterization for the microelectronics industry [164].

Si LEDs integrated on an SOI platform using lateral injection geometry were demonstrated, and the EL efficiency of bulk and SOI LEDs was characterized.

While these results demonstrate improved utility of DE, significantly lower than expected efficiencies were measured, and problems with reproducibility were experienced. To explore these issues it seems necessary to obtain a greater number of samples, and to invest time commensurate with an entirely new graduate project. However, given the overall performance of the DE

LEDs, and the lack of support for the DE model that has accumulated in the literature since the start of this project, such pursuits are left to others to decide if the pursuit of DE light emission is of any value.

Chapter 7. Conclusions

The thesis covers the integration of light emitters into optical slab waveguides. Of paramount concern is that that the entire platform is VLSI compatible. This was accomplished using two techniques, namely, DE, and Si-ncs.

In the DE work, LEDs emitting at 1.1 and 1.5 μm were demonstrated on bulk Si, and on an SOI platform. LEDs were designed, fabricated, and characterized. The LEDs were designed to use a lateral injection scheme. Surface PL spectra of SOI were analyzed to account for interference. It was concluded that the optical constants of the SOI, specifically the refractive index dispersion introduced by excited carriers, was known with insufficient accuracy to enable predictive fitting of the emission spectrum. The surface EL emission efficiency of the LEDs was characterized, and compared to other Si LEDs fabricated on bulk and SOI.

In the nanocrystal work, Si-ncs were integrated with SiN_x waveguides. For comparison, standard Si-nc core waveguides were also fabricated. Optically pumped waveguides emitting at ~850 nm were designed, fabricated and characterized. Edge PL was measured and analyzed. Two-sectioned devices

were demonstrated that contain an emitting section integrated with a low-loss transmitting section. The coupling loss between the two regions was found to be negligible compared to propagation losses, and the device functioned as an emitter coupled to a transmission line. Edge emission from the waveguides was found to be well described as a propagating guided mode with waveguide loss introduced primarily from the Si-nc layer. Throughout the discussion of the Si-nc work (Chapter 5), future work was suggested. Most importantly, the pursuit of edge emitting ridge or channel waveguides was recommended.

Appendix I Gain Measurement

Preliminary gain measurements are presented here with 850 nm TE polarized probe light prism coupled into an air/Si-nc/SiN_x/SiO_2 waveguide. The waveguide was surface-pumped with a continuous wave 405 nm laser light. Edge emission of the probe light was detected using lock-in detection. Since the probe light was chopped, no pump signal was directly detected. Figure 58 shows the pump and probe signal as a function of time. The results are extremely surprising.

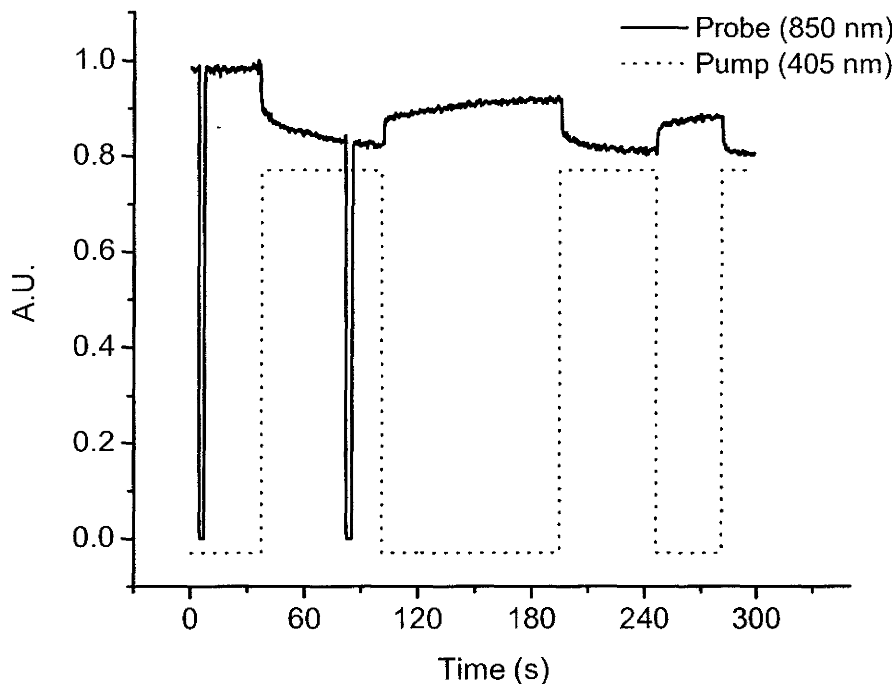

Figure 58: Pump-probe measurement of surfaced pumped prism coupled light in an integrated Si-nc waveguide. Near the beginning of the measurement, the probe beam was blocked to illustrate the time constant of the system.

When the pump light is turned on, the probe signal consistently drops several %. With the pump light turned off, the probe signal makes a partial recovery. Both the drop and recovery have a fast and slow component. The behaviour of the slow components are reminiscent to fatigue behaviour, and is assumed to be related to the same mechanism.

The probe induced loss can be explained by free carrier absorption (FCA), as has been done by others [139]. As probe light is absorbed, carriers are quickly excited. When the probe light is turned off, the excess carriers quickly recombine. (In other measurements not shown, the PL excitation and decay time constants are measured to be <100 μs). Such behaviour is discouraging news. It suggests that gain, under CW excitation at 850 nm, is either absent or offset by free carrier absorption. This behaviour is observed with several combinations of pump and probe intensities.

The slow portion of the probe induced loss is consistent with the "blinking" theory suggested to explain recoverable fatigue. When the pump light is turned on, FCA quickly increases the propagation loss. According to the "blinking" theory, the free carrier population will slowly increase as carriers become traped at the Si-nc interface, leaving behind an unpaired carrier that is now unable to recombine for lack of a partner. Such behaviour would encourage a slow increase in loss as these unpaired carriers are generated. Conversely, with the pump signal blocked, signal quickly increases as the photoexcited carriers recombine. According to the "blinking" theory, the unpaired carriers will slowly

recombine as their partners become untrapped. Such behaviour would encourage a slow decrease in loss.

The "blinking" theory has not been confirmed. Here, it is simply noted that the pump probe results are consistent with the expected behaviour. The results presented here are preliminary and have not been quantified. Further testing is required to explore the parameter space.

References

[1] M. Lipson, "Guiding, modulation and emitting light on silicon – challenges and opportunities," J. Lightwave Tech. **23** 4222 (2005)
[2] G. T. Reed, "The optical age of silicon," Nature **427** 595-596 (2004)
[3] G. T. Reed, A. P. Knights, *Silicon Photonics: An introduction* (Wiley, 2004)
[4] D. J. Lockwood L. Pavesi, , "Silicon Photonics," Topics in Applied Physics **94** (2004)
[5] J. D. Plummer, M. D. Deal, P. B. Griffin, *Silicon VLSI Technology, Fundamentals, Practice and Modeling* (Prentice Hall, 2000)
[6] J. D. B. Bradley, P. E. Jessop, A. P. Knights, "Silicon waveguide-integrated optical power monitor with ehnahced sensitivity at 1550 nm," Appl. Phys. Lett **86** 241103 (2005)
[7] M. Green, J.H. Zhao, A. H. Wang, P. J. Reece, M. Gal, "Efficient Si light-emitting diodes," Nature **412** 805-808 (2001)
[8] A. Mills, "Compound semiconductors on silicon," III-V's Review **15** 30 (2002)
[9] W. Bogaerts, D. Taillaert, B. Luyssaert, P. Dumon, J. Van Campenhout, P. Bienstman, D. Van Thourhout, R. Baets, "Basic structures for photonic integrated circuits in silicon-on-insulator," Optics Express **12** 1583 (2004)
[10] M. Schnarrenberger, L. Zimmermann, T. Mitze, J. Bruns, K. Petermann, "Facet preparation of SOI waveguides by etching and cleaving compared to dicing and polishing," First IEEE International Conference on Group IV Photonics **29** 72-74 (2004)
[11] L T Canham, "Silicon quantum wire array fabrication by electrochemical and chemical dissolution of wafers," Appl. Phys. Lett. **57** 1046-1048 (1990)
[12] H. Rong, A. Liu, R. Jones, O. Cohen, D. Hak, R. Nicolaescu, A. Fang, M. Paniccia, "An all-silicon Raman laser," Nature **433** 292-294 (2005)
[13] A. W. Fang, H. Park, O. Cohen, R. Jones, M. J. Paniccia, J. E. Bowers, "Electrically pumped hybrid AlGaInAs silicon evanescent laser," Opt. Express **14** 9203 (2006)
[14] J. M. Sun, T. Dekorsy, W. Skorupa, A. Mucklich, B. Schmidt, M. Helm, "Efficient silicon light emitting diodes by boron implantation: the mechanisim," Opt. Mater. **27** 1041-1045 (2005)
[15] S. F. Yu, C. Yuen, S. P. Lau, Y. G. Wang, H. W. Lee, B. K. Tay, "Ultraviolet amplified spontaneous emission from zinc oxide ridge waveguides on silicon substrate," Appl. Phys. Lett. **83** 4288 (2003)
[16] R. G. Heideman, P. V. Lambeck, "Remote opto-chemical sensing with extreme sensitivity: design, fabrication and performance of a pigtailed integrated optical phas-modulated Mach-Zehnder interferometer system," Sens. Actuators B-chem. **61** 100-127 (1999)
[17] O. Hofmann, G. Voirin, PNeidermann, A. Manz, "Three-dimensional microfluidic confinement for effencient sample delivery to biosensor surfaces. Application to immunoassays on planar optical waveguides," Anal. Chem. **74** 5243-5250 (2002)
[18] J. N. Milgram, A. P. Knights, K. P. Homewood, R. M Gwilliam, "Considerations for interpretation of luminescence from silicon-on-insulator light emitting structures," Semicond. Sci. Technol. **22** 1104-1110 (2007)

[19] J. N. Milgram, J. Wojcik, P. Mascher, A. P. Knights, "Optically pumped Si nanocrystal emitter integrated with low loss silicon nitride waveguides," Optics Express **15** 14679-14688 (2007)

---

[20] P. Y. Yu, M. Cardona, *Fundamentals of Semiconductors, Physics and Material Properties 2nd edition* (Springer-Verlag, 1999)
[21] J. I. Pankove, *Optical processes in semiconductor* (Prentice Hall, 1971)
[22] G. Davies, "The optical properties of luminescence centres in silicon," Physics Reports **176** 83-188 (1989)
[23] L. C. Kimerling, K. D. Kolenbrander, J. Michel, J. Palm, "Light emission from silicon," Solid State Physics **50** 333-381 (1997)
[24] S. M. Sze, *Physics of Semiconductors Device, 2nd Editions* (John Wiley & Sons, 1981) Chapter 1.5.3
[25] I. Schnitzer, E. Yablonovitch, C. Caneau, T. J. Gmitter, "Ultrahigh spontaneous emission quantum efficiency, 99.7% internally and 72% externally, from AlGaAs/GaAs/AlGaAs double heterostructures
[26] M. Lahbabi, A. Ahaitouf, M. Flyou, E. Abarkan, J. P. Charles, A. Bath, A. Hoffmann, S. E. Kerns, D. V. Kerns Jr., "Analysis of electroluminescence spectra of silicon and gallium arsenide p-n junction in avalanche breakdown," J. Appl. Phys. **95** 1822 (2004)
[27] M. S. Hybersten, "Absorption and emission of light in nanoscale silicon structures," Phys. Rev. Lett. **72** 1514 (1994)
[28] H. Yonezu, Y. Furukawa, H. Abe, Y. Yoshikawa, S.-Y. Moon, A. Utsumi, Y. Yoshizumi, A. Wakahara, M. Ohtani, "Elemental devices, circuits and processes for a monolithic Si/III-V-N alloy OEIC," Opt. Mater. **27** 799-803 (2005)
[29] C. F. Shih, N. C. Chen, C. A. Chang, K. S. Liu, "Blue, green and white InGaN light-emitting diodes grown on Si," Japanese Journal of Applied Physics **44** L140 (2005)
[30] L. Pavesi, "A review of the various efforts to a silicon laser", Proceedings of SPIE (Photonic West, San Diego 2003)
[31] W. L. Ng, M. A. Lourenco, R. M. Gwilliam, S. Ledain, G. Shao, K. P. Homewood, "an efficient room-temperature silicon-based light-emitting diode," Nature **410** 192 (2001)
[32] M. A. Lourenco, M. S. A Siddiqui, R. M. Gwilliam, G. Shao, K. P. Homewood, "Efficient silicon light emitting diodes made by dislocation engineering," Physica E **16** 376-381 (2003)
[33] A. D. Prins, Y. Ishibashi, S. Sasahara, J. Nakahara, M. A. Lourenco, R. M. Gwilliam, T. Kobayashi, A. Nagata, K. P. Homewood, "Silicon-based light emitting diode material studied under high pressure," Phys. Stat. Sol. (b) **14** 3387-3390 (2004)
[34] R. Gwilliam, M. A. Lourenco, M. Milsovljevic, K. P. Homewood, G. Shao, "Dislocation engineering for Si-based light emitting diodes," Mat. Sci. Eng. B **124-125** 86-92 (2005)
[35] M. A. Lourenco, M. S. A Siddiqui, G. Shao. R. M. Gwilliam, K. P. Homewood, "Ion beam fabricated silicon light emitting diodes," Phys. Stat. Sol. (a) **201** 239-244 (2004)
[36] A. D. Prins, T. Ishibashi, S. Sasahara, J. Nakahara, M. A. Lourenco, R. M. Gwilliam. T. Kobayashi, A. Nagata, K. P. Homewood, "Silicon-based light emitting diode material studied under high pressure," Phys. Stat. Sol (b) **241** 3387-3390 (2004)
[37] M. Milosavljevic, G. Shao, M. A. Lourenco, R. M. Gwilliam, K. P. Homewood, "Engineering of boron-induced dislocation loops for efficient room-temperature silicon light-emitting diodes," J. Appl. Phys **97** 073512 (2005)
[38] M. A. Lourenco, M. Milosavljevic, R. M. Gwilliam, K. P. Homewood, G. Shao, "On the role of dislocation loops in silicon light emitting diodes," Appl. Phys. Lett. **87** 201105 (2005)
[39] M. A. Lourenco, M. Milosavljevic, G. Shao, R. M. Gwilliam, K. P. Homewood, "Boron engineered dislocation loops for efficient room temperature silicon light emitting diodes," Thin Solid Films **504** 36-40 (2006)

---

[40] M. Milosavljevic, M. A. Lourenco, G. Shao, R. M. Gwilliam, K. P. Homewood, "Optimising dislocation-engineered silicon light-emitting diodes," Appl. Phys. B. **83** 289-294 (2006)
[41] N. A. Sobolev, A. M. Emel'yanov, E. I. Shek, V. I. Vdovin, "Extended structural defects and their finfluence on the electroluminescence in efficient Si light-emitting diodes," Physica B **340-342** 1031-1035 (2003)
[42] G. Z. Pan, R. P. Ostroumov, L. P. Ren, Y. G Lian, K. L. Wang, "Silicon light emissions from boron implant-induced defect engineering," J. Non-Crystalline Solids **352** 2506-2509 (2006)
[43] D. J. Stowe, S. A. Galloway, S. Senkader, K. Mallik, R. J. Falster, P. R. Wilshaw, "Near-band gap luminescence at room temperature from dislocations in silicon" Physica B **340-342** 710-713 (2003)
[44] M. Kittler, T. Arguirov, A. Fischer, W. Seifert, "Silicon-based light emission after ion implantation," Opt. Mater. **27** 967-972 (2005)
[45] T. Hoang, P. LeMinh, J. Holleman, J. Schmitz, "The effect of dislocation loops on the light emission of silicon LED's," IEEE Elec. Dev. Lett. **27** 105 (2006)
[46] Personal communication, from Kevin Homewood and Russell Gwilliam while working on our collaborative journal paper, later published in J. Semi. Sci. Tech. **22** 1104 (2007)
[47] T. Hoang, J. Holleman, P. LeMinh, J. Schmitz, T. Mchedlidze, T. Arguirov, M. Kittler, "Influence of dislocation loops on the near-infrared light emission from silicon diodes," IEEE Trans. Elec. Dev. **54** 1860 (2007)
[48] V. Kveder, M. Badylevich, E. Steinman, A. Izotov, M. Seibt, W. Schroter, "Room-temperature silicon light-emitting diodes based on dislocation luminescence," Appl. Phys. Lett. **84** 2106-2108 (2004)
[49] O. E. Sveinbjornsson, J. Weber, "Room temperature electroluminescence from dislocation-rich silicon," App. Phys. Lett. **69** 2686 (1996)
[50] D. Comedi, O. H. Y. Zalloum, E. A. Irving, J. Wojcik, T. Roschuk, M. J. Flynn, P. Mascher, "X-ray-diffraction study of crystalline Si nanocluster formation in annealed silicon-rich silicon oxides," J. Apl. Phys **99** 023518 (2006)
[51] R. J. Walters, J. Kalkman, A. Polman, H. A. Atwater, M. J. A de Dood, "photoluminescence quantum efficiency of dense silicon nanocrystal ensembles in SiO_2," Phys. Rev. B **73** 132302 (2006)
[52] L. Pavesi, L. Dal Negro, C. Mazzoleni, G. Franzo, F. Priolo, "Optical gain in silicon nanocrystals," Nature **408** 440 (2000)
[53] P. M. Fauchet, J. Ruan, H. Chen, L. Pavesi, L. Dal Negro, M. Cazzaneli, R. G. Elliman, N. Smith, M. Samoc, B. Luther-Davies, "Optical gain in different silicon nanocrystals systems," Opt. Mater. **27** 745-749 (2005)
[54] A. Hryciw, A. Meldrum, K. S. Buchanan, C. W. White, "Effects of particle size and excitation spectrum on the photoluminescnece of silicon nanocrystals formed by ion implantation," Nuclear Instrum. Methods in Phys. Res. B **222** 469-476 (2004)
[55] M. L. Brongersma, P. G. Kik, A. Polman, K. S. Min H. A. Atwater, "Size-dependent electron-hole exchange interaction in Si nanocrystals," Appl. Phys. Lett. **76** 351 (2000)
[56] P. Mutti, G. Ghislotti, S. Bertoni, L. Bonoldi, G. F. Cerofolini, L. Meda, E. Grilli, M. Guzzi, "Room-temperature visible luminescence from silicon nanocrystals in silicon implanted SiO_2 layers," Appl. Phys. Lett **66** 851 (1995)
[57] F. Iacona, G. Franzo, C. Spinella, "Correlation between luminescence and structural properties of Si nanocrystals," J. Appl. Phys. **87** 1295 (1999)

---

[58] V. Vinciguerra, G. Franzo, F. Priolo, F. Iacona, C. Spinella, "Quantum confinement and recombination dynamics in silicon nanocrystals embedded in Si/SiO_2 superlattices," J. Appl. Phys. **87** 8165 (2000)
[59] C. Garcia, B. Garrido, P. Pellegrino, R. Ferre, J. A. Moreno, J. R. Morante, L. Pavesi, M. Cazzaneilli, "Size dependence of lifetime and absorption cross section of Si nanocrystlas embedded in SiO_2," Appl. Phys. Lett. **82** 1595 (2003)
[60] M. Glover, A. Meldrum, "Effect of "buffer layers" on the optical properties of silicon nanocrystal superlattices," Opt. Mater. **27** 977-982 (2005)
[61] A. R. Wilkinson, R. G. Elliman, "Kinetics of H_2 passivation of Si nanocrystals in SiO_2," Phys. Rev. B **68** 155302 (2003)
[62] E. Neufeld, S. Wang, R. Apetz, Ch. Buchal, R. Carius, C. W. White, D. K. Thomas, "Effect of annealing and H_2 passivation on the photoluminescence of Si nanocrystals in SiO_2," Thin Solid Films **294** 238-241 (1997)
[63] A. R. Wilkinson, R. G. Elliman, "Maximizing light emission from silicon nanocrystals –The role of hydrogen," Nuclear Instrum. Method. Phys. Res. B **242** 303-306 (2006)
[64] D. Comdei, O. H. Y. Zalloum, P. Mascher , "H-sensitive radiative recombination path in Si nanoclusters embedded in SiO_2," Appl. Phys. Lett **87** 213110 (2005)
[65] A. Meldrum A. Hryciw, A. N. MacDonald, C. Blois, K. Marsh, J. Wang, Q. Li, "Phtotluminescence in the silicon-oxygen system," J. Vacuum Science & Tech. A. Vacuum, Surfaces, and Films **24** 713 (2006)
[66] G. Y. Sung, N.M. Park, J.H. Shin, K. H. Kim, T. Y. Kim, K. S. Cho, C. Huh, "Physics and device structures of highly efficient silicon quantum dots based silicon nitride light-emitting diodes," IEEE J. Sel. Top. Quant. Elec. **12** 1545 (2006)
[67] T. Trupke, J. Zhao, A. Wang, R. Corkish, M. A. Green, "Very efficient light emission from bulk crystalline silicon," Appl. Phys. Lett. **82** 2996 (2003)
[68] O. Bisi, S. Ossicini, L. Pavesi, "Porous silicon: a quantum spnge structure for silicon based optoelectronics," Surface Science Reports **38** 1-126 (2000)
[69] B. Hamilton, "Porous silicon", Semicond. Sci. Technol. **10** 1187-1207 (1995)
[70] A. G. Cullis, L. T. Canham, P. D. J. Calcott, "The structural and luminescence properties of porous silicon," Appl. Phys. Rev. **82** 909-965 (1997)
[71] M. V. Wolkin, J. Jorne, P. M. Fauchet, G. allan, C. Delerue, "Electronic states and luminescence in porous silicon quantum dots: The role of oxygen," Phys. Rev. Lett. **82** 197 (1999)
[72] C. Lee, C. Lin, T. Lee, T. Tsai, "Photoluminescence degradation and passivation mechanisms of Si nanoclusters in silicon oxide matrix," J. J Appl. Phys. **44** 4240-4244 (2005)
[73] D. Amans, O. Guillois, G. Ledoux, D. Porterat, C. Reynaud, "Influence of light intensity on the photoluminescence of silicon nanostructures," J. Appl. Phys. **91** 5334 (2002)
[74] J. Valenta, J. Linnros, R. Juhasz, F. Cichos, J. Martin, "Optical spectroscopy of single quantum dots," *Proceedings of the NATO Advanced Research Workshop on Torards the first silicon laser*, Trento, Italy, II Mathematics, Physics and Chemistry **93** 89-106 (2002)
[75] F. Cichos, J. Martin, C. von Borczyskowski, "Emission intermittency in silicon nanocrystals," Phys. Rev. B **70** 115314 (2004)
[76] A. L. Efros, M. Rosen, "Random telegraph signal in the photoluminescence intensity of a single quantum dot," Phys. Rev. Lett. **78** 1110 (1997)
[77] D. E. Gomez, M. Califano, P. Mulvaney, "Optical properties of single semicondutor nanocrystals," Phys. Chem. Chem. Phys. **8** 4989-5011 (2006)

---

[78] I. Sychugov, R. Juhasz, J. Linnros, J. Valenta, "Luminescence blinking of a Si quantum dot in a SiO_2 shell," Phys. Rev. B **71** 115331 (2005)
[79] G. Barillaro, A. Diligenti, F. Pieri, F. Fuso, M. Allegrini, "Integrated porous-silicon light-emitting diodes: A fabrication process using graded doping profiles," Appl. Phys. Lett. **78** 4154 (2001)
[80] V. Torres-Costa , F. Agullo-Rueda , R .J. Martin-Palma , J. M. Martinez-Duart, "Porous silicon optical devices for sensing applications," Opt. Mater. **27** 1084-1087 (2005)
[81] A. J. Kenyon, "Erbium in silicon," Semicond. Sci. Technol. **20** R65-R84 (2005)
[82] A. Polman, "Erbium implanted thin film photonic materials," J. Appl. Phys. **82** 1 (1997)
[83] D. Pacifici, A. Irreara, G. Franzo, M. Miritello, F. Iacona, F. Priolo, "Erbium-doped Si nanocrystals: optcial properties and electrolumenscent devices," Physica E **16** 331-340 (2003)
[84] J. Zhao, G. Zhang, T. Trupke, A. Wang, F. Hudert, M. A. Green, "Near-band edge light emission from silicon semiconductor on insulator diodes," Appl. Phys. Lett. **85** 2832 (2004)

[85] A. Karsenty, A. Sa'ar, N. Ben-Yosef, J. Shappir, "Enhanced electroluminescence in silicon-on-insulator metal-oxide-semiconductor transistors with thin silicon layer," Appl. Phys. Lett. **82** 4830 (2003)
[86] J. Potfajova, J. M. Sun, B. Schmidt, T. Dekorsy, W. Skorupa, B. Helm, "Silicon-on-insulator microcavity light emitting diodes with two Si/SiO2 Bragg reflectors," J. Luminescence **121** 290-292 (2006)
[87] T. Hoang, P. LeMinh, J. Holleman, J. Schmitz, "Strong Efficiency improvement of SOI-LEDs through carrier confinement," IEEE Elec. Dev. Lett. **28** 383 (2007)
[88] E. Cho, M. A. Green, J. Xia, R. Corkish, P. Reece, M. Gal, "Clear quantum-confined luminescence from crystalline silicon/SiO_2 single quantum wells," Appl. Phys. Lett. **84** 2286 (2004)
[89] E. Cho, M. A. Green, R. Corkish, R. Reece, M. Gal, S. Lee, "Photoluminescence in crystalline silicon quantum wells," P. Appl. Phys. **101** 024321 (2007)
[90] S. G. Clouthier, P. A. Kossyrev, J. Xu, "Optical gain and stimulated emissionin periodic nanopatterned crystalline silicon," Nature Materials **4** 887 (2005)
[91] H. Rocken, J. Meijer, A. Stephan, U. Weidenmuller, H. H. Bukow, C. Rolfs, "White electroluminescent nanostructures in silicon fabricated using focused ion implantation," Nuclear Instrum. Method. Phys. Res. B. **181** 274-279 (2001)
[92] J. S. Xia, Y. Ikegami, K. Nemoto, Y. Shiraki, "Observation **of** whispering-gallery modes **in** Si microdisks **at** room temperature," Appl. Phys. Lett. **90** 141102 (2007)
[93] K. Misiakos, S. E. Kakabakos, P. S. Petrou, H. H Ruf, "A monolithic silicon optoelectronic transducer as a real-time affinity biosensor," Anal. Chem. **74** 1366-1373 (2004)
[94] A. Yamada, M. Sakuraba, J. Murota, "Integration of Si p-i-n diodes for light emitter and detector with optical waveguides," Mat. Sci. Semi. Processing **8** 435-438 (2005)
[95] L. Pavesi, L. Dal Negro, C. Mazzoleni, G. Franzo, F. Priolo, "Optical gain in silicon nanocrystals," Nature
408, 440-444 (2000)
[96] J. Valenta, I. Pelant, J. Linnros, "Waveguiding effects in the measurement of optical gain in a layer of Si nanocrystals," App. Phys. Lett. **81**, 1396-1398 (2002)

---

[97] L. Dal Negro, P. Bettotti, M. Cazzanelli, D. Pacifici, L. Pavesi, "Applicability conditions and experimental analysis of the variable stripe length method for gain measurements," Opt. Commun. **229**, 337-348 (2004).
[98] T. Ostatnicky, J. Valenta, I. Pelant, K. Luterova, R. G. Elliman S. Cheylan, B. Honerlage, "Photoluminescence from an active planar optical waveguide made of silicon nanocrystals: dominance of leaky substrate modes in dissipative structures," Opt. Mater. **27**, 781-786 (2005)
[99] L. Khriachtchev, D. Navarro-Urrios, L. Pavesi, C. J. Oton, N. E. Capuj, S. Novikov, "Spectroscopy of silica layers containing Si nanocrystals: Experimental evidence of optical birefringence," J. Appl. Phys. **101**, 044310 (2007).

[100] R. T. Neal, M. D. C. Charlton, G. J. Parker, C. E. Finlayson, M. C. Netti, J. J. Baumberg, "Ultrabroadband transmission measurements on waveguides of silicon-rich silicon dioxide," Appl. Phys. Lett. **83,** 4598-4600 (2003).

[101] R. G. Elliman, M. Forcales, A. R. Wilkinson, N. J. Smith, "Waveguiding properties of Er-implanted silicon-rich oxides," Nucl. Instrum. Methods Phys. Res. B **257**, 11-14 (2007).

[102] P. Pellegrino, B. Garrido, C. Garcia, J. Arbiol, J. R. Morante, M. Melchiorri, N. Daldosso, L. Pavesi, E. Scheid, G. Sarrabayrouse, "Low-loss rib waveguides containing Si nanocrystals embedded in SiO2," J. Appl. Phys. **97**, 074312 (2005).
[103] N. Daldosso, D. Navarro-Urrios, M. Melchiorri, L. Pavesi, F. Gourbilleau, M. Carrada, R. Rizk, C. Garcia, P. Pellegrino, B. Garrido L. Cognalto, "Absorption cross section and signal enhancement in Er-doped Si nanocluster rib-loaded waveguides," Appl. Phys. Lett. **86**, 261103 (2005).
[104] J. Lee, J. H. Shin, N. Park, "Optical gain at 1.5 μm in nanocrystal Si-sensitized Er-doped silica waveguide using top-pumping 470 nm LEDs," J. Lightwave Tech. **23** 19-25 (2005)
[105] D. S. Gardner, M. L. Brongersma, "Microring and microdisk optical resonators using silicon nanocrystals and erbium prepared using silicon technology," Opt. Mater. **27**, 804-811 (2005).
[106] L. Tallone, C. De Bernardi, "Low cost optical amplifier," US Patent 7068420 (2006)
[107] J. Shin, H. Han, N. Park, "Top pumped waveguide amplifier," US Patent 7075708 (2006)
[108] J. T. Simpson, M. L. Simpson, Marcus, S. P. Withrow, C. W. White, S. L. Jaiswal, "Nanocrystal waveguide (NOW) laser," US Patent 6853669 (2005)
[109] J. H. Hunt, "Optical integrated circuit," US Patent 6822305 (2004)
[110] A. Givant, J. Shappier, A. Sa'ar, "Porous silicon on insulator: A new approach to fabriate porous silicon based optoelectronic devices," Phys. Stat. Sol. a) **182** 419 (2000)
[111] S. K. Lazarouk, P. V. Jaguiro, A. A. Leshok. V. E. Borisenko, "Reverse biased porous silicon light-emitting diodes for optical intra-chip interconnects," Physica E **16** 495-498 (2003)
[112] H. Nishihara, M. Haruna, T. Suhara, "Optical Integrated Circuits" (McGraw-Hill Professional, 1989)
[113] D. Marcuse, *Theory of dielectric optical waveguides, 2nd sub edition* (Academic Press, 1991)
[114] J. Chilwell, I. Hodgkinson, "Thin-films field-transfer matrix theory of planar multilayer waveguides and reflection from prism-loaded wavegduies," J. Opt. Soc. Am. A **1** 742-753 (1984)
[115] http://www.rsoftdesign.com
[116] Haes, B. Demeulenaere, R. Baets, D. Lenstra, T. D. Visser, H. Block, "Difference between TE and TM modal gain in amplifying waveguides: analysis and assessment of two perturbation approaches," Opt. Quantum. Electron. **29**, 263-273 (1997).

---

[117] A. W. Snyder, J. D. Love, *Optical Waveguide Theory* (Chapman and Hall, 1983)
[118] S. R. J. Brueck, "Radiation from a dipole embedded in a dielectric slab," IEEE J. Sel. Top. Quant. Elec. **6** 899-910 (2000)
[119] Y. Suematsu, K. Furuya, "Theoretical spontaneous emission factor if injection lasers," Trans. IECE Jap. **E 60** 467-472 (1977)
[120] D. Marcuse, "Launching light into fiber cores from sources located in the cladding," J. Lightwave Tech. **6** 1273 (1988)
[121] A. H. Hartog, M. P. Gold, "On the theory of backscattering in single-mode optical fibers," J. Lightwave Tech. **2** 76 (1984)
[122] D. T. Cassidy, "Spontaneous-emission factor of semiconductor diode lasers," J. Opt. Soc. Am. B **8** 747 (1991)
[123] K. Izuka, *Elements of Photonics, Volume I, In free space and special media* (John Wiley & Sons, 2002)
[124] ATHENA User's Manual 2002 (Santa Clara, CA: Silvaco International Inc.)
[125] G. T. A. Kovacs, N. I. Maluf, K. E. Petersen, "Bulk micromachining of silicon" Proc. IEEE **86** 1536-1551 (1998)
[126] W. Stutius, W. Streifer, "Silicon nitride films on silicon for optical waveguides," Apl. Optics **16** 3218-3222 (1977)
[127] G. L. Bona, R. Germann, B. J. Offrein, "SiON high-refractive-index waveguide and planar lightwave circuits," IBM J. Res. & Dev. **47** 239-249 (2003)
[128] N. Daldosso, M. Melchiorri, F. Riboli, M. Girardini, G. Pucker, M. Crivellari, P. Bellutti, A. Lui, L. Pavesi, "Comparison among various Si_3N_4 waveguide gemoetries grown within a CMOS fabrication pilot line, " J. Lightwave Technol. **22** 1734-1740 (2004)
[129] D. Comdei, O. H. Y. Zalloum, E. A. Irving, J. Wojcik, P. Mascher, "H-induced effects in luminescent silicon nanostructures obtained from plasma enhanced chemical vapor deposition grown Si_yO_{1-y}:H(y<1/3) thin films annealed in (Ar+5%H2)," J. Vac. Sci. Technol. A **24** 817-820 (2006)
[130] X. Tan, J. Wojcik, P. Mascher, "Study of the optical properties of SiO_xN_y thin films by effective medium theories," J. Vac. Sci. Technol. A **22** 1115-1119 (2004)
[131] Y. Q. Wang, R. Smirani, G. G. Ross, "The effect of implantation dose on the microstructure of silicon nanocrystals in SiO_2," Nanotechnology **15** 1554-1560 (2004)
[132] R. T. Holm, S. W. McKnight, E. D. Palik, W Lukosz, "Interference effects in luminescence studies of thin films," *Appl. Optics* **21** 2512 (1982)
[133] D. C. Marra, E. S. Aydil S-J Joo, E. Yoon, V. I. Srdanov, "Angle-dependent photoluminescence spectra of hydrogenated amorphous silicon thin films," *Appl. Phys. Lett* **77** 3346 (2000)

[134] R. Ferre, B. Garrido, P. Pellegrino, M. Peralvarez, C. Garcia, J. A. Moreno, J. Carreras, J. R. Morante *J, "Optical-geometrical effects on the photoluminescence spectra of Si nanocrystals embedded in SiO_2," Appl. Phys* ***98*** 084319 (2005)
[135] Introduction to Modern Optics 2nd Edition, Chapter 4, Fowles G R, Dover Publications Inc. New York (1975)
[136] R. Smirani, R. Martin, G. Abel, Y. Q. Wang, M. Chicoine, G. G. Ross, "The effect of size and depth profile of Si-nc imbedded in a SiO_2 layer on the photoluminescence spectra,"*J. Luminescence* **115** 62 (2005)

---

[137]C. B. Li, C. J. Huang, B. W. Cheng, Y. H. Zuo, R. W. Mao, L. P. Luo, J. Z. Yu, Q. M. Wang, "Cavity-enhanced photoluminescence of SiG/Si multiquantum wells grown on silicon-on-insulator substrate,".*J Appl. Phys.* **95** 5914 (2004)
[138] P. K. Tien, R. Ulrich, "Theory of prism-film coupler and thin-film light guides," J. Optical Soc. America **60** 1325 (1970)
[139] R. G. Elliman, A. R. Wilkinson, N. Smith, M. G. Spooner, T. D. M. Weijers, "Light emission from silicon nanocrystals – size does matter!," J. Korean Physical Society **45** S656 (2004)
[140] A. E. Siegman, M. W. Sasnett, T. F. Jr. Johnston, "Choice of clip levels for beam width measurements using knife-edge techniques," IEEE J. Quan. Elec. **27** 1098-1104 (1991)
[141] V. Vinciguerra, G. Franzo, F. Priolo, F. Iacona, C. Spinella, "Quantum confinement and recombination dynamics in silicon nanocrystals embedded in $SiSiO_2$ superlattics," J. Appl. Phys. **87** 8165-8173 (2000)
[142] U. S. Sias, L. Amaral, M. Behar, H. Boudinov, E. C. Moreira, "The excitation power density effect on the Si nanocrystals photoluminescence," Nucl. Instrum. Meth. Phys. Res. B. **250** 178-182 (2006)
[143] D. Kovalev, H. Heckler, G. Polisski, F. Koch, "Optical properties of Si nanocrystals," Phys. Stat. Sol. (b) **215** 871-932 (1999)
[144] Handbook of Optical Constants of Solids, E. Palik, Academic Press, 1985
[145] L. Dal Negro, J. H. Yi, J. Michel, L. C. Kimerling, T. –W. F. Chang, V. Sukhovatkin, E. H. Sargent, "Light emission efficiency and dynamics in silicon-rich silicon nitride films," Appl. Phys. Lett. **88** 233109 (2006)
[146] S. Miura, T. Nakamura, M. Fujii, M. Inui, S. Hayashi, "Size dependence of photoluminescence quantum efficiency of Si nanocrystals," Phy. Rev. B **73** 245333 (2006)
[147] R. J. Walters, J. Kalkman, A. Polman, H. A. Atwater, M. J. A. de Dood, "Photoluminescence quantum efficiency of dense silicon nanocryatsl ensembles in SiO_2," Phy. Rev. B **73** 132302 (2006)
[148] I. Pelant, T. Ostatnicky, J. Valenta, K. Luterova, E. Skopalova, T. Mates, R. G. Elliman, "Waveguide cores containing silicon nanocrystals as active spectral filters for silicon-based photonics," Appl. Phys. B **83** 87-91 (2006)
[149] L. Dal Negro, M. Cazzanelli, Z. Gaburro, P. Bettotti, L. Pavesi, F. Priolo, G. Franzo, D. Pacifici, F. Iacona, "Stimulated Emission in silicon nanocrystals," Towards the First Silicon Laser, 145-164. Kluwer Academic Publishers (2003)
[150] N. Daldosso, M. Melchiorri, L. Pavesi, G. Pucker, F. Gourbilleau, S. Chausserie, A. Belarouci, X. Portier, C. Dufour, "Optical losses and absorption cross-section of silicon nanocrystals," J. Luminescence **121** 344-348 (2006)
[151] R. G. Elliman, M. J. Jederer, B. Luther-Davies, "Optical absorption measurements of silica containing Si nanocrystals produced by ion implantation and thermal annealing," Appl. Phys. Lett. **80** 1325 (2002)
[152] L. Khriachtchev, M. Rasanen, S. Novikov, "Efficient wavelength-selective optical waveguiding in a silica layer containing Si nanocrystals," Appl. Phys. Lett. **83** 3018 (2003)
[153] J. Ruan, P. M. Fauchet. L. Dal Negro, M. Cazzanelli, L. Pavesi, "Stimulated emission in nanocrystalline silicon superlattices," Appl. Phys. Lett. **26** 5479 (2003)
[154] C. K. Wong, H. Wong, C. W. Kok, M. Chan, "silicon oxynitride prepared by chemical vapor deposition as optical waveguide materials," J. Cryst. Growth **288** 171-175 (2006)

---

[155] W. M. A. Bik, R. N. H. Linssen, F. H. P. M Habraken, W. F van der Weg, A. E. T. Kuiper, "Diffusion of hydrogen in low-pressure chemical capor deposited silicon nitride films," Appl. Phys. Lett **56** 2530 (1990)
[156] C. Boehme, G. Lucovsky, "Dissociation reactions of hyrdogen in remote plamsa-enhanced chemical-vapor-deposition silicon nitride," J. Vac. Sci. Technol. A **19** 2622 (2001)
[157] H. F. W. Dekkers, G. Beaucarne, M. Hiller, H. Charifi, A. Slaoui, "Molecular hydrogen formation in hydrogenated silicon nitride," Appl. Phys. LEtt. **89** 211914 (2006)
[158] D. Benoit, J. Regolini, P. Morin, "Hyrdogen desorption and diffusion in PECVD silicon nitride. Application to passivation of CMOS active pixel sensors," Microelectronic Engineering **84** 2169-2172 (2007)
[159] E. C. Baranova, V. M. Gusev, Y. V. Martynenko, C. V. Starinin, I. B. Haibullin, "", Radiat. Eff. **18** 21 (1973)
[160] R. A. Soref, B. R. Bennett, *IEEE J. Quantum Elec.* **23** 123 (1987)
[161] C. M. Herzinger, B. Johs, W. A. McGahan, J. A. Woollam, W. Paulson W *J. Appl. Phys.* **83** (1998)
[162] D. J. Lockwood, J. M. Baribeau, B. T. Sullivan *J. Vac. Sci. Technol. B* **16** 1707 (1998)
[163] B. G. Streetman, *Solid State Electronic Devices* (Prentice Hall, 4th Edition, 1995)
[164] M. Tajima, "Characterization of silicon-on-insulator wafers by photoluminescence under UV light excitation," *J. Crystal Growth* **237-239**, 324 (2002)

5790 35